

1

2 Analysis report on the $ep \rightarrow e' p' \pi^+ \pi^-$ reaction in the CLAS
3 detector with a 2.039 GeV beam for $0.4 \text{ GeV}^2 < Q^2 < 1.0 \text{ GeV}^2$
4 and $1.3 \text{ GeV} < W < 1.825 \text{ GeV}$

5 **G. Fedotov^{a,b}, V. Burkert^c, R. Gothe^b, V. Mokeev^{a,c}, Iu. Skorodumina^{a,b}**

6 ^a*Moscow State University,
7 Vorob'evy gory, 119899 Moscow, Russia*

8 ^b*University of South Carolina,
9 712 Main Street, Columbia, South Carolina, 29208*

10 ^c*Thomas Jefferson National Accelerator Facility,
11 12000 Jefferson Avenue, Newport News, Virginia, 23606*

¹² Contents

¹³ 1	Physics motivation	⁴
¹⁴ 2	Event selection	⁸
¹⁵ 2.1	Particles identification	⁹
¹⁶ 2.1.1	Electron identification	⁹
¹⁷ 2.1.2	Hadron identification	¹⁶
¹⁸ 2.1.3	Timing correction	¹⁷
¹⁹ 2.2	Momentum corrections	²²
²⁰ 2.2.1	Electron momentum correction	²²
²¹ 2.2.2	Proton momentum correction (Energy loss)	²³
²² 3	Other cuts and corrections	²⁶
²³ 3.1	Fiducial cuts	²⁶
²⁴ 3.1.1	Fiducial cuts for negatively charged particles	²⁶
²⁵ 3.1.2	Fiducial cuts for positively charged particles	²⁷
²⁶ 3.2	Data quality check	²⁹
²⁷ 3.3	Vertex cut	³¹
²⁸ 3.4	Exclusivity cut	³⁵
²⁹ 3.5	Missing energy cut	³⁹
³⁰ 3.6	Binning and kinematical coverage	³⁹
³¹ 4	Cross section calculation	⁴³
³² 4.1	Kinematical variables	⁴³

³³	4.2	Cross section formula	50
³⁴	4.3	Radiative corrections	53
³⁵	4.4	Efficiency evaluation	54
³⁶	4.5	Filling kinematical cells with zero acceptance	56
³⁷	4.6	Combination of various topologies	59
³⁸	5	Correction for binning effects	61
³⁹	6	Systematical errors	64
⁴⁰	6.1	Errors due to normalization, electron identification, and electron detection efficiency	64
⁴¹	6.2	Errors due to the different ways of combining topologies	65
⁴²	6.3	Errors due to the integration over different final hadron variables	65
⁴³	6.4	Systematical error summary	66
⁴⁴	7	Conclusions	68
⁴⁵	Appendix A: Measured cross sections		70
⁴⁶	Bibliography		119

⁴⁸ **Chapter 1**

⁴⁹ **Physics motivation**

⁵⁰ In this analysis note new set of differential and fully integrated cross sections for the exclusive
⁵¹ reaction $ep \rightarrow e'p'\pi^+\pi^-$ from data of the e1e run collected with the CLAS detector in
⁵² the kinematic area of $1.3 \text{ GeV} < W < 1.825 \text{ GeV}$ and $0.4 \text{ GeV}^2 < Q^2 < 1.0 \text{ GeV}^2$ is
⁵³ presented. In each bin of W and Q^2 nine single-differential cross sections are obtained.
⁵⁴ They consist of: a) three distributions over invariant masses of the final hadron pairs; b)
⁵⁵ three CM-angular distributions over polar angles θ of the final π^+ , π^- , and p' , and c) three
⁵⁶ CM-angular distributions over the angles α between two planes. One plain is defined by
⁵⁷ the three-momenta of all final hadrons. Another plane is defined by the three-momenta
⁵⁸ of virtual photon and one of the final hadrons for the three different choices of this final
⁵⁹ hadron. More detailed information about kinematical variables is in Sect. 4.1. These data
⁶⁰ were obtained for the first time in the kinematic area $Q^2 < 0.6 \text{ GeV}^2$ and $W > 1.55 \text{ GeV}$.
⁶¹ At $0.6 \text{ GeV}^2 < Q^2 < 1.0 \text{ GeV}^2$ similar $\pi^+\pi^-p$ single-differential cross sections have already
⁶² been measured with CLAS [1]. However, in this data set these cross sections are obtained
⁶³ in Q^2 -bins of bin sizes, which are roughly a factor of six smaller than those achieved in [1].

⁶⁴ The studies of exclusive $\pi^+\pi^-$ electroproduction off protons represent an important avenue
⁶⁵ in the investigation of the N^* spectrum and structure via analyses of experimental data
⁶⁶ on exclusive meson electroproduction with CLAS. The CLAS detector has provided the dominant
⁶⁷ portion of all data on meson electroproduction in the resonance excitation region. The
⁶⁸ studies of transition helicity amplitudes from the proton ground state to its excited states
⁶⁹ represent a key aspect of the N^* program with CLAS [2, 3]. Data on meson electroproduction
⁷⁰ off nucleons in the N^* region obtained with CLAS open an opportunity to determine
⁷¹ the Q^2 evolution of the $\gamma_v N \rightarrow N^*$ electrocouplings both in comparative and combined
⁷² analyses of various meson electroproduction channels. The electroexcitation amplitudes for
⁷³ the low-lying resonances $\Delta(1232)3/2^+$, $N(1440)1/2^+$, $N(1520)3/2^-$, and $N(1535)1/2^-$ have
⁷⁴ been determined over a wide range of Q^2 in a comprehensive analysis of JLab-CLAS data
⁷⁵ on differential cross sections, longitudinally polarized beam asymmetries, and beam-target
⁷⁶ asymmetries for single pion electroproduction off protons [4]. Recently $\gamma_v N \rightarrow N^*$ elec-

77 electrocouplings of several higher-lying nucleon resonances: $N(1675)5/2^-$, $N(1680)5/2^+$, and
 78 $N(1710)1/2^+$ have become available for the first time for $1.5 \text{ GeV}^2 < Q^2 < 4.5 \text{ GeV}^2$ from
 79 the analysis of exclusive π^+ electroproduction off the proton [5]. Electrocouplings for the
 80 $N(1440)1/2^+$ and $N(1520)3/2^-$ resonances for $Q^2 < 0.6 \text{ GeV}^2$ have been determined from
 81 the data [6] on exclusive $\pi^+\pi^-$ electroproduction off the proton [7]. The recent analysis [8] of
 82 the CLAS data on $\pi^+\pi^-$ electroproduction off protons [1] provided the results on electrocou-
 83 plings of these states in a wider Q^2 -range up to 1.5 GeV^2 . Furthermore, electrocouplings of
 84 the $\Delta(1620)3/2^-$ resonance that decays preferentially to the $N\pi\pi$ final states have become
 85 available from this analysis for the first time. Consistent results for the $\gamma_vp \rightarrow N^*$ elec-
 86 trocouplings of the $N(1440)1/2^+$ and $N(1520)3/2^-$ resonances, that have been determined
 87 in independent analyses of the dominant meson electroproduction channels $N\pi$ and $\pi^+\pi^-p$
 88 with completely different non-resonant contributions, demonstrated the reliable extraction
 89 of these fundamental quantities. This success also supports the capability of the reaction
 90 models, that have been developed for the extraction of the resonance parameters from the
 91 analyses of data on single- [4] and double-pion [9] electroproduction off protons, to provide
 92 reliable information on the N^* parameters from independent studies of either of these major
 93 exclusive channels.

94 The CLAS results on the $\gamma_vp \rightarrow N^*$ electrocouplings [2, 4, 5, 7, 8, 10] have had a stimulat-
 95 ing impact on the theory of the excited nucleon state structure, in particular, on QCD-based
 96 approaches. The light cone sum rule (LCSR) approach [11, 12] for the first time provided
 97 access to the quark distribution amplitudes (DAs) inside the $N(1535)1/2^-$ resonance from
 98 analysis of the CLAS results on the $\gamma_vp \rightarrow N^*$ electrocouplings of this state [4]. Confronting
 99 the quark DAs of excited nucleon states determined from the experimental results on the
 100 $\gamma_vp \rightarrow N^*$ electrocouplings to the LQCD expectations, makes it possible to explore the
 101 emergence of the resonance structure starting from the QCD Lagrangian. The moments of
 102 the $N(1535)1/2^-$ quark DAs derived from the CLAS data are consistent with the LQCD
 103 expectations [12]. The Dyson-Schwinger Equations of QCD (DSEQCD) provide a concep-
 104 tually different avenue for relating the $\gamma_vp \rightarrow N^*$ electrocouplings to the fundamental QCD
 105 Lagrangian [13–15]. The DSEQCD approach allows to evaluate the contribution of the three
 106 bound dressed quarks, the so-called quark core, to the structure of excited nucleon states
 107 starting from the QCD Lagrangian. A successful description of the nucleon elastic form
 108 factors and the CLAS results on the $N \rightarrow \Delta$, $N \rightarrow N(1440)1/2^+$ electromagnetic transition
 109 form factors [2, 4, 7, 10] at photon virtualities $Q^2 > 2.0 \text{ GeV}^2$ has been recently achieved
 110 within the DSEQCD framework [13, 15, 16]. This successful description of the form factors
 111 that correspond to distinctively different structures achieved with the same dressed quark
 112 mass function strongly underlines:

- 113 • the relevance of dynamical dressed quarks with the properties predicted by the DSE-
 114 QCD approach [17] as constituents of the quark cores for the structure of the ground
 115 and excited nucleon states;
- 116 • the capability of the DSEQCD approach [13, 15] to map out the dressed quark mass

117 function from the experimental results on the Q^2 evolution of the nucleon elastic and
118 $p \rightarrow N^*$ transition form factors ($\gamma_v p \rightarrow N^*$ electrocouplings) from a combined analysis.

119 Physics analyses of the CLAS results [4, 7, 10] on the $\gamma_v p \rightarrow N^*$ electrocouplings revealed
120 the structure of excited nucleon states at photon virtualities $Q^2 < 5.0 \text{ GeV}^2$ as a complex
121 interplay between meson-baryon and quark degrees of freedom. The relative contributions
122 from the meson-baryon cloud and the quark core are strongly dependent on the quantum
123 numbers of the excited nucleons. Analyses of the $A_{1/2}$ electrocouplings of the $N(1520)3/2^-$
124 resonance [18, 19] demonstrated that this amplitude is dominated by quark core contributions
125 in the entire range of $Q^2 < 5.0 \text{ GeV}^2$ measured by CLAS. However, the recent analysis [20]
126 of the first CLAS results [5] on the $N(1675)5/2^- \gamma_v p \rightarrow N^*$ electrocouplings suggested a
127 dominance of the meson-baryon cloud. Pronounce differences in the structure of the N^* states
128 of different quantum numbers demonstrate different manifestations of the non-perturbative
129 strong interaction in generation of excited nucleons as the bound systems of an infinite
130 amount of quarks and gluons. The studies of $\gamma_v p \rightarrow N^*$ electrocouplings for all prominent
131 nucleon resonances offer unique information on many facets of the non-perturbative strong
132 interaction and motivate the extension of the studies of $\gamma_v p \rightarrow N^*$ electrocouplings over full
133 spectrum of excited nucleons.

134 Currently the results on resonance electrocouplings in mass range above 1.6 GeV are
135 rather limited. The recent studies of single pion electroproduction [5] delivered the results on
136 electrocouplings of only those high mass states, which have a substantial branching fraction
137 for decays to the $N\pi$ final states. Several high-lying nucleon excitations, as $\Delta(1620)1/2^-$,
138 $\Delta(1700)3/2^-$, and $N(1720)3/2^+$, decay preferentially to $N\pi\pi$ final states making the channel
139 of $\pi^+\pi^-$ electroproduction off the proton the major source of information on electrocouplings
140 of these states. In the future these electrocouplings can be checked in independent analyses
141 of KY exclusive electroproduction channels [21]. The data on electrocouplings of high-lying
142 resonances, which decay both to the $N\pi$ and the $N\pi\pi$ final states, in $\pi^+\pi^-$ electroproduction
143 channel will make it possible to test the consistency of these results with those from inde-
144 pendent analyses of single pion electroproduction, offering a sensitive check of the reliability
145 of the resonance parameter extraction.

146 The experimental data on $\pi^+\pi^-$ electroproduction off protons presented in this analysis
147 note will be analyzed within the framework of the meson-baryon reaction model JM [7–
148 9], which is currently the only available approach worldwide for the extraction of resonance
149 electrocouplings from this exclusive channel. The aforementioned approach already provided
150 reliable results on electrocouplings of all resonances in mass range below 1.65 GeV with
151 sizable decays to the $N\pi\pi$ final states. The analysis of experimental data presented in this
152 note eventually will allow us to:

- 153 • determine the evolution of the electrocouplings of most nucleon resonances in mass
154 range up to 1.825 GeV with photon virtualities Q^2 up to 1.0 GeV^2 with bin sizes in Q^2
155 much smaller than previously achieved in any experiments. For high-lying resonances

156 that decay preferentially to the $N\pi\pi$ final states this information will be obtained for
157 the first time;

- 158 • explore electrocouplings of all orbital excitations ($L=1$) of the $[70,1^-]$ spin-flavor $SU(6)$ -
159 supermultiplet in a combined analysis of the results from both $N\pi$ and $N\pi\pi$ channels.

160 Studies of the combined CLAS preliminary results on $\pi^+\pi^-$ photo- and electroproduction
161 [1] within the framework of the JM meson-baryon reaction model have provided further
162 convincing evidences for the existence of the new baryon state $N'(1720)3/2^+$ [22]. So far,
163 it is the only candidate state, for which information on the internal structure has become
164 available from results on $\gamma_vp \rightarrow N^*$ electrocouplings at $Q^2 < 1.5$ GeV 2 . However, right now,
165 only four data points for this new state's electrocouplings are available. From the data of
166 this analysis note, the $N'(1720)3/2^+$ electrocoupling values will become available at the set
167 of additional Q^2 bins of bin size at least a factor of six smaller than available from the old
168 CLAS experiment [1]. The expected results will for the first time offer a deep insight to the
169 structure of the new baryon state $N'(1720)3/2^+$.

170 The expected results will extend considerably the available information on the interplay
171 between meson-baryon cloud and quark core contributions to the structure of excited nucleon
172 states in particular in mass range from 1.6 to 1.8 GeV.

¹⁷³ **Chapter 2**

¹⁷⁴ **Event selection**

¹⁷⁵ The data reported in this analysis were taken during the e1e run periods in the Hall B during
¹⁷⁶ November 2002 - January 2003 that included several configurations (hydrogen and deuterium
¹⁷⁷ targets as well as two different beam energies of 1 GeV and 2.039 GeV). The torus current
¹⁷⁸ was 2250 A and the mini torus current 5995 A. This particular analysis is concentrated on
¹⁷⁹ the data obtained with the 2 cm long liquid hydrogen target located at -0.2 cm along z-axis,
¹⁸⁰ a 2.039 GeV polarized electron beam, and the CLAS detector. The run numbers' range of
¹⁸¹ this experimental setup is 36118 - 36512. There is a gap in the run numbering between runs
¹⁸² 36160 and 36387, which coincides with Christmas and New Year of 2002-2003 and is most
¹⁸³ likely connected to a database server glitch (there are no entries in the database nor files
¹⁸⁴ on the silo associated with run numbers in this gap). Totally about 1.5 billion triggers over
¹⁸⁵ a month of a beamtime were accumulated. The list of full and empty target runs that are
¹⁸⁶ used in the analysis is presented in Tab. 2.1.

Full target runs	Empty target runs
36117–36122, 36125–36129, 36133–36142	35124
36144, 36145, 36147–36150, 36152–36154	36428
36156, 36158–36160, 36429–36434	36495
36437, 36441–36447, 36449, 36450	
36452–36454, 36458–36467, 36469	
36473–36478, 36480–36482, 36484–36492	
36497–36503, 36505–36511	

Table 2.1: List of the runs that are used in the analysis.

¹⁸⁷ 2.1 Particles identification

¹⁸⁸ In this analysis the first in time particle that gives signals in all four parts of the CLAS
¹⁸⁹ detector is chosen as electron candidate for each event. To identify hadrons only signals in
¹⁹⁰ drift chambers and time-of-flight system are required.

¹⁹¹ All data accumulated during the run is stored in BOS [23] files. For all events selected
¹⁹² for analysis the number of geometrically reconstructed particles (*gpart*) was required to be
¹⁹³ greater than zero. The *gpart* variable is extracted from variable *NPGP* in HEVT bank
¹⁹⁴ according to 2.1.1.

$$NPGP = (\text{Number of final reconstructed particles}) \times 100 + gpart \quad (2.1.1)$$

¹⁹⁵ One more requirement is that the status word (*stat*) is greater than zero (variable *Status*
¹⁹⁶ in EVNT bank).

¹⁹⁷ Then, as mentioned above, for electron candidates signals in all four detectors are required
¹⁹⁸ (all variables *DCStat*, *CCStat*, *SCStat*, *ECStat* from EVNT bank must be greater than
¹⁹⁹ zero). For hadrons only the variables *DCStat* and *SCStat* from EVNT bank are required
²⁰⁰ to be greater than zero.

²⁰¹ Finally the corresponding charge for all particle candidates (variable *Charge* from EVNT
²⁰² bank) is required to be plus or minus one depending on the particle candidate's type.

²⁰³ 2.1.1 Electron identification

²⁰⁴ Firstly electromagnetic calorimeter (EC) and Čerenkov counter (CC) responses need to be
²⁰⁵ checked, to select good electrons from the electron candidates.

²⁰⁶ EC cuts

²⁰⁷ On the hardware level the calorimeter threshold was set to cut off events as close as possible
²⁰⁸ to the kinematic edges of the W and Q^2 domain covered by the measurement, but far enough
²⁰⁹ to keep the low energy contamination within reasonable limits. To select good electrons more
²¹⁰ precisely an additional calorimeter threshold cut on the software level is applied. This cut
²¹¹ accounts for the minimal momentum of the scattered electron that can be reconstructed
²¹² ($P_{e'} > 0.461$ GeV) and is chosen according to [24].

²¹³ Then an additional cut (the so-called sampling fraction cut) was applied to eliminate in
²¹⁴ part pion contamination. To develop this cut the fact that electrons and pions have differ-
²¹⁵ ent energy deposition patterns in EC was used. An electron produces an electromagnetic
²¹⁶ shower, where the deposited energy is proportional to the electron momentum, while a π^-

as minimum ionizing particle loses a constant amount of energy per scintillator (2 MeV/cm) independently of its momentum. In Fig. 2.1 total energy deposited in EC divided by the particle momentum is shown as function of particle momentum. The six plots represent six CLAS sectors. Events between the red curves are selected as good electron candidates for further analysis. The vertical red line at $P_{e'} = 0.461$ GeV shows EC threshold cut. The upper and lower red curves are obtained in the following way: x-slices of 2D histograms are fit by Gaussians. In this way points that correspond to the positions of the fit maxima $\pm 3\sigma$ are obtained. These points determine the upper and lower boundaries for the cut. Finally, to obtain smooth curves, all points are fit by a second order polynom.

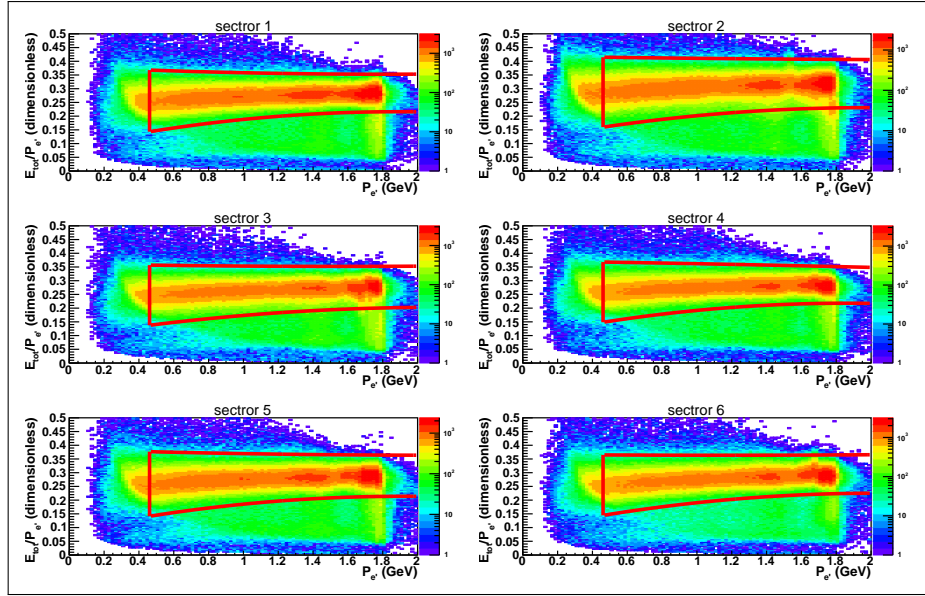


Figure 2.1: Sampling fraction distributions for the data. Six plots correspond to six CLAS sectors. Events between red curves are selected for further analysis.

Both cuts on minimal electron energy and on sampling fraction are applied both to experimental and Monte Carlo events. Since the Monte Carlo simulation does not reproduce electromagnetic showers good enough, the sampling fraction cuts for the simulation, obtained using the same procedure as for the data, look slightly different (see Fig. 2.2).

In Fig. 2.3 the energy deposited in the outer part of EC versus the energy deposited in the inner part of EC is shown before (left plot) and after (right plot) final electron identification. As it is seen in this plot the spot in the left bottom corner that corresponds to the pion contamination disappears that verifies the reliability of the electron selection.

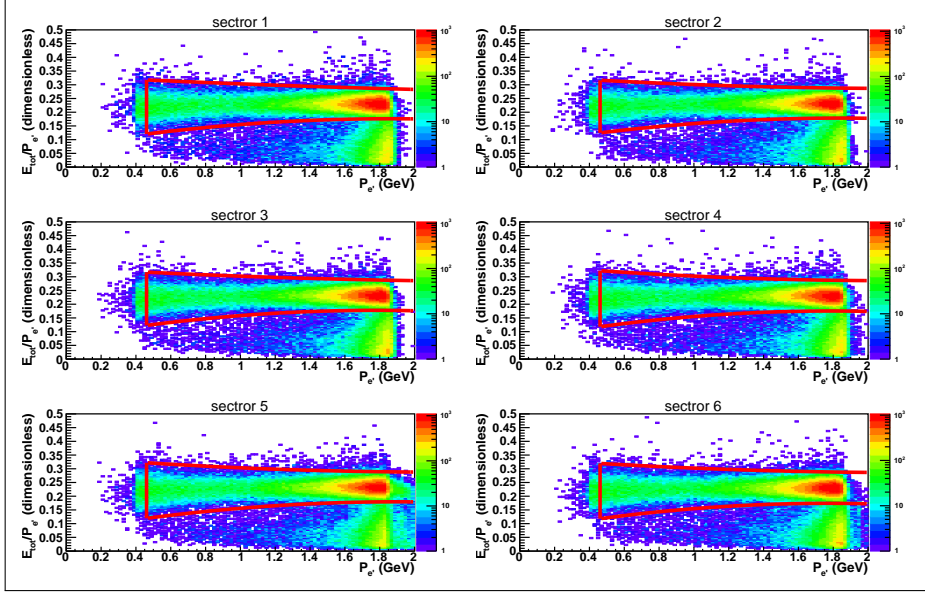


Figure 2.2: Sampling fraction distributions for Monte Carlo. Six plots correspond to six CLAS sectors. Events between red curves are selected for further analysis.

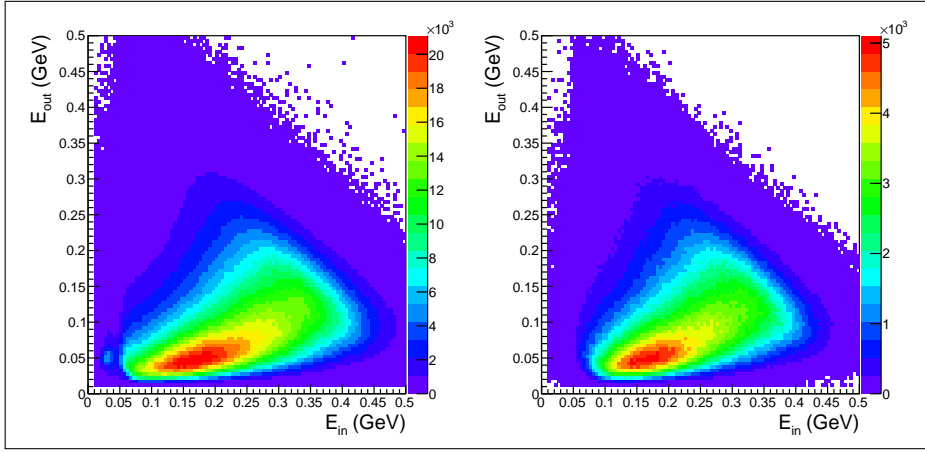


Figure 2.3: Energy deposited in the outer part of EC versus energy deposited in the inner part of EC before (left plot) and after (right plot) final electron selection.

²³⁴ **CC cuts**

²³⁵ To improve the quality of electron candidate selection and π^-/e^- separation a Čerenkov
²³⁶ counter is used. In this experiment the Čerenkov counter had inhomogeneously distributed
²³⁷ zones with partially low detection efficiency. For that purpose a geometrical cut for the
²³⁸ removal of CC low efficiency zones is established. This cut is defined in the plane of Čerenkov
²³⁹ counter. Since polar and azimuthal angles ($\theta_{cc}, \varphi_{cc}$) in the CC plane are not directly defined
²⁴⁰ in the BOS banks [23] some calculations were made to derive these angles from variables
²⁴¹ available in DCPB bank. Fig. 2.4 illustrates these calculations.

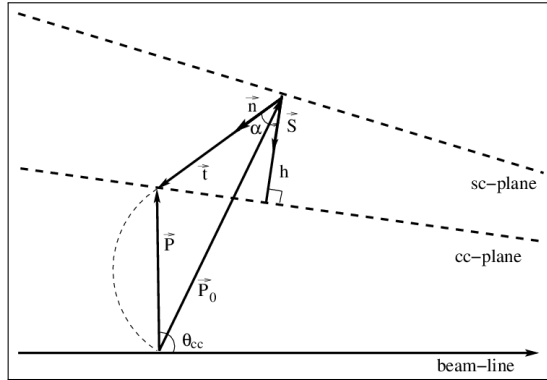


Figure 2.4: Calculation of polar θ_{cc} and azimuthal φ_{cc} angles in the CC plane using variables that are available in DCPB bank.

²⁴² The equation 2.1.2 of the CC plane is known from [25]:

$$\begin{aligned} Ax + By + Cz + D &= 0, \\ D &= 1., \\ A &= -0.000785, \\ B &= 0, \\ C &= -0.00168, \\ \vec{S} &= (A, B, C) \end{aligned} \tag{2.1.2}$$

²⁴³ The distance (h) from the SC hit point to the CC plane (see Fig. 2.4) is then given by

$$h = \frac{(\vec{S} \cdot \vec{P}_0) + D}{|\vec{S}|}, \tag{2.1.3}$$

²⁴⁴ where components of \vec{P}_0 are available in DCPB bank (x_{sc}, y_{sc}, z_{sc}). A tangent to the
²⁴⁵ particle track at the point of intersection with the CC plane (\vec{t}) is shown in Fig. 2.4 by a

²⁴⁶ dashed line and can be written as

$$|\vec{t}| = \frac{h}{\cos(\alpha)}. \quad (2.1.4)$$

²⁴⁷ In turn $\cos(\alpha)$ can be calculated as 2.1.5.

$$\cos(\alpha) = \frac{(\vec{n} \cdot \vec{S})}{|\vec{S}|}, \quad (2.1.5)$$

²⁴⁸ where \vec{n} is a unit vector in \vec{t} -direction based on the DCPB bank variables (cx_sc, cy_sc, cz_sc).
²⁴⁹ It needs to be mentioned that there is no magnetic field between the CC and SC planes, so
²⁵⁰ after hitting the CC plane the particle moves along the \vec{t} -vector.

²⁵¹ It is easy to see in Fig. 2.4 that the vector \vec{P} , which goes from the interaction vertex to
²⁵² the track intersection with the CC plane, is $\vec{P} = \vec{P}_0 + \vec{t}$. Therefore, the angles θ_{cc} and φ_{cc}
²⁵³ can be calculated by 2.1.6 and 2.1.7, respectively.

$$\theta_{cc} = \arccos \left(\frac{P_z}{|\vec{P}|} \right) \quad (2.1.6)$$

$$\begin{aligned} \varphi_{cc} &= \arctan \left(\frac{P_y}{P_x} \right) & \text{if } P_x > 0, P_y > 0 \\ \varphi_{cc} &= \arctan \left(\frac{P_y}{P_x} \right) + 2\pi & \text{if } P_x > 0, P_y < 0 \\ \varphi_{cc} &= \arctan \left(\frac{P_y}{P_x} \right) + \pi & \text{if } P_x < 0, P_y < 0 \\ \varphi_{cc} &= \arctan \left(\frac{P_y}{P_x} \right) + \pi & \text{if } P_x < 0, P_y > 0 \\ \varphi_{cc} &= \frac{\pi}{2} & \text{if } P_x = 0, P_y > 0 \\ \varphi_{cc} &= \frac{3\pi}{2} & \text{if } P_x = 0, P_y < 0 \end{aligned} \quad (2.1.7)$$

²⁵⁴ After the angles in the CC plane are defined, distributions φ_{cc} vs. θ_{cc} are plotted for each
²⁵⁵ CLAS sector (see Fig. 2.5). The quantity 2.1.8 is shown by the color code in Fig. 2.5. This
²⁵⁶ quantity varies from zero to one and shows the portion of good electrons with number of
²⁵⁷ photoelectrons greater than five inside a $(\theta_{cc}, \varphi_{cc})$ bin. Or in other words how efficient CC
²⁵⁸ is in a given $(\theta_{cc}, \varphi_{cc})$ bin.

$$\frac{\text{number of events inside } (\theta_{cc}, \varphi_{cc}) \text{ bin with more than 5 photoelectrons in CC}}{\text{total number of events inside } (\theta_{cc}, \varphi_{cc}) \text{ bin}} \quad (2.1.8)$$

259 The edges of the distributions in Fig. 2.5 are sharp due to the fiducial cut that is applied
 260 in the CC plane 2.1.9. The shape of this cut is taken from [26].

$$\begin{aligned} \theta_{cc} &> 7.0 + 0.0032\varphi_{cc} + 0.0499\varphi_{cc}^2 \\ \left(\frac{\theta_{cc} - 45.5^\circ}{34.5^\circ}\right)^2 + \left(\frac{\varphi_{cc}}{21^\circ}\right)^2 &\leq 1 \\ \left(\frac{\theta_{cc} - 45.5^\circ}{1.75^\circ}\right)^2 + \left(\frac{\varphi_{cc}}{21^\circ}\right)^2 &> 1 \\ \theta_{cc} &< 45^\circ \end{aligned} \quad (2.1.9)$$

261 The two stripes in sector five in Fig. 2.5 correspond to the inefficient zones that will be
 262 discussed in Sec. 3.1.

263 For further analysis only zones with a ratio 2.1.8 greater than 0.8 are selected. These
 264 zones are shown in black in Fig. 2.6. As it is seen in Fig. 2.6, there is an inefficient zone in
 265 the middle of each sector, that is expected since two CC mirrors are joined there.

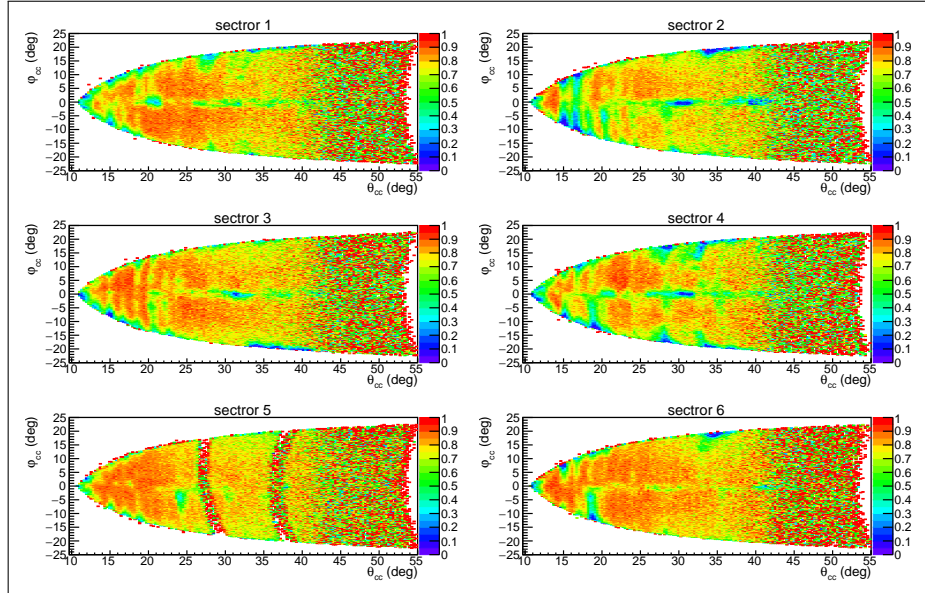


Figure 2.5: Distributions of the quantity 2.1.8 as function of the polar (θ_{cc}) and azimuthal (φ_{cc}) angles in the CC plane for six CLAS sectors.

266 After the geometrical cut shown in Fig. 2.6 is applied photoelectron distributions are
 267 plotted for each PMT on the left and right sides of each CC segment and for each CLAS
 268 sector (see Fig. 2.7). The segment number and *index* that indicates which side PMT was
 269 fired are taken from the CCPB bank *Status* variable according to

$$Status = 10 \times (\text{CC segment number}) + 1000 \times (1 + index), \quad (2.1.10)$$

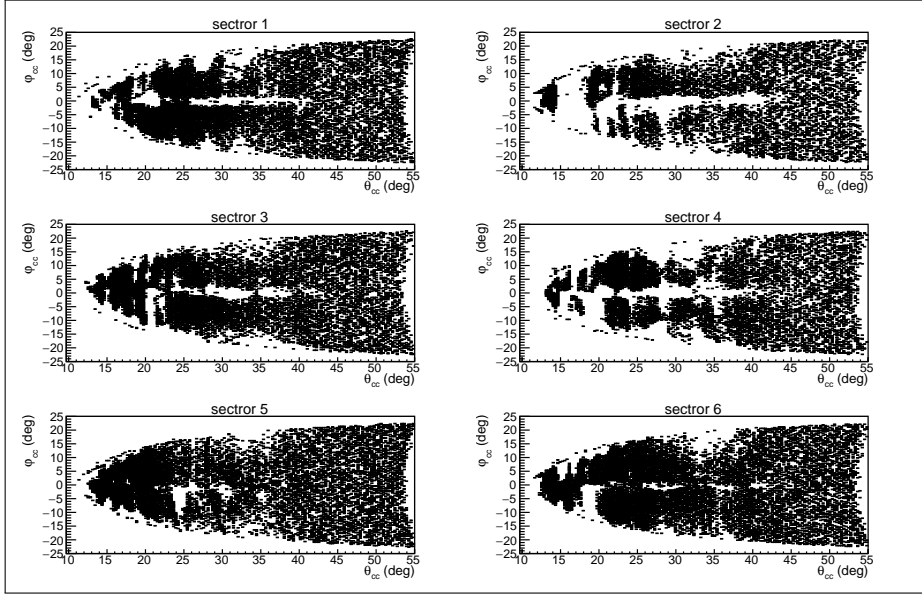


Figure 2.6: Zones where CC is efficient enough to accept good electron candidates are shown in black as function of the polar (θ_{cc}) and azimuthal (φ_{cc}) angles in the CC plane for six CLAS sectors.

270 where *index* is 1 for right PMTs, -1 for left PMTs, and 0 for the case when both PMTs were
271 fired.

272 As it is seen in Fig. 2.7, there are some peaks at low number of photoelectrons. These
273 peaks correspond to π^- contamination and/or noise in PMTs [25]. To eliminate events under
274 this peak all events on the left side of the red vertical line in Fig. 2.7 are excluded from the
275 analysis.

276 Since Monte Carlo does not reproduce photoelectron distributions well enough, the cut
277 shown by the red line in Fig. 2.7 is applied only to the data. To recover good electrons that
278 were cut off in this way a special procedure is developed. The part of the distributions on
279 the right side of the red line is fit by function 2.1.11, which is a slightly modified Poisson
280 distribution.

$$y = P_1 \left(\frac{P_3^{\frac{x}{P_2}}}{\Gamma \left(\frac{x}{P_2} + 1 \right)} \right) e^{-P_3} \quad (2.1.11)$$

281 The fitting function is then continued into the region on the left side of the red line. In
282 this way the two regions, shown by blue and green in Fig. 2.7, are determined. Finally the
283 correction factors are defined by 2.1.12 and applied as a weight for each event which goes to
284 the particular PMT.

$$F_{ph. el.} = \frac{\text{green area} + \text{blue area}}{\text{green area}} \quad (2.1.12)$$

285 It needs to be mentioned that segments one, two, and 18 are removed from the analysis
 286 completely since they are dominated by events with very low number of photoelectrons. The
 287 procedure described above is applied for left and right side PMTs. For the events with both
 288 PMTs fired the peak at low number of photoelectrons is almost absent and no additional
 289 cut like this is needed.

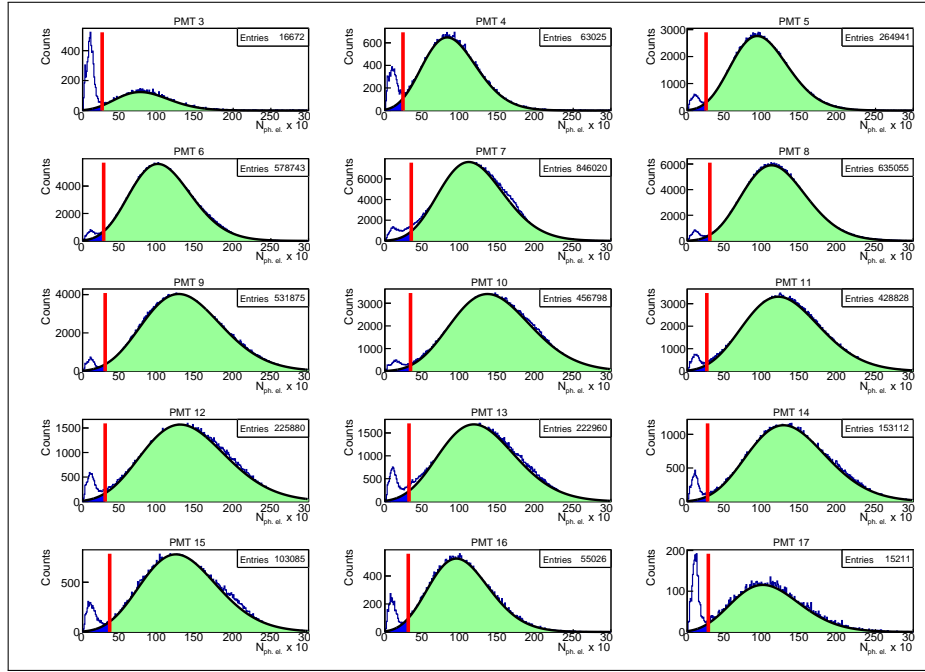


Figure 2.7: Number of photoelectrons multiplied by ten for the left side of sector one of CC. Various plots correspond to various CC segments. Black curves show the fit by function 2.1.11. Red vertical lines show the applied cut. Regions that are needed to calculate the ratio 2.1.12 are shown in blue and green.

290 2.1.2 Hadron identification

291 The CLAS time-of-flight (TOF) system provides information on particle velocity ($\beta = v/c$).
 292 The information from the Drift Chambers allows to measure the particle momentum (P).
 293 Therefore, charged hadron can be identified using the relation between particle mass, mo-
 mentum, and velocity

$$\beta = \frac{p}{\sqrt{p^2 + m^2}}. \quad (2.1.13)$$

295 For the hadron identification, only events with electron candidates that have been selected
 296 in the previous step are used. β versus momentum distributions are plotted for each TOF

297 scintillator in each CLAS sector (see example plots for CLAS sector one in Fig. 2.8 for
 298 positively charged particles and in Fig. 2.9 for preliminary selected π^- candidates).

299 It needs to be mentioned that in order to simplify the analysis process the preliminary
 300 particle id was made on an initial step of converting data from the BOS files to the files with
 301 ROOT trees. It leads to the fact that in Figure 2.9 only the region that corresponds to the
 302 preliminary selected π^- candidates is filled with events.

303 For visual identification of improperly working scintillation bars, theoretical curves with
 304 hadron 2.1.13 (π^+ , π^- , proton) proper mass assumptions are plotted. As it can be seen in the
 305 plots paddle number 48 has enormous number of events. It happened most likely, because
 306 more paddles of TOF were connected to TDC 48 or due to cooking problems. Therefore,
 307 paddles 48 are excluded from the analysis. Besides scintillators number 17 in sectors two
 308 and five worked improperly and are also excluded from the analysis.

309 Events between purple dashed curves in Fig. 2.8 and Fig. 2.9 are selected as π^+ and π^-
 310 candidates, respectively. Analytical formulae for these curves are given in 2.1.14.

$$\begin{aligned} \beta &< \frac{(205.98 - P_{hadron}) \left(\frac{200 - P_{hadron}}{200 + P_{hadron}} \right)^{0.7} (P_{hadron} + 0.5)}{(200.02 + P_{hadron}) \sqrt{(P_{hadron} + 0.5)^2 + 0.019}} + 0.019 \\ \beta &> \frac{(1 + 5 \times 1.07 \times (P_{hadron} - 0.07))(P_{hadron} - 0.07)}{(1 + 5(P_{hadron} - 0.07)) \sqrt{(P_{hadron} - 0.07)^2 + 0.138^2}} - 0.1 \end{aligned} \quad (2.1.14)$$

311 For proton candidates the selection cuts 2.1.15 are used. They are shown by the red
 312 dashed lines in Fig. 2.8.

$$\begin{aligned} \beta &< \left(\frac{P_{hadron}}{\sqrt{P_{hadron}^2 + 0.938^2}} + 0.02 \right) \frac{1.2 + 0.92P_{hadron}}{1 + P_{hadron}} \\ \beta &> \left(\frac{P_{hadron}}{\sqrt{P_{hadron}^2 + 0.938^2}} - 0.05 \right) \frac{1 + P_{hadron}}{0.9 + 1.06P_{hadron}} \end{aligned} \quad (2.1.15)$$

313 As seen in Figs. 2.8 and 2.9 some scintillators with numbers larger equal 40 have two
 314 bands (both of them most likely correspond to the given hadron). The origin of these two
 315 bands can be based on mistakes in data cooking/calibration or the consequence of the fact
 316 that two scintillation bars are connected to one TDC. For this large-number scintillators all
 317 events laying higher than the upper cut for protons are assumed to be pions.

318 2.1.3 Timing correction

319 Another approach can be used to treat the scintillators with numbers larger equal 40, which
 320 have two bands that correspond to the same hadron. The idea of this approach is to plot

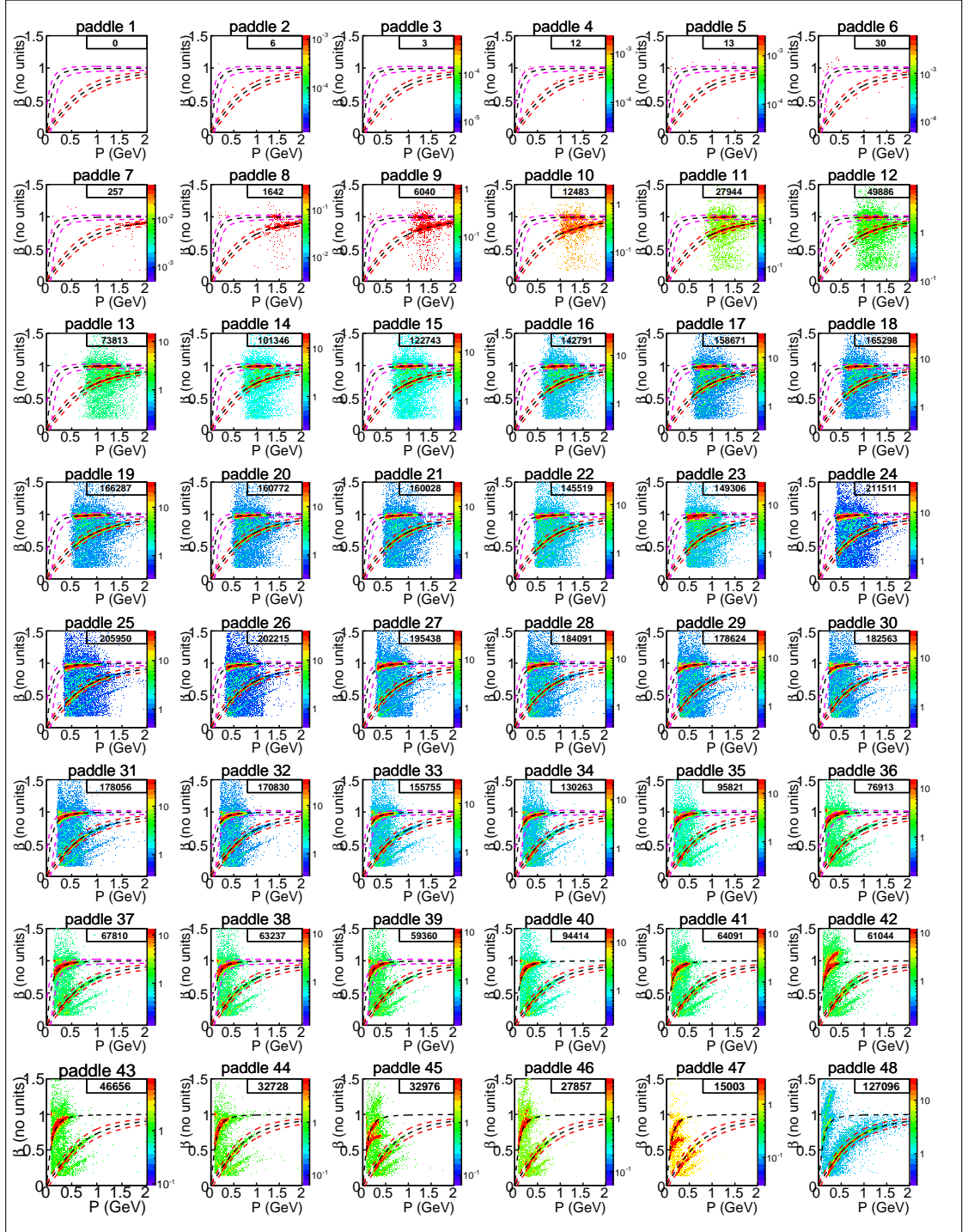


Figure 2.8: β versus momentum distributions for positively charged particles for different TOF scintillators in CLAS sector one. Black dashed curves are theoretical under the exact hadron mass assumption 2.1.13. Events between the two purple dashed 2.1.14 and two red dashed 2.1.15 curves are selected as π^+ and proton candidates, respectively. For scintillators with number greater equal 40 all events laying higher than the upper red dashed curve are assumed as π^+ candidates. Number of events is shown in the right upper corner of each plot.

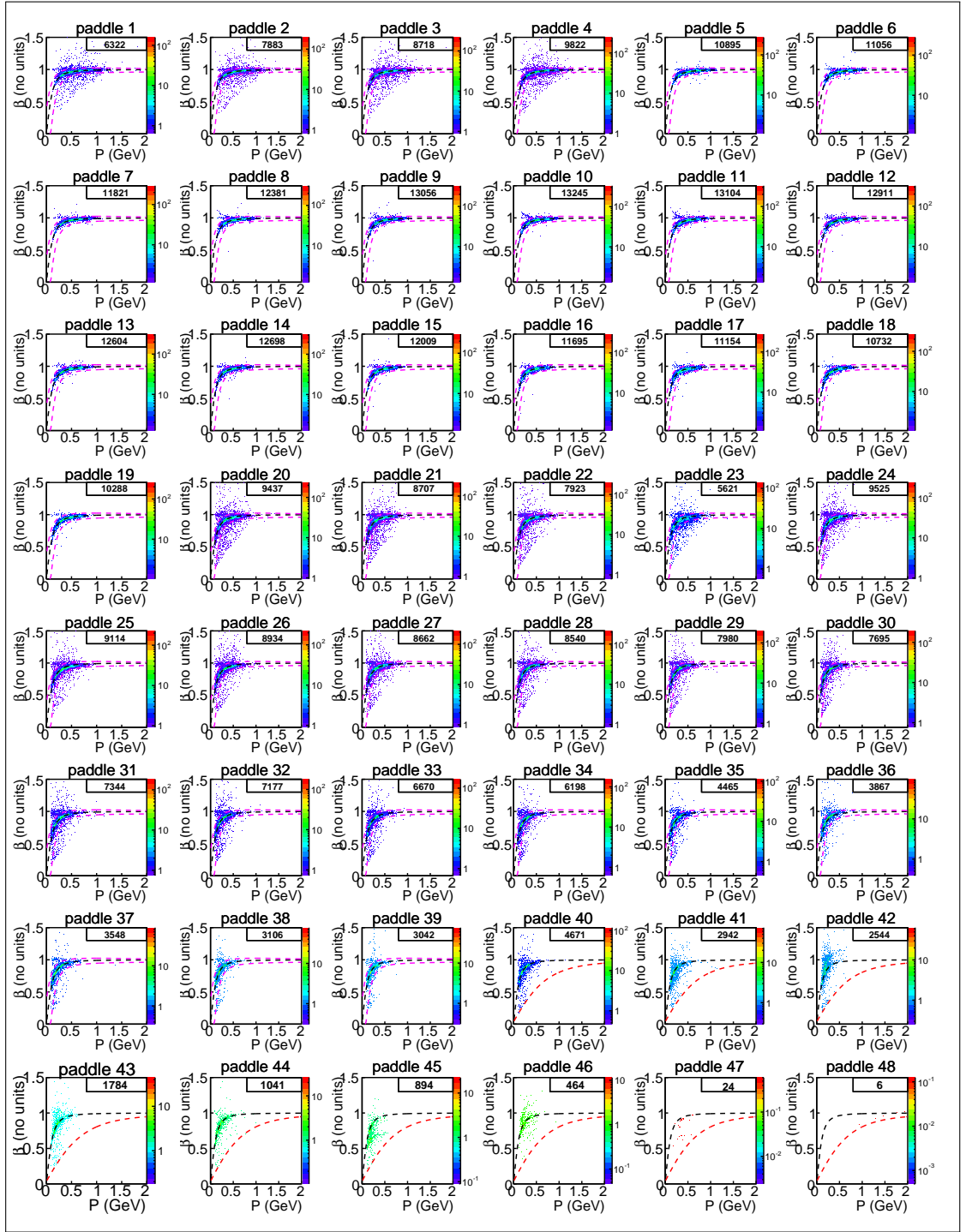


Figure 2.9: β versus momentum distributions for negatively charged particles for different TOF scintillators in CLAS sector one. Black dashed curves are theoretical under the exact π^- mass assumption 2.1.13. Events between the two purple dashed 2.1.14 curves are selected as π^- candidates. For scintillators with number greater equal 40 all events laying higher than the red dashed curve are assumed as π^- candidates. Number of events is shown in the right upper corner of each plot.

321 the difference between the measured time that hadron travels between the target and the
 322 SC plane and the same quantity calculated under the exact hadron mass assumption. This
 323 time difference ΔT is calculated as:

$$\Delta T = \frac{l_h}{c} \left(\frac{1}{\beta_n} - \frac{1}{\beta_{old}} \right), \quad (2.1.16)$$

324 where l_h is the hadron path length from the vertex to the SC plane (the *Path* variable in
 325 DCPB bank), β_n is the nominal β with the exact mass of the hadron assumed (see Eq. 2.1.13),
 326 β_{old} is the value of β that needs to be corrected, c is the speed of light.

327 In the left side in Fig. 2.10 ΔT is plotted for the π^+ candidates for the paddle 42 in
 328 CLAS sector one as a function of their momentum. The two horizontal bands are clearly
 329 seen in this figure. One of them is around $\Delta T = 0$, while another one is shifted by two nano
 330 seconds and corresponds to the wrong band in β versus momentum distribution for paddle
 331 42 (see Fig. 2.8).

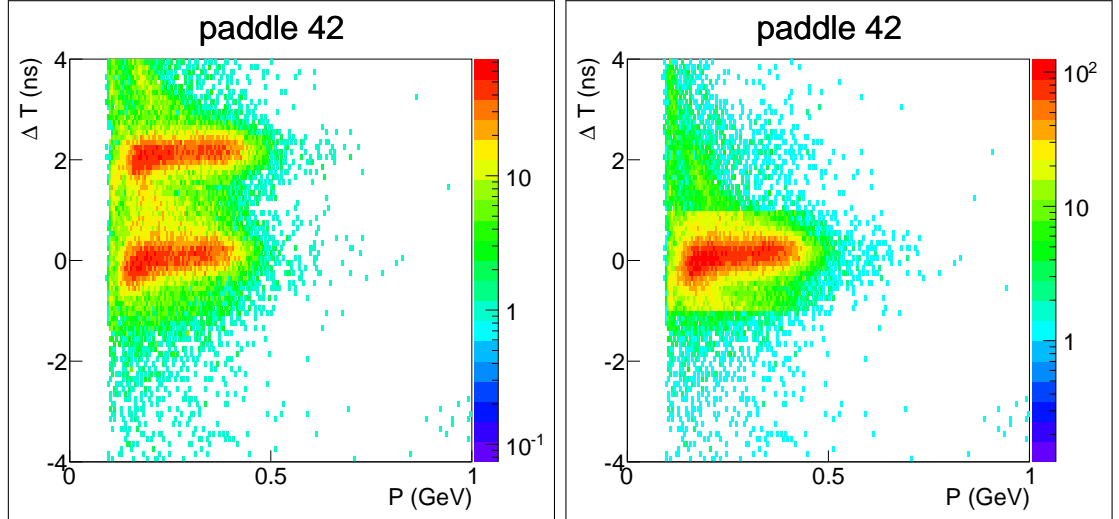


Figure 2.10: Quantity ΔT that is given by Eq. 2.1.16 before (left plot) and after (right plot) the timing corrections.

322 The idea of timing corrections is to shift the wrong bands in ΔT versus momentum
 323 distributions to their correct position around $\Delta T = 0$. The result of this shift is shown in
 324 the right side in Fig. 2.10. After this shift the correct value of β is calculated using Eq. 2.1.17.

$$\beta_{corr} = \frac{1}{\frac{1}{\beta_n} - \frac{(\Delta T - t_{max})c}{l_h}}, \quad (2.1.17)$$

335 where t_{max} is the position of each wrong band, 2 ns in the example shown in Fig. 2.10.

After applying the procedure that is described above for all pion candidates in all problematic paddles with double bands, the β versus momentum distributions are plotted, see Fig. 2.11. As it is seen in Fig. 2.11 there are no paddles with double bands anymore. So, even for scintillators with the numbers greater equal 40 the same β versus momentum cuts (see Eq. 2.1.14) can be applied. This procedure is performed for pion candidates only, since the effect of the band doubling in the β versus momentum distributions for the protons is rather small and all proton candidates are lying inside the cut given by Eq. 2.1.15 even without timing corrections.

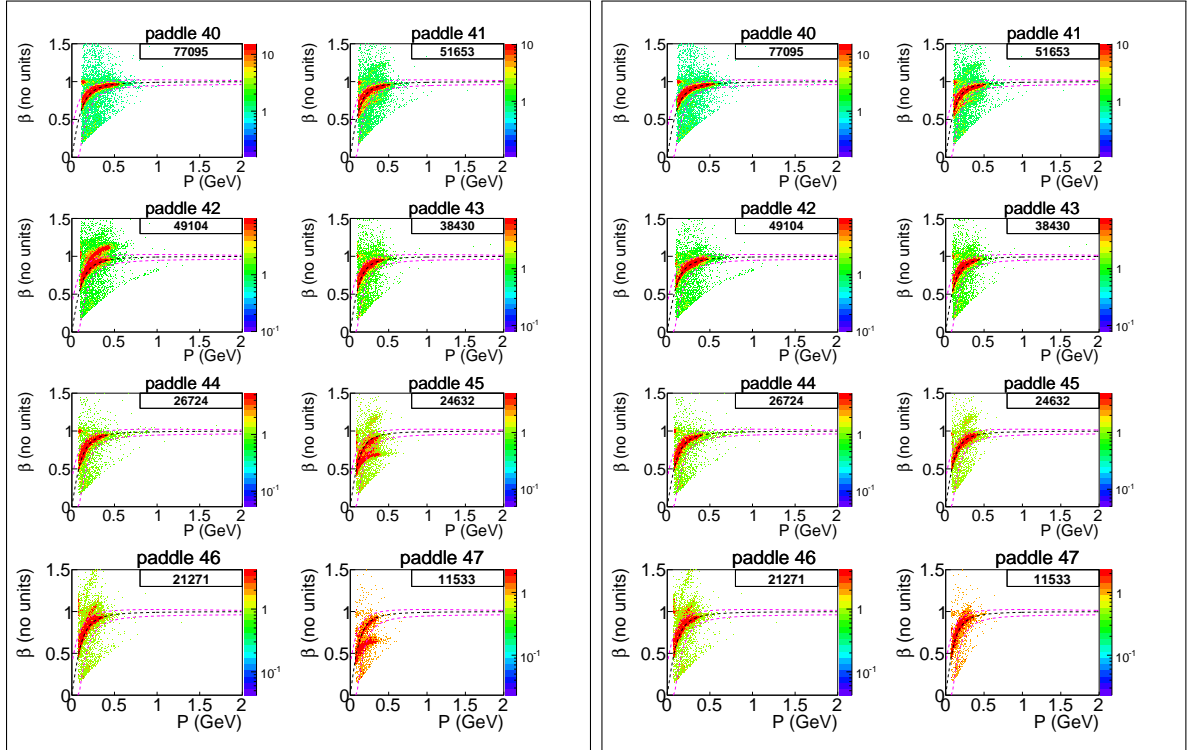


Figure 2.11: β versus momentum distributions before (left plot) and after (right plot) the timing corrections for π^+ . Only scintillators in CLAS sector one with number larger than 40 are shown. Black dashed curves are theoretical under the exact π^+ mass assumption 2.1.13. Events between the two purple dashed 2.1.14 and two red dashed 2.1.15 curves are selected as pions. Number of events is shown in the right upper corner of each plot.

Both methods of hadrons identification that are described in the previous and this sections have been compared and it is found that they give pretty small difference in the cross sections. Nevertheless, the final cross sections presented in this analysis are obtained using the timing corrections described in this section.

348 2.2 Momentum corrections

349 2.2.1 Electron momentum correction

350 Due to the slight misalignments in the DC position, small inaccuracies in the description of
 351 the torus magnetic field, and other possible reasons the momentum and angle of particles
 352 may have some small systematic deviations from the real values. Since the effects are of
 353 unknown origin, they cannot be simulated in GSIM. Hence a special momentum correction
 354 procedure is needed for the data. The approach [27], which is based on elastic kinematic,
 355 was chosen for this purpose.

356 Low beam energy ~ 2 GeV of analyzed dataset leads to the small shift (~ 3 MeV) in
 357 elastic peak position. For comparison for 6 GeV runs this shift is about 20 MeV. From [27]
 358 it is known that momentum corrections are essential only for high-energetic particles. Since
 359 in 2π kinematics hadrons carry only small portion of the system momentum, the expected
 360 momentum corrections for them are significantly less than for electrons and can be neglected.

361 In Fig. 2.12 elastic peak positions are shown for six CLAS sectors before (left panel)
 362 and after (right panel) electron momentum correction. The peaks are fit by Gaussians with
 363 polynomial background, fitting curves are shown in Fig. 2.12, and the fit parameter p_1
 364 corresponds to the elastic peak position. As seen in Fig. 2.13, elastic peak positions for all
 365 CLAS sectors get closer to the proton mass, shown by red horizontal line. The momentum
 366 resolution for electrons can be roughly estimated from elastic peak width that is about nine
 367 MeV.

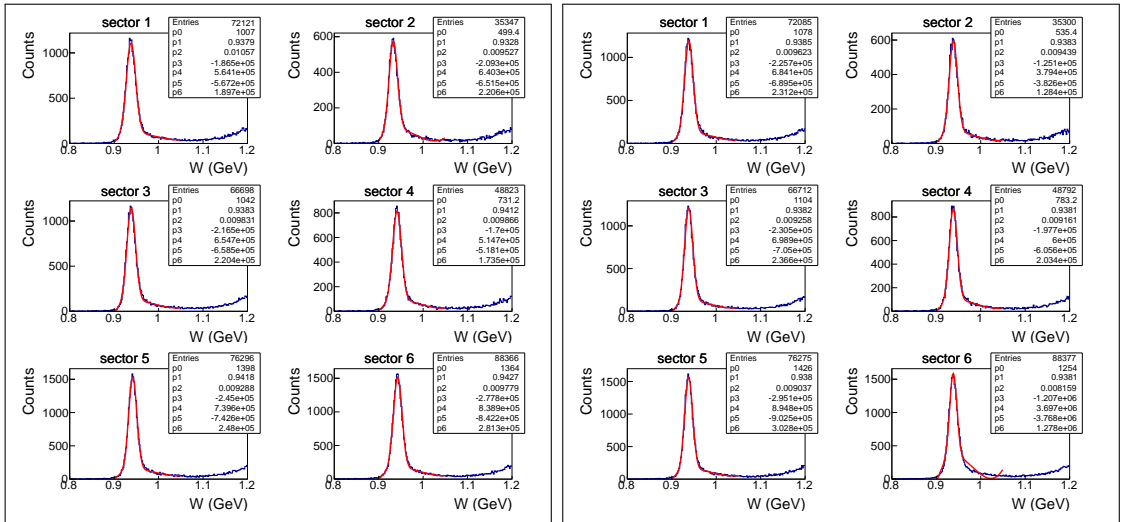


Figure 2.12: Elastic peaks for six CLAS sectors before (left panel) and after (right panel) electron momentum correction. Fit parameter p_1 corresponds to elastic peak position.

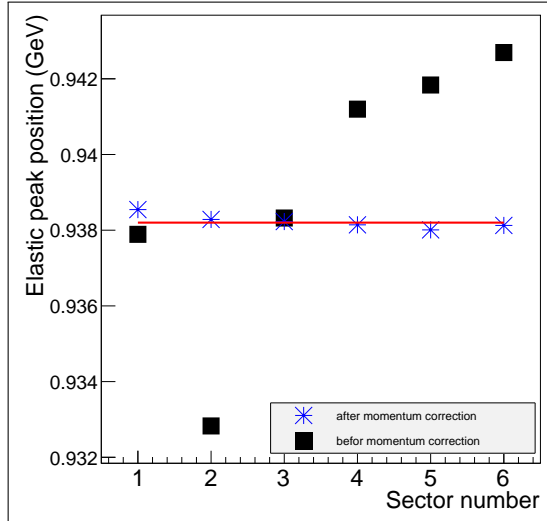


Figure 2.13: Elastic peak position for six CLAS sectors before (black squares) and after (blue stars) electron momentum correction. Horizontal red line shows the proton mass.

368 Due to unknown reasons (most likely because electrons lose energy when they travel
 369 through the detector and target media) the reconstructed electron momentum appears to
 370 be slightly lower than the generated one. Therefore, an adapted electron momentum correc-
 371 tion procedure is also applied to the Monte Carlo events. This correction depends only on
 372 scattered electron angle θ and momentum, but not on the CLAS sector. Figure 2.14 shows
 373 differences between thrown and reconstructed electron momenta before and after the correc-
 374 tion procedure. As shown in Fig. 2.14, these differences become negligible after momentum
 375 corrections have been applied.

376 2.2.2 Proton momentum correction (Energy loss)

377 While traveling through the detector and the target, the proton loses part of its energy due
 378 to interaction with media, hence the measured momentum is lower than the one the proton
 379 actually had right after the interaction. This effect is especially important for the low-
 380 energy protons and can lead to misdetermination of various kinematical quantities. GSIM
 381 simulation of the CLAS detector correctly propagates protons through the media and is used
 382 to account for this effect by using both information about the generated and reconstructed
 383 protons.

384 To obtain the correction function, event distributions for the differences between gener-
 385 ated and reconstructed proton momenta are binned in proton momentum and proton angle
 386 θ and fit by Gaussians. The in this way obtained peak positions are fit as function of proton
 387 momentum and proton angle θ . The results are shown in Fig. 2.15. The function shown in

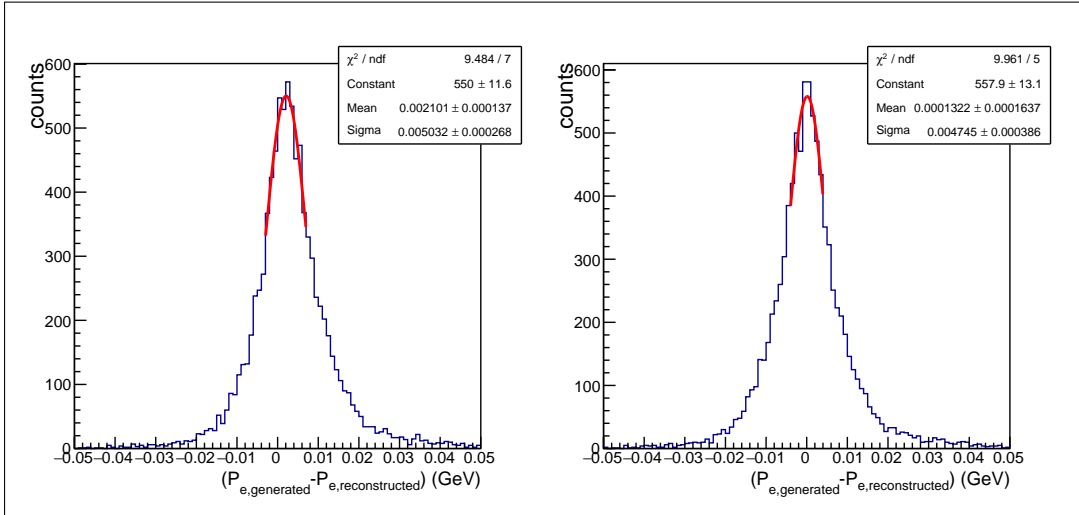


Figure 2.14: The difference between generated and reconstructed electron momenta before (left plot) and after (right plot) the momentum correction has been applied to the reconstructed electrons.

388 Fig. 2.15 gives the percentage of the momentum that protons lose when they move through
 389 the detector and target media. This function is used to correct the momentum both in the
 390 simulation and the data.

391 It needs to be mentioned that to isolate the pure effect of energy loss, reconstructed
 392 events with and without detector and target material need to be compared. Since in the
 393 used procedure differences between generated and reconstructed events are analyzed, the
 394 correction function shown in Fig. 2.15 can also include other effects that lead to improper
 395 proton momentum reconstruction.

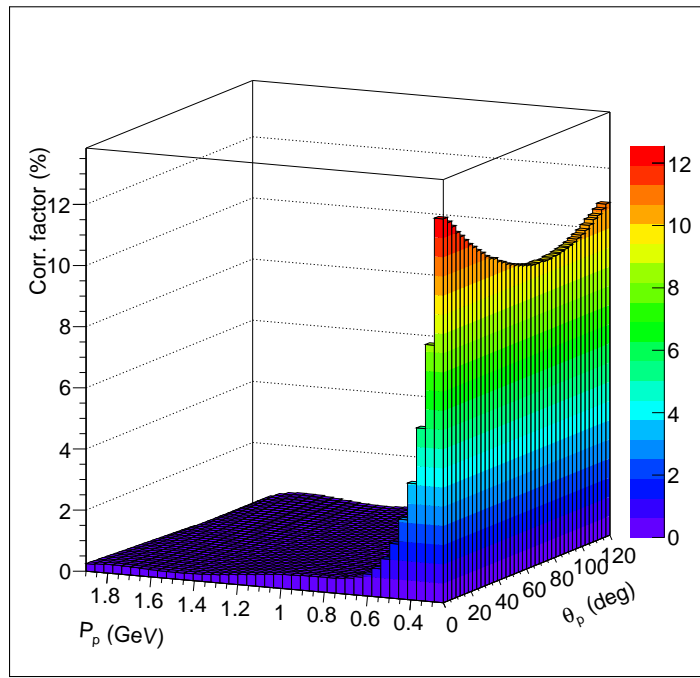


Figure 2.15: The percentage of momentum that protons lose when they move through the detector and target media as a function of the momentum and scattered angle θ of the proton.

³⁹⁶ **Chapter 3**

³⁹⁷ **Other cuts and corrections**

³⁹⁸ **3.1 Fiducial cuts**

³⁹⁹ The CLAS detector has an active detection solid angle that is obviously smaller than 4π .
⁴⁰⁰ This is in part due to the space filled with the torus field coils: the angles covered by the coils
⁴⁰¹ are not equipped with any detection system and therefore form a "dead" area for detection.
⁴⁰² Moreover, different studies and analyses have shown that also the edges of the active area
⁴⁰³ do not provide a safe region for particle reconstruction, being affected by rescattering from
⁴⁰⁴ the coil, field distortions, and similar effects. Therefore it is now common practice to accept
⁴⁰⁵ for the analysis only events inside specific fiducial cuts, i.e. cuts on the kinematic variables
⁴⁰⁶ (momentum and angles) of each particle. This method guarantees that the reconstructed
⁴⁰⁷ events accepted in the analysis include only particles detected in "safe" areas of the detector,
⁴⁰⁸ that is where the acceptance is thought to be well understood. These cuts are applied for
⁴⁰⁹ both real events and Monte Carlo reconstructed events and produce a reduction factor in
⁴¹⁰ the number of events accepted in each kinematic bin that is called detector acceptance.

⁴¹¹ **3.1.1 Fiducial cuts for negatively charged particles**

⁴¹² In the CLAS experiments with the normal direction of the torus magnetic field, like in e1e
⁴¹³ experiment, negatively charged particles are inbending. For that type of particles sector
⁴¹⁴ independent, symmetrical, and momentum dependent cuts are applied. To establish the
⁴¹⁵ shape of these cuts relatively flat areas in φ distributions are selected. For that purpose all
⁴¹⁶ events are binned in the particle momentum and the particle polar angle θ (see Fig. 3.1).
⁴¹⁷ In Fig. 3.1 φ distributions are shown for one slice over momentum and for various bins in
⁴¹⁸ θ for electrons (left side plots) and π^- (right side plots). Events between the vertical lines
⁴¹⁹ in Fig. 3.1 are selected for further analysis. The analytical shape of these cuts is given by

⁴²⁰ Eq. 3.1.1 for electrons and Eq. 3.1.2 for π^-

$$\begin{aligned}
\theta_{min} &= 9.7 + 17/(P_{e'} + 0.2) \\
\delta\varphi_{e'} &= p_1 \sin(p_2(\theta_{e'} - \theta_{min}))^{p_3 + p_4/\theta_{e'} + p_5/\theta_{e'}^2} + p_6 \\
p_1 &= 37.3(0.85 + 1.1P_{e'}) \\
p_2 &= 0.01745 \\
p_3 &= p_1/37.3 \\
p_4 &= -62.8 - 30P_{e'} \\
p_5 &= 1525 \\
p_6 &= 0
\end{aligned} \tag{3.1.1}$$

$$\begin{aligned}
\theta_{min} &= 11 + 8/(0.472P_{\pi^-} + 0.117) \\
\delta\varphi_{\pi^-} &= p_1 \sin(p_2(\theta_{\pi^-} - \theta_{min}))^{p_3 + p_4/\theta_{\pi^-} + p_5/\theta_{\pi^-}^2} + p_6 \\
p_1 &= 30.5 \\
p_2 &= 0.01745 \\
p_3 &= 0.705 + 1.1P_{\pi^-} \\
p_4 &= -63.2 - 33.3P_{\pi^-} \\
p_5 &= 1530 \\
p_6 &= -1
\end{aligned} \tag{3.1.2}$$

⁴²¹ where $P_{e'}$ and P_{π^-} are the momenta of the particles in GeV, $\theta_{e'}$ and θ_{π^-} are the polar angles
⁴²² of the particles in degrees. $\delta\varphi_{e'}$ and $\delta\varphi_{\pi^-}$ are the portions of the polar angle φ accepted by
⁴²³ the fiducial cut, or in other words if $\theta > \theta_{min}$ and $|\varphi| < \delta\varphi$ then the particle is accepted.
⁴²⁴ The functions 3.1.1,3.1.2 are shown in 2D plots φ versus θ in Fig. 3.2 for electrons (left side)
⁴²⁵ and π^- (right side).

⁴²⁶ There are some additional inefficient areas that are not related to the gaps between
⁴²⁷ CLAS sectors. These areas are typically caused by drift chamber and time-of-flight system
⁴²⁸ inefficiencies (dead wires or PMTs). Some of them are reproduced in Monte Carlo simulation,
⁴²⁹ while others are not. To exclude the latter from the analysis additional fiducial cuts on θ
⁴³⁰ versus momentum distributions are applied. These cuts are individual for each CLAS sector.
⁴³¹ They are shown by the black curves for real and Monte Carlo events in Fig. 3.3 for electrons
⁴³² and in Fig. 3.4 for π^- . For the electron distributions in Fig. 3.3 only CLAS sector five is
⁴³³ shown since there are no dead areas in other sectors.

⁴³⁴ 3.1.2 Fiducial cuts for positively charged particles

⁴³⁵ For positively charged particles, which are outbending in the e1e experiment, momentum
⁴³⁶ independent and asymmetrical fiducial cuts are the best choice. These cuts are established

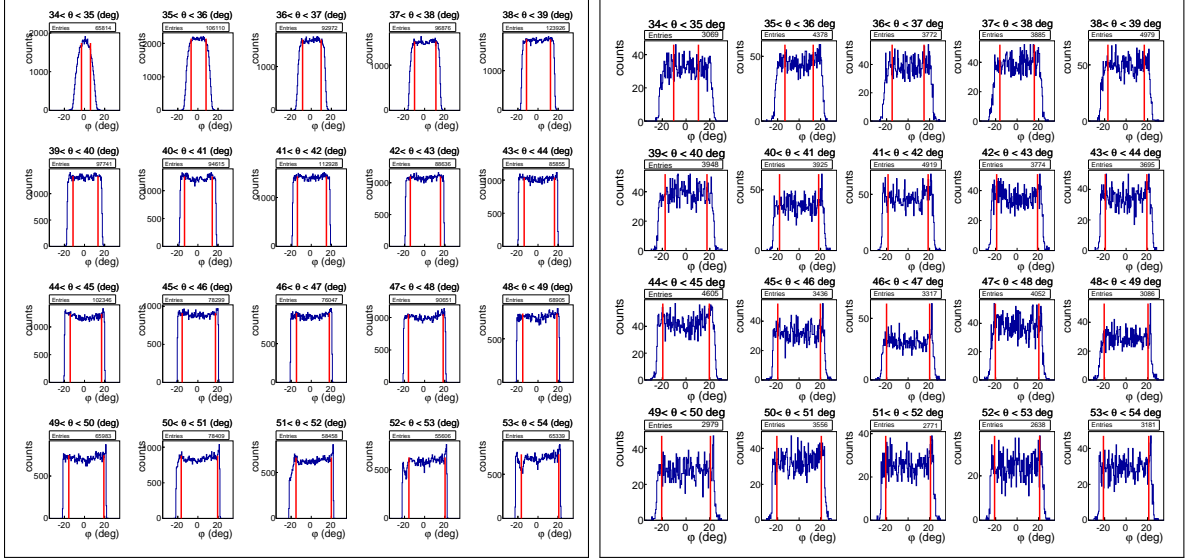


Figure 3.1: φ -event distributions for electrons (left plot) and π^- (right plot). Electrons are shown for CLAS sector 6 and a momentum range from 480 MeV to 560 MeV, while π^- are for sector 3 and a momentum range from 400 MeV to 600 MeV. Various plots represent bins in polar angle θ . Events between the red lines are selected for the analysis.

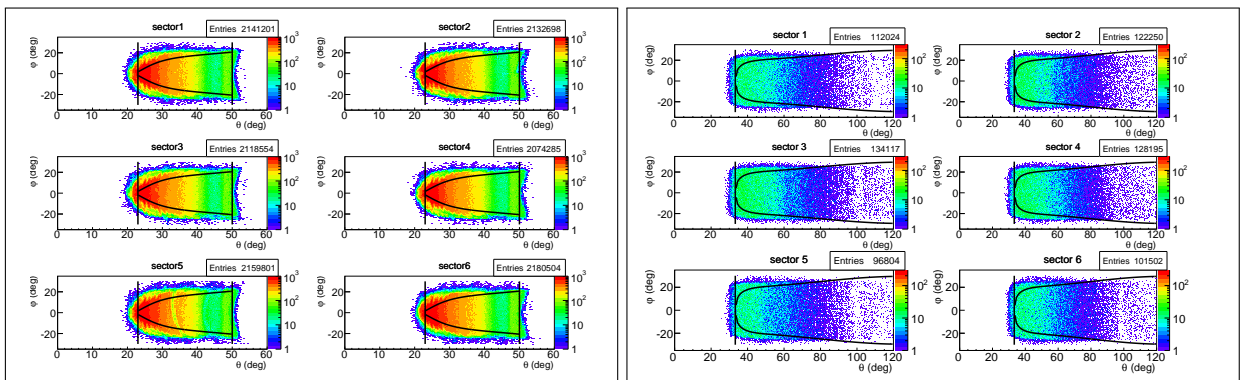


Figure 3.2: φ versus θ distributions for electrons with momenta from 1120 MeV to 1200 MeV (left frame) and π^- with momenta from 400 MeV to 600 MeV (right frame) for all six CLAS sectors. Curves show the applied fiducial cuts, vertical lines stand for minimum and maximum θ cuts.

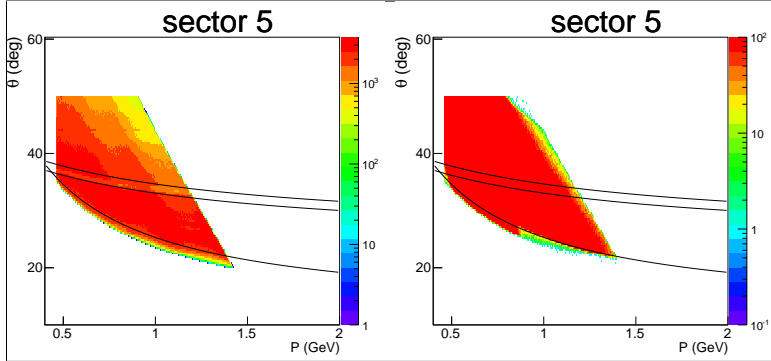


Figure 3.3: θ versus momentum distributions for electrons in CLAS sector five. Left plot shows real and right plot Monte Carlo events. Black curves show cuts applied to remove inefficient areas.

437 in the same way as for negatively charged particles, i.e. by selection of the flat parts of the
 438 event distributions over φ . The shape of these cuts is given by

$$\begin{aligned}\varphi_{upper} &= 24(1 - e^{-0.08(\theta-9)}) \\ \varphi_{lower} &= -25(1 - e^{-0.1(\theta-10)}),\end{aligned}\quad (3.1.3)$$

439 where θ is the particle angle in degrees. φ_{upper} and φ_{lower} are the upper and lower cut
 440 boundaries. Events with $\varphi_{lower} < \varphi < \varphi_{upper}$ are selected for further analysis.

441 This function is superimposed on the 2D φ versus θ distributions of real events and shown
 442 in Fig. 3.5 by the black curves. Additional cuts in θ versus momentum coordinates are shown
 443 by the black curves for Monte Carlo and real events in Fig. 3.6 for protons and in Fig. 3.7
 444 for π^+ .

445 3.2 Data quality check

446 During the quite long experimental run the variations of the experimental conditions, like
 447 the target density deviation or improper operation of some parts of the detector, can lead to
 448 different yields of events. Only parts of the run with relatively stable event rates are selected
 449 for the analysis. For that purpose cuts on DAQ live time and number of events per Faraday
 450 cup (FC) charge are used.

451 FC charge updates with given frequency, so the whole run time can be divided into so-
 452 called *blocks*. Each *block* corresponds to the portion of time between two FC charge readouts.
 453 FC charge readout happens approximately once in ten seconds. The *block* number ranges
 454 from one to the maximum number over the run time. The first and last *blocks* in each run

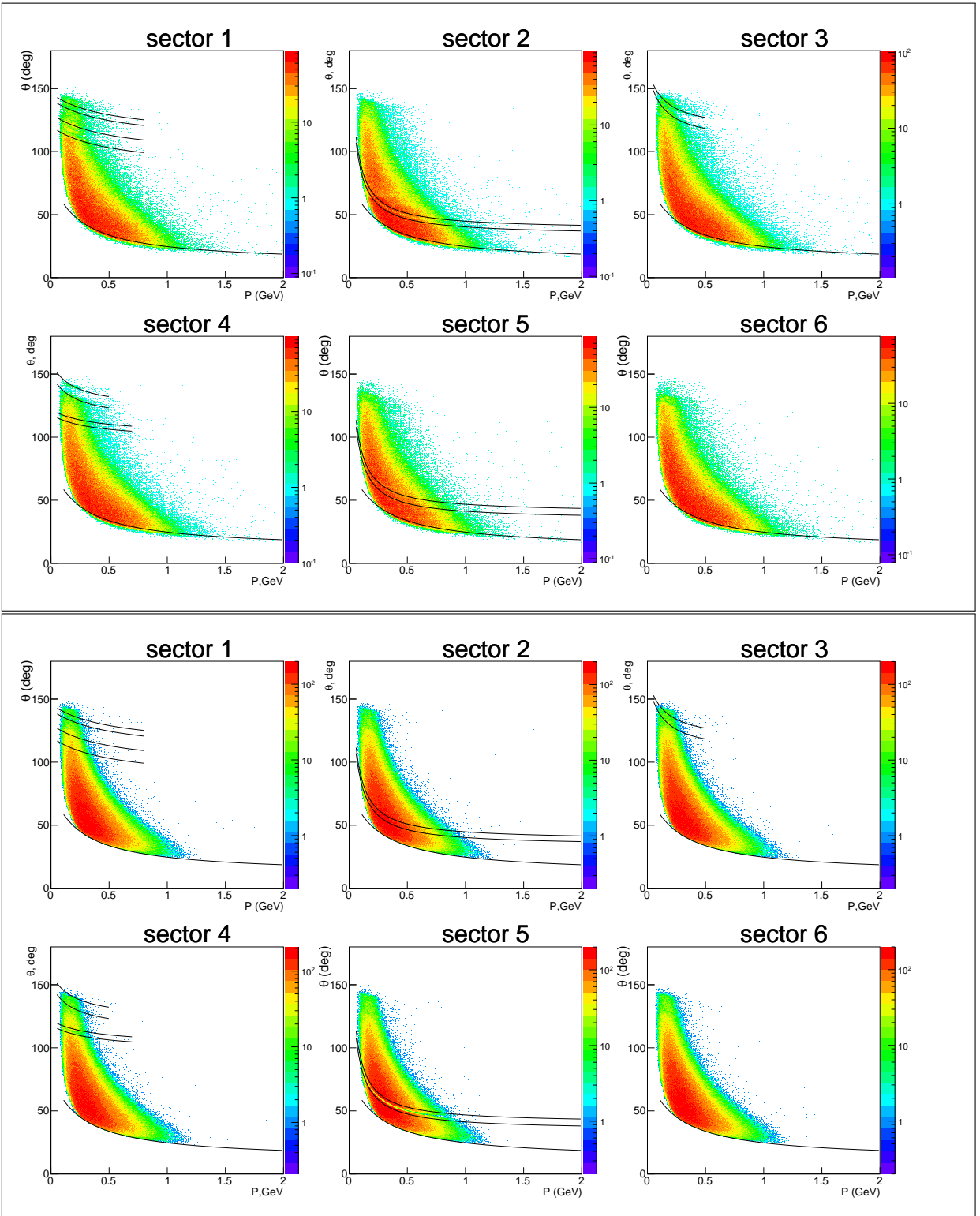


Figure 3.4: θ versus momentum distributions for real π^- events (upper frame) and for Monte Carlo events (lower frame) for all six CLAS sectors. Black curves show cuts applied to remove inefficient areas.

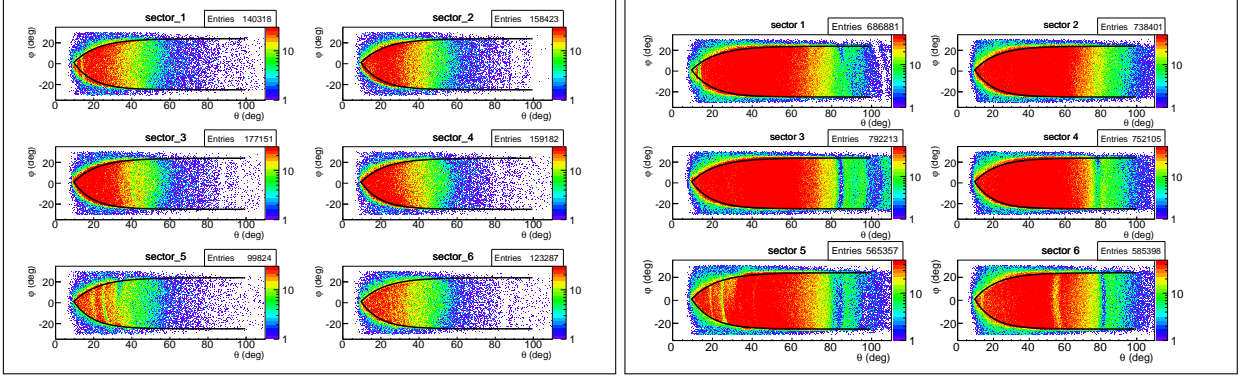


Figure 3.5: φ versus θ distributions for protons with momenta from 600 MeV to 800 MeV (left frame) and π^+ with momenta from 400 MeV to 600 MeV (right frame) for all six CLAS sectors. Curves show the applied fiducial cuts.

file are excluded from the analysis since FC readout is not synchronized with begin/end of the file.

DAQ live time is the portion of time within the *block* during which the DAQ is able to accumulate events. A significant deviation of the live time from the average value indicates event rate alteration. For instance, if the live time is close to one, then the event rate is too low and vice versa. In Fig. 3.8 DAQ live time and yields of elastic and inclusive events normalized to FC charge are shown as function of *block* number. *Blocks* between the horizontal red lines in Fig. 3.8 are selected for the analysis. Due to the enormous amount of *blocks* all of them can not be made visible in two dimensional histogram, so y-axis projections of histograms in Fig. 3.8 are produced (see Fig. 3.9). The horizontal red cut lines in Fig. 3.8 correspond to the vertical red cut lines in Fig. 3.9.

3.3 Vertex cut

The target is specific to the e1e experiment and its setup is presented in Fig. 3.10. It has a conical shape with diameter varying from 0.4 to 0.6 cm. In some instances cooling system could not extract all the heat generated by the beam and the hydrogen in the target cell could boil. If bubbles stay along the beamline, the real luminosity would be different from the expected value and the absolute measurement will lack accuracy. The conical shape helps to direct bubbles upwards and into a wider area of the target, thus clearing the beamline. The forward aluminum window is made exactly the same as the entry/exit windows of the target cell and can serve for both the estimation of the number of events originated in the target windows and to precisely measure target z position in the beamline.

In Fig. 3.11 distributions of electron coordinate z at the interaction vertex are shown for

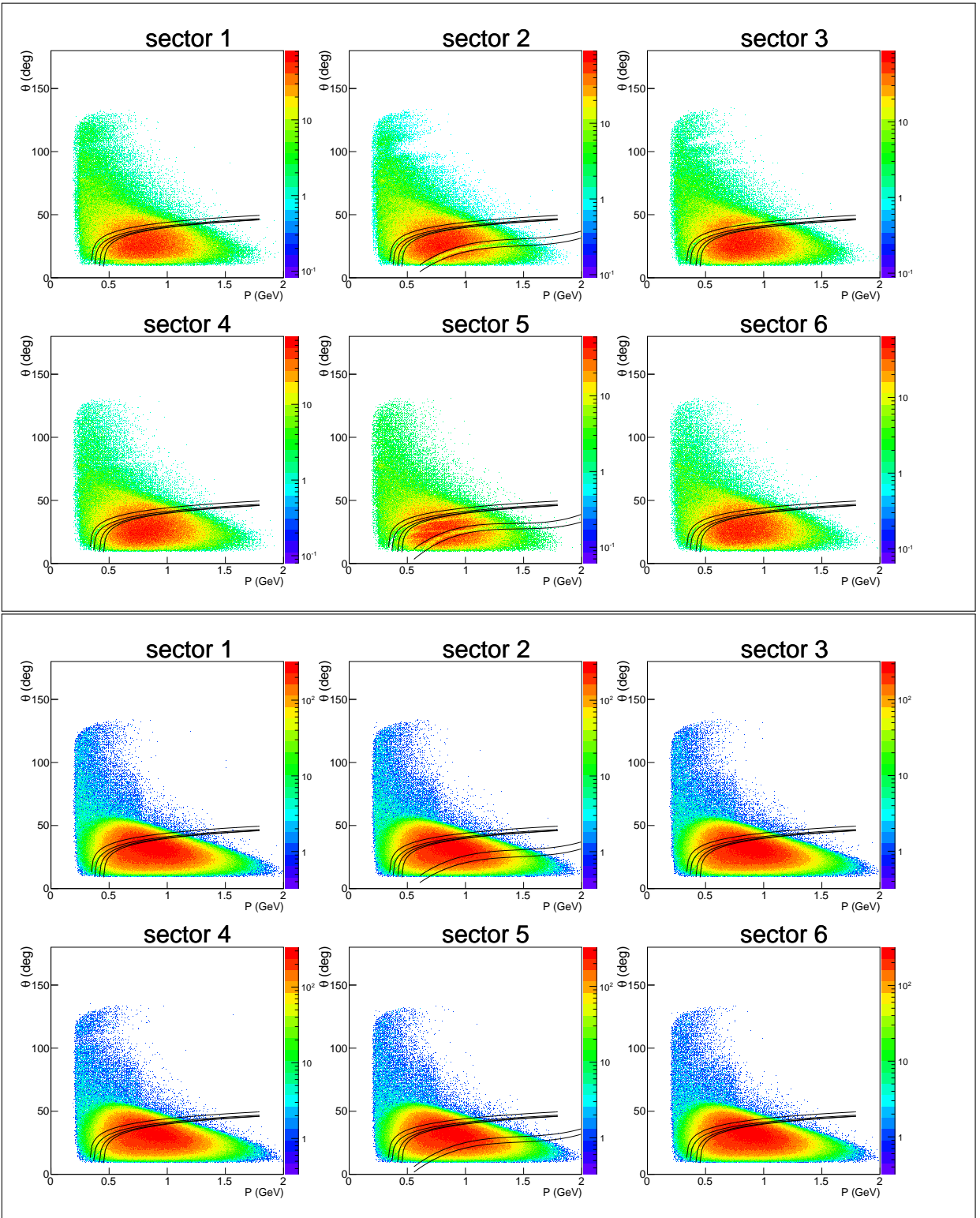


Figure 3.6: θ versus momentum distributions for real proton events (upper frame) and for Monte Carlo events (lower frame) for all six CLAS sectors. Black curves show cuts applied to remove inefficient areas.

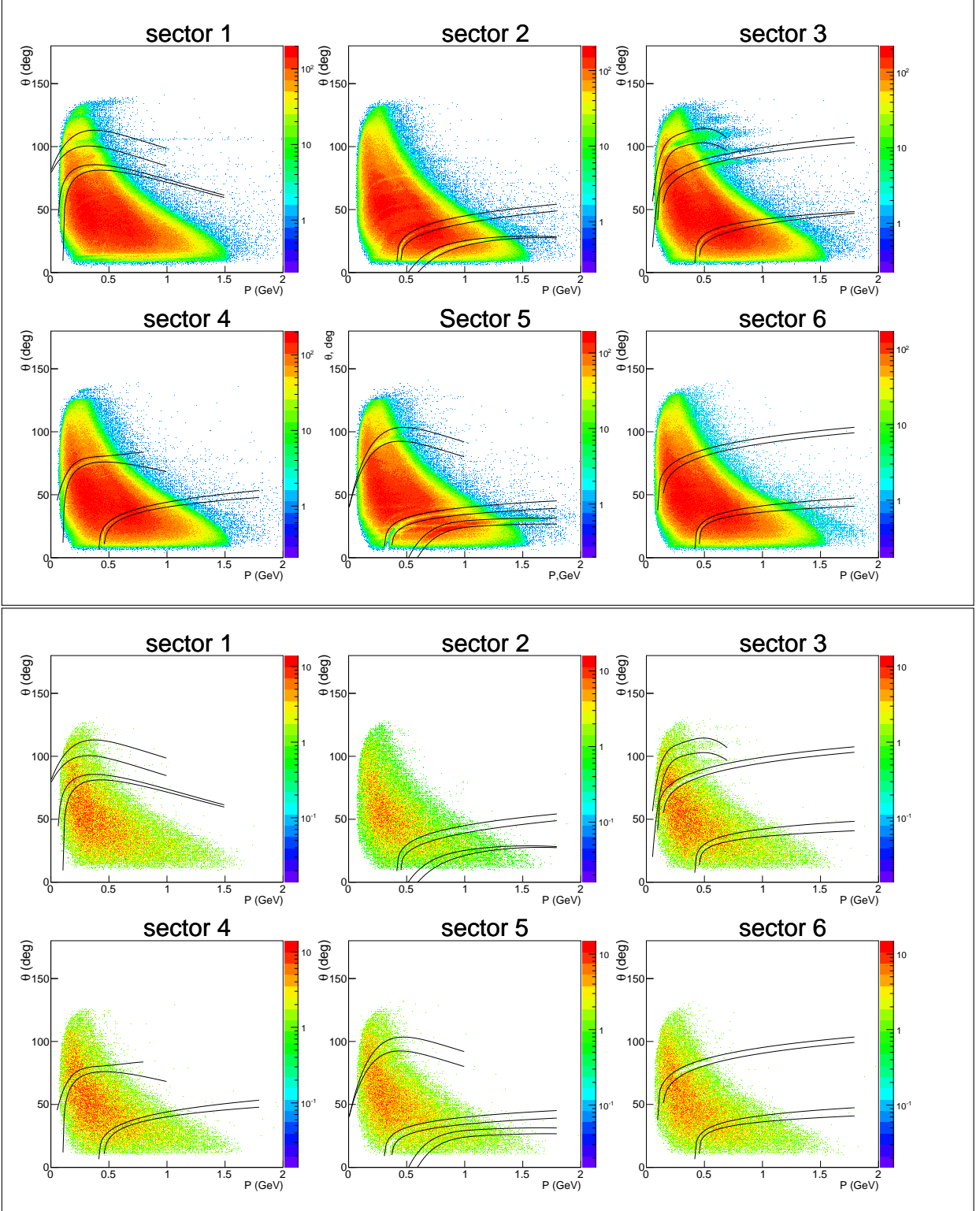


Figure 3.7: θ versus momentum distributions for real π^+ events (upper frame) and for Monte Carlo events (lower frame) for all six CLAS sectors. Black curves show cuts applied to remove inefficient areas.

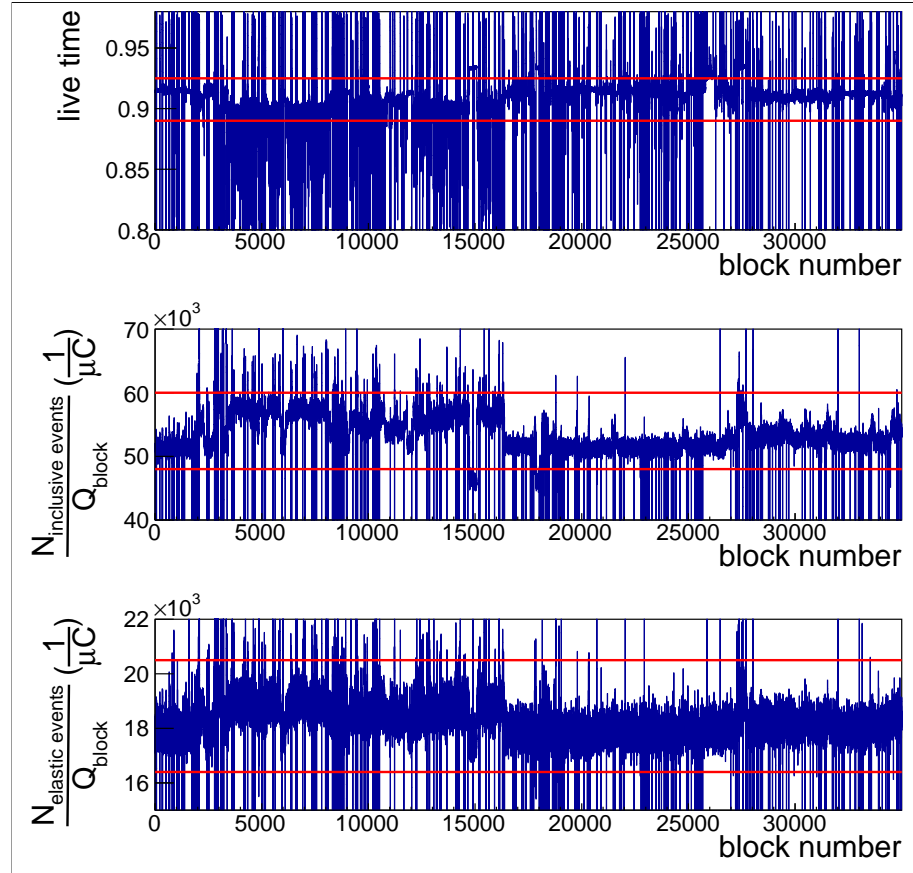


Figure 3.8: In the top plot DAQ live time is shown as function of *block* number. Each *block* corresponds to the portion of events that is accumulated during a single Faraday cup charge reading cycle. *Block* numbers range from one to the maximum number and represents the run duration in Faraday cup reading units. In the middle plot the number of inclusive events accumulated within each *block* divided by FC charge accumulated during the *block* is plotted versus *block* number. Bottom plot shows the number of elastic events accumulated within each *block* divided by FC charge accumulated during the *block* as function of *block* number. Horizontal red lines show the applied cuts.

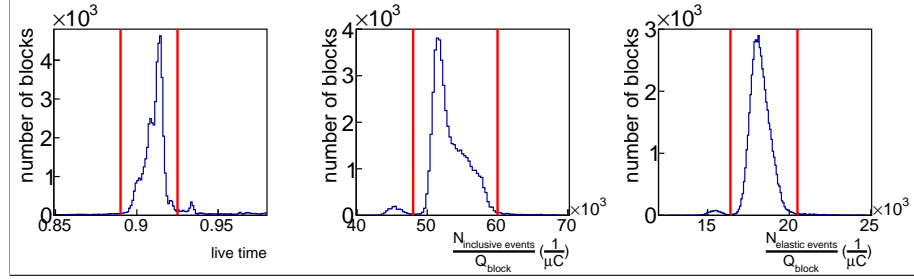


Figure 3.9: Number of *block* occurrences (see explanation in the text) as function of DAQ live time (left plot), inclusive event yield normalized to FC charge (middle plot), and elastic event yield normalized to FC charge (right plot).

477 events from both empty and full target runs for six CLAS sectors. The vertex coordinate z
 478 is taken from DCPB bank, where already beam-offset corrected values are stored. However
 479 small vertex corrections are made to shift the peak that corresponds to the forward aluminum
 480 window to the same position for full and empty target runs. Vertical green lines in Fig. 3.11
 481 show the cut that is applied in addition to the empty target event subtraction.

482 In Fig. 3.12 event distributions after subtraction of empty target contribution are shown
 483 in comparison with Monte Carlo events both reconstructed and generated. As it can be seen
 484 in Fig. 3.12 the simulation reproduces data well enough.

485 To reduce the number of events in which the electron comes from one and any hadron
 486 from another event, additional cuts on the difference of z coordinates of particles at the
 487 vertex are applied. These cuts do not allow the registered particles to have z vertices farther
 488 apart than 4 cm.

489 3.4 Exclusivity cut

490 Due to the experimental conditions the statistics of the double-pion events with all final
 491 hadrons registered is rather limited. Moreover, registration of all final hadrons leads to a
 492 limited acceptance, so the missing mass technique, when one of the final hadrons is not
 493 registered, is the best choice for the double-pion cross section extraction.

494 For the analyzed reaction one can distinguish four topologies:

- 495 • $ep \rightarrow e' p' \pi^+ X$
- 496 • $ep \rightarrow e' p' \pi^- X$
- 497 • $ep \rightarrow e' \pi^+ \pi^- X$
- 498 • $ep \rightarrow e' p \pi^+ \pi^- X$

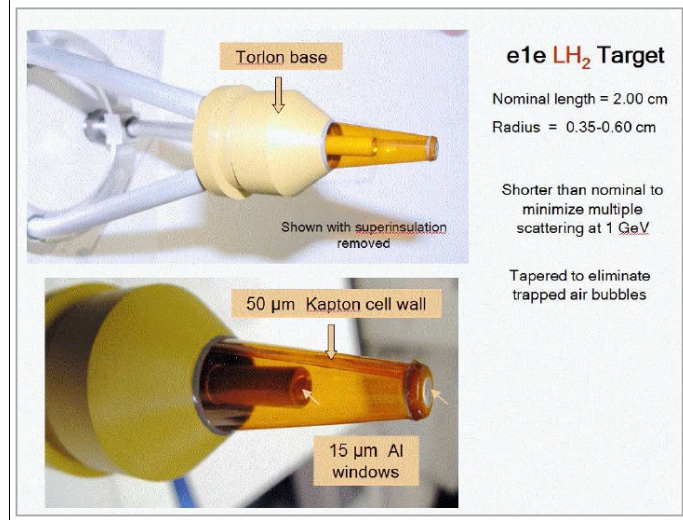


Figure 3.10: The target cell and support structure used during e1e run period.

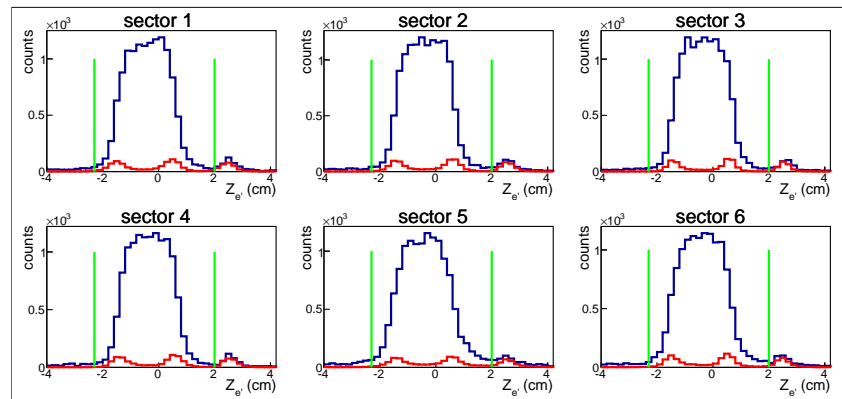


Figure 3.11: Distributions of the electron z coordinate at the vertex for full (blue curves) and empty (red curves) target runs for six CLAS sectors. Vertical green lines show the applied cuts. Both full and empty target distributions are normalized to the corresponding FC charge.

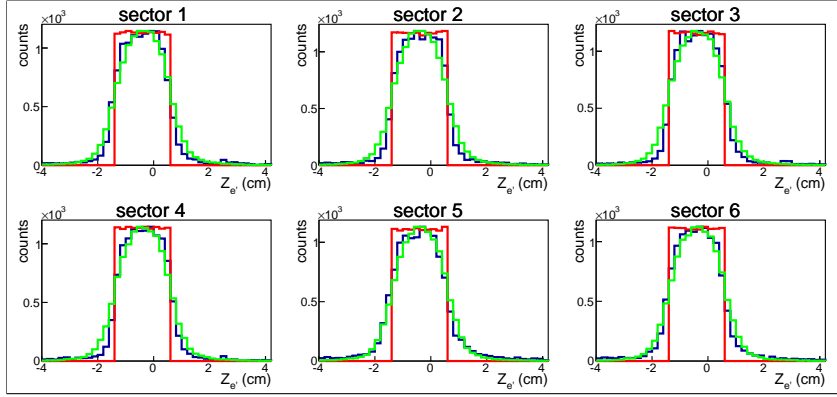


Figure 3.12: Distributions of the electron z coordinate at the vertex for data (blue curves) and Monte Carlo (green curves - reconstructed, red - generated) events for six CLAS sectors. For data empty target contributions are subtracted. All distributions are normalized to the maximum.

These topologies are defined in a way they do not overlap. For example the topology $ep \rightarrow e'p'\pi^+X$ requires the presence of e' , p' and π^+ candidates and absence of π^- candidates, avoiding in this way double counting.

For the case when one of the final hadrons is not registered, the missing mass M_X for the reaction $ep \rightarrow e'h_1h_2X$ is determined by

$$M_X^2 = (P_e + P_p - P_{e'} - P_{h_1} - P_{h_2})^2, \quad (3.4.1)$$

where P_{h_1} and P_{h_2} are the four-momenta of the registered final hadrons, P_e and P_p - four-momenta of initial electron and proton, and $P_{e'}$ - four-momentum of the scattered electron.

While for the events with all final hadrons registered, the missing mass M_X for the reaction $ep \rightarrow e'p'\pi^+\pi^-X$ is given by

$$M_X^2 = (P_e + P_p - P_{e'} - P_{\pi^+} - P_{\pi^-} - P_{p'})^2, \quad (3.4.2)$$

where P_e , P_p , $P_{e'}$, P_{π^+} , P_{π^-} , and $P_{p'}$ are the four-momenta of the initial and final particles.

Distributions of the missing mass squared for various topologies are shown in Fig. 3.13 for different W bins in comparison with Monte Carlo. The top row in Fig. 3.13 stands for the π^- -missing topology, the second row - for π^+ -missing topology, the third row - for proton-missing topology, and the bottom row for the case when all final hadrons are registered. The green arrows show the applied cuts. The π^- -missing topology contributes the biggest part to the statistics (about 70%), while events from other topologies populate kinematical areas with no acceptance for the π^- -missing topology. By combining events from various topologies one can reduce contributions from kinematical cells with zero acceptance (so-called empty cells) (see Sect. 4.5).

518 The simulation is carried out with the JM05 version of double-pion production model
 519 [28–30] and includes inclusive radiative effects according to [31]. More details about Monte
 520 Carlo simulation are in Sect. 4.4.

521 The contribution from the other exclusive channels (exclusive background) to the events
 522 within the exclusivity cuts is also taken into account by the Monte Carlo simulation. Most
 523 of the exclusive background events come from the $ep \rightarrow e'p'\pi^+\pi^-\pi^0$ channel. Both double-
 524 pion and three-pion channels are generated together with the relative weight of their cross
 525 sections taken from [32]. A phase space distribution is assumed for the 3π events. The 3π
 526 background can be barely seen as a separate peak on the right side of the missing mass
 527 squared distributions for the exclusive topology in last two W bins (see Fig. 3.13 bottom row). For the other topologies the 3π background can not be seen as a separate peak and
 528 it manifests itself as a contribution to the tail on the right side of the missing mass squared
 529 distributions.
 530

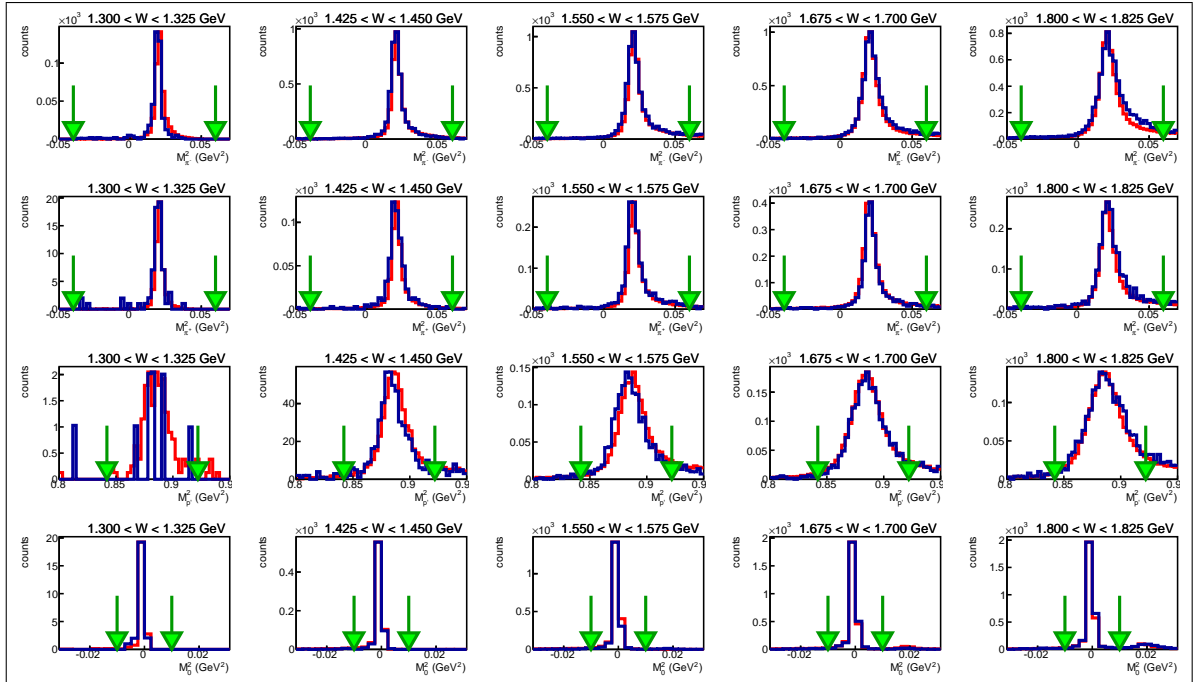
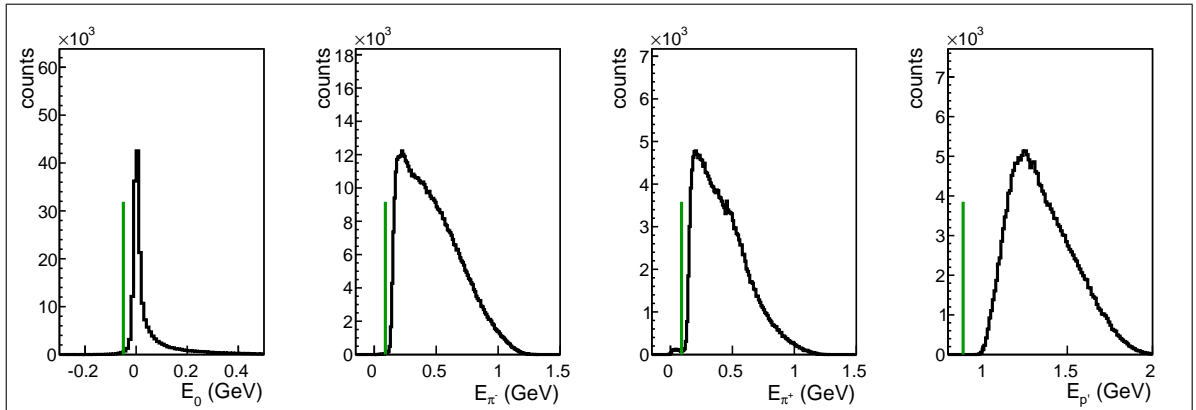


Figure 3.13: Missing mass squared distributions for various bins in W for Q^2 from 0.45 GeV^2 to 0.5 GeV^2 . Blue curves show real and red curves Monte Carlo events. The top row corresponds to π^- -missing topology, the second to π^+ -missing topology, the third to proton-missing topology, and the bottom to the fully exclusive topology. Green arrows show the applied exclusivity cuts.

531 3.5 Missing energy cut

532 To clean up event samples from misidentified and out-of-time particles, a cut on the missing
 533 energy is used in addition to the missing mass cut (Sect. 3.4). It limits the missing energy to
 534 be greater than $m_{miss.hadron} - 50$ MeV, where $m_{miss.hadron}$ is equal to the mass of the missing
 535 hadron (π^- , π^+ , or proton depending on the topology) or zero for the topology where all
 536 final hadrons are registered. The position of this cut is shown by the green vertical lines in
 Fig. 3.14.



537 Figure 3.14: Missing energy distributions for various topologies. Left plot corresponds to the topology where all final hadrons are registered and other plots correspond to the topologies with missing π^- , π^+ , or proton, respectively. Green vertical lines show the applied cut. All events on the right side of the lines are selected as good for analysis.

537

538 3.6 Binning and kinematical coverage

539 After all described above cuts and corrections about 2.5 million double-pion events survive
 540 and are used for the cross section calculation. Figure 3.15 shows the available kinematical
 541 coverage in electron variables. double-pion cross sections are calculated in 2D cells within
 542 the white boundaries in Fig. 3.15.

543 The binning in the final hadron variables is chosen according to the statistics left after
 544 the event selection (see Tab. 3.1) and takes into account the fact that the cross section is
 545 small in the W area near the double-pion production threshold. A more detailed description
 546 of the final hadron variable choice is given in Sect. 4.1.

547 It also needs to be mentioned that the right boundary of the invariant mass distributions

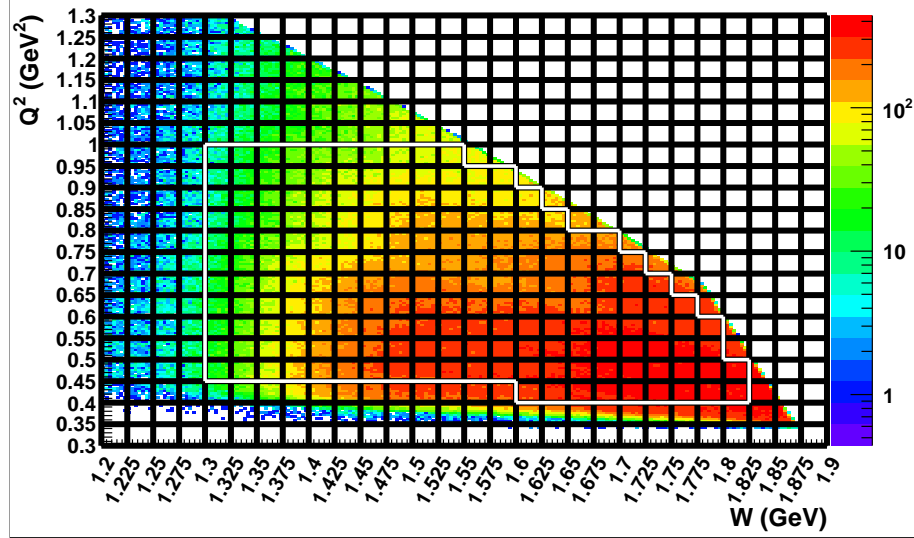


Figure 3.15: Q^2 versus W distribution populated with selected double-pion events. The cross section is calculated in 2D cells within the white boundaries.

548 depends on the value of W , while the left does not (see Eq. 3.6.1).

$$\begin{aligned} M_{left} &= m_{h_1} + m_{h_2} \\ M_{right} &= W - m_{h_3}, \end{aligned} \quad (3.6.1)$$

549 where M_{left} and M_{right} are the left and right boundaries of the invariant mass distribution.
550 m_{h_1} , m_{h_2} , and m_{h_3} are the masses of final hadrons. The value of W is taken in the center of
551 the corresponding W bin.

552 It leads to the fact that invariant mass distributions are broader at high W and hence a
553 more detailed binning in that area is necessary (see Tab. 3.1).

554 Since M_{right} is calculated using the value of W in the center of the corresponding W
555 bin some events are located beyond the boundaries determined by Eq. 3.6.1. Therefore the
556 binning in invariant mass needs special attention. Firstly the bin width is determined as:

$$width = \frac{M_{right} - M_{left}}{N_{bins} - 1}, \quad (3.6.2)$$

557 where N_{bins} is the number of bins.

558 Then the invariant mass distributions are obtained with the number of bins N_{bins} and
559 the left boundary of the first bin is set to M_{left} . That makes the last bin to be situated
560 completely out of the boundaries given by Eq. 3.6.1. Although the cross section obtained
561 in this bin is very small, it is kept in analysis since its content contributes to all other cross
562 sections obtained by integration over the corresponding invariant mass. After the binning

563 corrections this effect is assumed to be taken into account and this last bin in invariant
 564 masses is neglected.

565 It needs to be mentioned that the next to last bin in each invariant mass also needs
 566 special attention. Since the cross sections are obtained in W bin, the right boundaries
 567 of the invariant mass distributions vary for different events within this bin. In Fig. 3.16
 568 the distribution of the invariant mass of the two final hadrons X_1 and X_2 is schematically
 569 illustrated for the bin in W from W_{left} to W_{right} . The green and red vertical dashed lines
 570 show maximal invariant mass values that can be reached with W_{left} and W_{right} , respectively,
 571 while the vertical black dashed lines show the boundaries of the next to last bin in the
 572 invariant mass. As it is seen in Fig. 3.16 events in this bin with W between W_{left} and
 573 $M_{right}^{N_{bins}-1} = W_{center} - m_{X_3}$ are distributed in the range in $M_{X_1 X_2}$, which is less than invariant
 574 mass bin width defined by Eq. 3.6.2.

575 Correction for this effect is made using the new double pion event generator [33]. For
 576 that purpose for each invariant mass two one-dimensional distributions are generated in each
 577 W bin. The first one mimics the data distribution, for which all events in the next to last
 578 bin are divided by the same bin width defined by Eq. 3.6.2. For the second one events with
 579 W between W_{center} and W_{right} are divided by the same bin width defined by Eq. 3.6.2, while
 580 events with W between W_{left} and W_{center} are divided by the bin width that is individual
 581 for each event and equal to $W - m_{X_3} - M_{left}^{N_{bins}-1}$. The correction factor, by which obtained
 582 single-differential cross sections in the next to last bin should be multiplied, is defined as the
 583 ratio of the second distribution over the first one. This factor typically varies from 5% to
 584 10%.

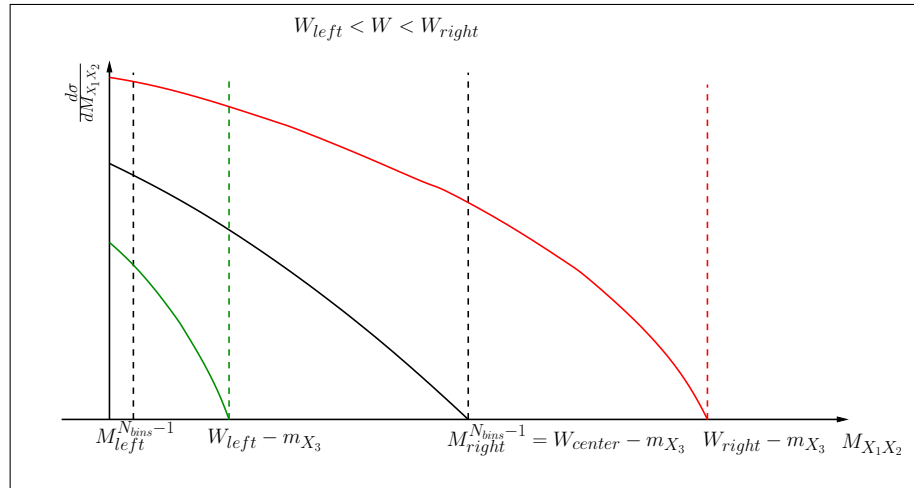


Figure 3.16: Schematic representation of the cross sections in the next to last bin in the invariant mass ($M_{X_1 X_2}$) for various W . Green and red vertical dashed lines show maximal invariant mass values that can be reached with W_{left} and W_{right} , respectively, while vertical black dashed lines show the boundaries of the next to last bin in the invariant mass.

Variable W range	Number of bins in invariant mass M	Number of bins in polar angle θ	Number of bins in azimuthal angle φ	Number of bins in angle between two planes α
1.3 - 1.35 GeV	8	6	5	5
1.35 - 1.4 GeV	10	8	5	6
1.4 - 1.45 GeV	12	10	5	8
> 1.45 GeV	12	10	8	8

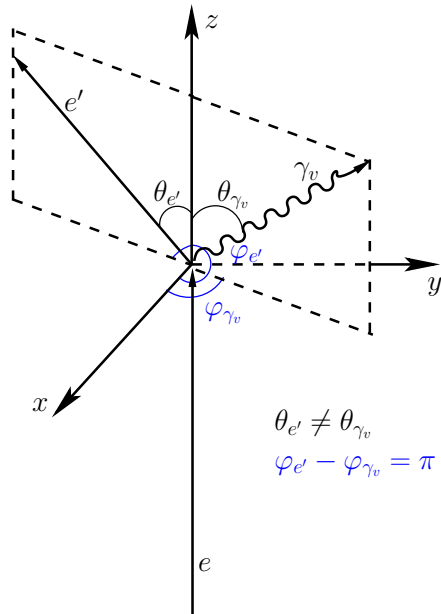
Table 3.1: Number of bins for the given final hadron variables.

⁵⁸⁵ Chapter 4

⁵⁸⁶ Cross section calculation

⁵⁸⁷ 4.1 Kinematical variables

⁵⁸⁸ After the double-pion event selection that uses the missing mass technique, the four-momenta
⁵⁸⁹ of all particles are known and can be used for the calculation of all kinematic variables. The
⁵⁹⁰ cross sections are obtained in the single-photon exchange approximation in the center of
⁵⁹¹ mass frame of the *virtual photon – initial proton* system.



$$\theta_{e'} \neq \theta_{\gamma_v}$$
$$\varphi_{e'} - \varphi_{\gamma_v} = \pi$$

Figure 4.1: Virtual photon and scattered electron angles θ and φ in the lab frame.

592 Therefore, to calculate the kinematic variables the four-momenta of all particles need to
 593 be transformed from the lab frame to the c.m. frame. For that purpose Lorentz transforma-
 594 tions that include the following steps are used ¹.

595 1) Firstly (xy)-plane of the lab system is rotated around z -axis to make x -axis laying in
 596 the electron scattering plane (see Fig. 4.1). This rotation transforms the four-momentum as
 597 $P' = P * R_1$, with

$$R_1 = \begin{pmatrix} \cos(\varphi_{e'}) & -\sin(\varphi_{e'}) & 0 & 0 \\ \sin(\varphi_{e'}) & \cos(\varphi_{e'}) & 0 & 0 \\ 0 & 0 & 1 & 0 \\ 0 & 0 & 0 & 1 \end{pmatrix}, \quad (4.1.1)$$

598 where $\varphi_{e'}$ is the azimuthal angle of the scattered electron.

599 After this rotation $\varphi_{\gamma_v} = \pi$, since the φ angle between scattered electron and virtual
 600 photon is equal to π ; and after the rotation $\varphi_{e'} = 0$ with respect to the intermediate reference
 601 frame.

602 2) After that the lab system is rotated to align the z -axis with the virtual photon direction.
 603 The four-momentum transformation for this rotation is given by $P'' = P' * R_2$, with

$$R_2 = \begin{pmatrix} \cos(\theta_{\gamma_v}) & 0 & -\sin(\theta_{\gamma_v}) & 0 \\ 0 & 1 & 0 & 0 \\ \sin(\theta_{\gamma_v}) & 0 & \cos(\theta_{\gamma_v}) & 0 \\ 0 & 0 & 0 & 1 \end{pmatrix}, \quad (4.1.2)$$

604 where θ_{γ_v} is the polar angle of the virtual photon. ²

605 3) Finally a boost into the c.m. frame of the *virtual photon – initial proton* system is

¹In all derivations the energy is assumed to be the last component of the four-momentum and the four-momentum to be a row vector.

²Using embedded ROOT functions, both rotations can be coded using the unit vectors TVector3 $uz = P4_gamma.Vect().Unit()$ and TVector3 $ux = (P4_EL.Vect().Cross(P4_ELP.Vect())).Unit()$, where P4_gamma, P4_EL, and P4_ELP are the four-momenta of the virtual photon, initial and final electrons, respectively. The axis vector ux needs to be rotated according to $ux.Rotate(3.*M_PI/2,uz)$. Finally the rotation is defined as $rot.SetZAxis(uz,ux).Invert()$ and needs to be applied to the four-momentum (P4) of each particle: $P4.Transform(rot)$.

606 performed. It is given by the formula $P''' = P'' * R_3$, with

$$R_3 = \begin{pmatrix} 1 & 0 & 0 & 0 \\ 0 & 1 & 0 & 0 \\ 0 & 0 & \gamma & -\gamma\beta \\ 0 & 0 & -\gamma\beta & \gamma \end{pmatrix}, \quad \beta = \frac{|\vec{q}|}{E_\gamma + m_{proton}} = \frac{\sqrt{E_\gamma^2 + Q^2}}{E_\gamma + m_{proton}}, \quad \gamma = \frac{1}{\sqrt{1 - \beta^2}}, \quad (4.1.3)$$

607 where $|\vec{q}|$ is the magnitude of the three-vector of the virtual photon and β the magnitude
608 and z -component of the three-vector $\vec{\beta} = (0, 0, \beta)$.³

609 When the four-momenta of all particles in the c.m. frame are defined one can calculate
610 the kinematic variables that describe the final hadron state. The three-body final state is
611 unambiguously determined by five kinematic variables. Indeed, three final particles could be
612 described by $4 \times 3 = 12$ components of their four-momenta. All these particles are on mass
613 shell. So, it gives us three restrictions $E_i^2 - P_i^2 = m_i^2$ ($i = 1, 2, 3$). The energy-momentum
614 conservation imposes four additional constraints for the final particles four-momenta com-
615 ponents. So, eventually five kinematic variables remain, which determine unambiguously
616 the three-body final state kinematics. In the electron scattering process $ep \rightarrow e'p'\pi^+\pi^-$ the
617 variables W, Q^2 are also present besides the hadronic final state variables. So electron scat-
618 tering cross section for double-charged pion electroproduction should be seven-differential:
619 five variables for the final hadrons plus W and Q^2 that are determined by the scattered elec-
620 tron kinematics. Such seven-differential cross sections may be written as $\frac{d^7\sigma}{dWdQ^2d^5\tau}$, where
621 $d^5\tau$ is five-dimensional phase space differential.

622 Several sets of five variables for the description of the final hadron kinematics may be
623 used. The following generalized set of variables is used in this analysis:

- 624 • invariant mass of the first pair of the particles M_{12} ;
- 625 • invariant mass of the second pair of the particles M_{23} ;
- 626 • the first particle solid angle Ω ;
- 627 • the angle α between two planes: one of them (plane A) is defined by the three-momenta
628 of the virtual photon (or initial proton) and the first final hadron, the second plane
629 (plane B) is defined by the three-momenta of all final hadrons (these angles are shown
630 in Figs. 4.3, 4.4, 4.5 for various choices of the first particle).

631 The cross sections in this analysis are obtained in three sets of variables depending on
632 various assignments for the first, second, and third final hadrons:

³ Note: if you use ROOT function `.Boost` you should change the sign of the z -component of β -vector:
`.Boost(0,0,-\beta)`.

- invariant mass of the $p'\pi^+$ pair, invariant mass of the $\pi^+\pi^-$ pair, proton spherical angles $\theta_{p'}$ and $\varphi_{p'}$ and angle $\alpha_{(p,p')(\pi^+,\pi^-)}$ (or $\alpha_{p'}$) between planes B (defined by the momenta of all final hadrons) and A (defined by initial and final protons), see Fig. 4.3;
- invariant mass of the $\pi^-\pi^+$ pair, invariant mass of the π^+p pair, π^- spherical angles θ_{π^-} and φ_{π^-} and angle $\alpha_{(p\pi^-)(p'\pi^+)}$ (or α_{π^-}) between planes B (defined by the momenta of all final hadrons) and A (defined by initial proton and π^-), see Fig. 4.4;
- invariant mass of the $\pi^+\pi^-$ pair, invariant mass of the π^-p pair, π^+ spherical angles θ_{π^+} and φ_{π^+} and angle $\alpha_{(p\pi^+)(p'\pi^-)}$ (or α_{π^+}) between planes B (defined by the momenta of all final hadrons) and A (defined by initial proton and π^+), see Fig. 4.5.

Lets explain in more detail the calculation of the kinematical variables in case of set number two. The invariant masses $M_{\pi^+\pi^-}$ and $M_{\pi^+p'}$ are calculated from the four-momenta of the final particles P_{π^-} , P_{π^+} , $P_{p'}$ in the c.m. frame in the following way

$$\begin{aligned} M_{\pi^+\pi^-} &= \sqrt{(P_{\pi^+} + P_{\pi^-})^2} \text{ and} \\ M_{\pi^+p'} &= \sqrt{(P_{\pi^+} + P_{p'})^2}. \end{aligned} \quad (4.1.4)$$

The angle θ_{π^-} between the three-momentum of the initial photon (\vec{P}_γ) and three-momentum of the final π^- (\vec{P}_{π^-}) in c.m. frame is calculated as:

$$\theta_{\pi^-} = \arccos \left(\frac{(\vec{P}_{\pi^-} \cdot \vec{P}_\gamma)}{|\vec{P}_{\pi^-}| |\vec{P}_\gamma|} \right) \quad (4.1.5)$$

The angle φ_{π^-} is determined as:

$$\begin{aligned} \varphi_{\pi^-} &= \arctg \left(\frac{P_{y\pi^-}}{P_{x\pi^-}} \right); P_{x\pi^-} > 0; P_{y\pi^-} > 0 \\ \varphi_{\pi^-} &= \arctg \left(\frac{P_{y\pi^-}}{P_{x\pi^-}} \right) + 2\pi; P_{x\pi^-} > 0; P_{y\pi^-} < 0 \\ \varphi_{\pi^-} &= \arctg \left(\frac{P_{y\pi^-}}{P_{x\pi^-}} \right) + \pi; P_{x\pi^-} < 0; P_{y\pi^-} < 0 \\ \varphi_{\pi^-} &= \arctg \left(\frac{P_{y\pi^-}}{P_{x\pi^-}} \right) + \pi; P_{x\pi^-} < 0; P_{y\pi^-} > 0 \\ \varphi_{\pi^-} &= \pi/2; P_{x\pi^-} = 0; P_{y\pi^-} > 0 \\ \varphi_{\pi^-} &= 3\pi/2; P_{x\pi^-} = 0; P_{y\pi^-} < 0, \end{aligned} \quad (4.1.6)$$

where $P_{i\pi^-}$ is i -component of the π^- three-momentum ($i = x, y, z$). The angles θ_{π^-} and φ_{π^-} are shown in Fig. 4.2.

650 The calculation of the angle α_{π^-} between two planes A and B (see Fig. 4.4) is more
 651 complicated. Firstly two auxiliary vectors $\vec{\gamma}$ and $\vec{\beta}$ should be determined. The vector $\vec{\gamma}$ is
 652 the unit vector perpendicular to the three-momentum \vec{P}_{π^-} , directed toward the vector $(-\vec{n}_z)$
 653 and situated in the plane A, which is defined by the three-momentum of initial proton and
 654 three-momentum of π^- . \vec{n}_z is the unit vector directed along z -axis. The vector $\vec{\beta}$ is the unit
 655 vector perpendicular to the three-momentum of π^- , directed toward the three-momentum
 656 of π^+ and situated in the plane B, which is defined by all final hadrons. Note that the three-
 657 momenta of π^+ , π^- , p' are in the same plane, since in c.m. frame their total three-momentum
 658 has to be equal to zero. Then the angle between two planes α_{π^-} is

$$\alpha_{\pi^-} = \arccos(\vec{\gamma} \cdot \vec{\beta}), \quad (4.1.7)$$

659 where \arccos is a function that runs between zero and π , while the angle α_{π^-} may vary between
 660 zero and 2π . To determine the α angle in the range between π and 2π the relative direction
 661 between the π^- three-momentum and the vector product $\vec{\delta} = [\vec{\gamma} \times \vec{\beta}]$ of the auxiliary vectors
 662 $\vec{\gamma}$ and $\vec{\beta}$ should be taken into account. If the vector $\vec{\delta}$ is colinear to the three-momentum of
 663 π^- , the angle α_{π^-} is determined by (4.1.7), and in a case of anti-collinearity by

$$\alpha_{\pi^-} = 2\pi - \arccos(\vec{\gamma} \cdot \vec{\beta}). \quad (4.1.8)$$

664 The defined above vector $\vec{\gamma}$ can be expressed as

$$\begin{aligned} \vec{\gamma} &= a_\alpha(-\vec{n}_z) + b_\alpha \vec{n}_{P_{\pi^-}} \quad \text{with} \\ a_\alpha &= \sqrt{\frac{1}{1 - (\vec{n}_{P_{\pi^-}} \cdot (-\vec{n}_z))^2}} \quad \text{and} \\ b_\alpha &= -(\vec{n}_{P_{\pi^-}} \cdot (-\vec{n}_z))a_\alpha, \end{aligned} \quad (4.1.9)$$

665 where $\vec{n}_{P_{\pi^-}}$ is the unit vector directed along the three-momentum of π^- (see Fig. 4.4).
 666 Taking the scalar products $(\vec{\gamma} \cdot \vec{n}_{P_{\pi^-}})$ and $(\vec{\gamma} \cdot \vec{\gamma})$, it is straightforward to verify, that $\vec{\gamma}$ is
 667 the unit vector perpendicular to the three-momentum of π^- .

668 The vector $\vec{\beta}$ can be obtained as

$$\begin{aligned} \vec{\beta} &= a_\beta \vec{n}_{P_{\pi^+}} + b_\beta \vec{n}_{P_{\pi^-}} \quad \text{with} \\ a_\beta &= \sqrt{\frac{1}{1 - (\vec{n}_{P_{\pi^+}} \cdot \vec{n}_{P_{\pi^-}})^2}} \quad \text{and} \\ b_\beta &= -(\vec{n}_{P_{\pi^+}} \cdot \vec{n}_{P_{\pi^-}})a_\beta, \end{aligned} \quad (4.1.10)$$

669 where $\vec{n}_{P_{\pi^+}}$ is the unit vector directed along the three-momentum of π^+ .

670 Again taking the scalar products $(\vec{\beta} \cdot \vec{n}_{P_{\pi^-}})$ and $(\vec{\beta} \cdot \vec{\beta})$, it is straightforward to see, that
 671 $\vec{\beta}$ is the unit vector perpendicular to the three-momentum of π^- .

672 The angle α_{π^-} coincides with the angle between the vectors $\vec{\gamma}$ and $\vec{\beta}$. So, the scalar
 673 product $(\vec{\gamma} \cdot \vec{\beta})$ allows to determine the angle α_{π^-} (4.1.7). The kinematic variables for the
 674 other assignments for the first, second, and third final hadrons described above, are evaluated
 in the similar way.

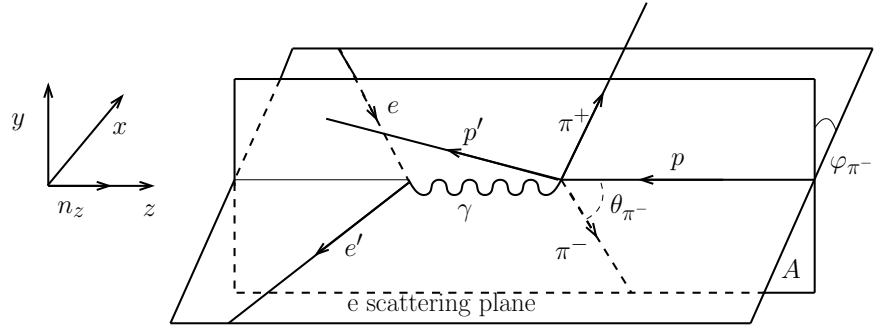


Figure 4.2: Polar (θ_{π^-}) and azimuthal (φ_{π^-}) angles of π^- in the c.m. frame.

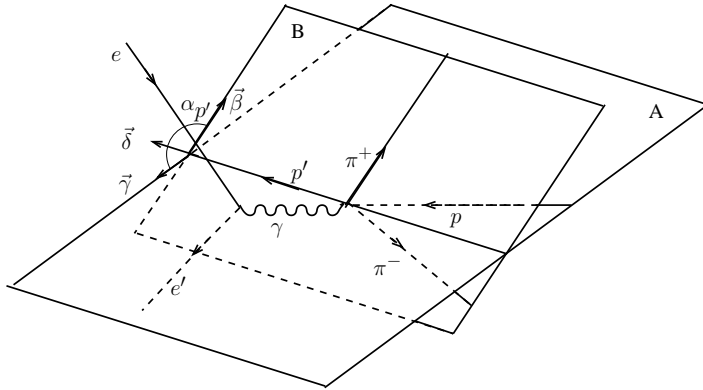


Figure 4.3: Definition of the angle $\alpha_{p'}$ between two planes: the plane B is defined by the three-momenta of all final hadrons, while the plane A defined by the three-momenta of initial and scattered protons. The definitions of auxiliary vectors $\vec{\beta}$, $\vec{\gamma}$, $\vec{\delta}$ are given in the text.

675
 676 Further detailed information about kinematic of the reactions with three-particle final
 677 states can be found here [34].

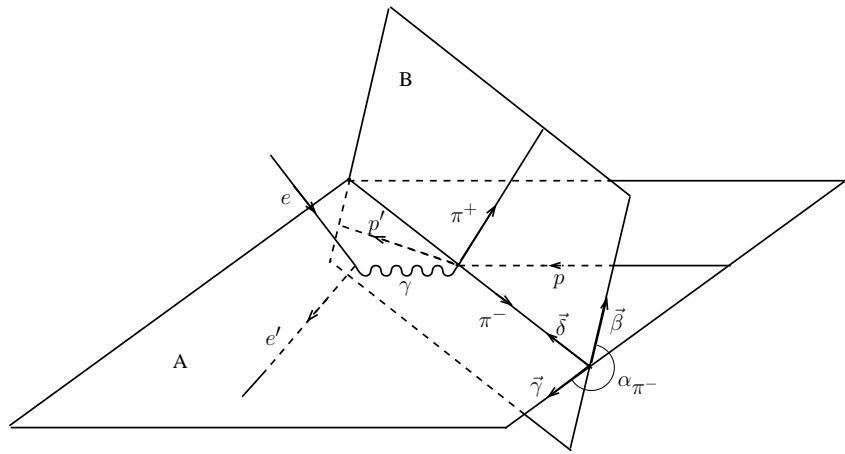


Figure 4.4: Definition of the angle α_{π^-} between two planes: the plane B is defined by the three-momenta of all final hadrons, while the plane A defined by the three-momenta of π^- and initial proton. The definitions of auxiliary vectors $\vec{\beta}$, $\vec{\gamma}$, $\vec{\delta}$ are given in the text.

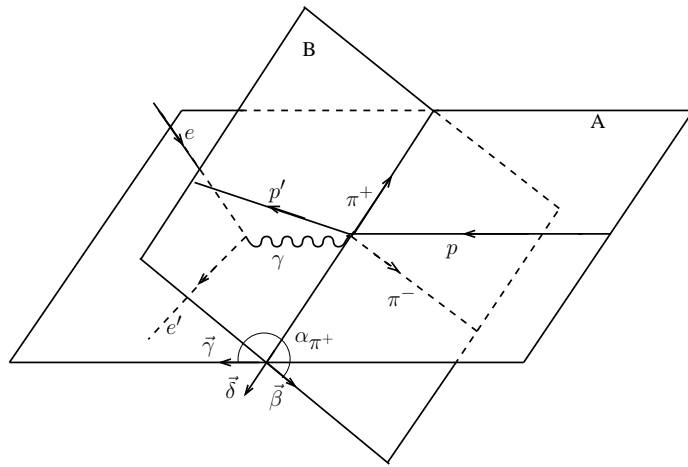


Figure 4.5: Definition of the angle α_{π^+} between two planes: the plane B is defined by the three-momenta of all final hadrons, while the plane A defined by the three-momenta of π^+ and initial proton. The definitions of auxiliary vectors $\vec{\beta}$, $\vec{\gamma}$, $\vec{\delta}$ are given in the text.

678 4.2 Cross section formula

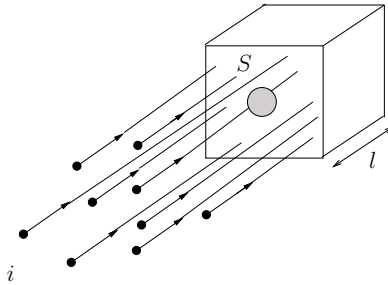


Figure 4.6: The incoming electron beam with the current i is hitting a homogeneous target with the area S and density ρ .

679 In the fixed target experiments (see Fig. 4.6) the interaction rate (the number of inter-
680 actions per second) can be determined according to the following relation:

$$\frac{dN}{dt} = \frac{i N_{targ} \sigma}{S}, \quad (4.2.1)$$

681 where i is the beam current (the number of incoming electrons per second), N_{targ} is the total
682 number of nuclei inside the target, S is the taget area, σ is the total cross section.

683 For i the following is true:

$$i = \frac{dN_{beam}}{dt} = \frac{1}{q_e} \frac{dQ}{dt}, \quad (4.2.2)$$

684 where N_{beam} is the number of incoming electrons, Q is the total charge that is carried by
685 incoming electrons, q_e is the elementary charge.

686 N_{targ} can be written in this way:

$$N_{targ} = \frac{m N_A}{M_m} = \frac{N_A \rho V}{M_m} = \frac{N_A \rho S l}{M_m}, \quad (4.2.3)$$

687 where m , V , ρ , l are the mass, volume, density and length of the target, respectively, M_m is
688 the molar mass of the target material, N_A is the Avogadro constant.

689 From (4.2.1), (4.2.2) and (4.2.3) the cross section

$$\sigma = \frac{q_e \Delta N M_m}{Q l N_A \rho} = \frac{\Delta N}{L}, \quad (4.2.4)$$

690 where $L = \frac{Q l N_A \rho}{q_e M_m}$ is the luminosity and Q is the total charge of incoming electrons accumu-
691 lated in the Faraday cup.

692 Since this analysis is focused on the reaction $ep \rightarrow e'p'\pi^+\pi^-$, the quantity ΔN in the
 693 formula (4.2.4) is the total number of double-pion events. Liquid hydrogen is located in the
 694 target cell, hence the number of events that correspond to the target cell walls needs to be
 695 subtracted from the number of events that corresponds to the full target.

696 Taking into account that the charge accumulated in the Faraday cup is different for full
 697 (Q_{full}) and empty (Q_{empty}) target runs the formula for the total cross section can be rewritten
 698 as

$$\sigma = \frac{\frac{\Delta N_{full}}{Q_{full}} - \frac{\Delta N_{empty}}{Q_{empty}}}{\frac{l\rho N_A}{q_e M_m}}. \quad (4.2.5)$$

699 As it is mentioned in Sect. 4.1 the double-pion cross section depends on seven kinematical
 700 variables. For the second set of kinematical variables (see Sect. 4.1) considering formula
 701 (4.2.5) the seven-differential cross section can be written as

$$\frac{d\sigma}{dW dQ^2 dM_{p\pi^+} dM_{\pi^+\pi^-} d\Omega d\alpha_{\pi^-}} = \frac{1}{F \cdot R} \frac{\left(\frac{\Delta N_{full}}{Q_{full}} - \frac{\Delta N_{empty}}{Q_{empty}} \right)}{\Delta W \Delta Q^2 \Delta \tau \left(\frac{l\rho N_A}{q_e M_H} \right)}, \quad (4.2.6)$$

702 where ΔN_{full} and ΔN_{empty} are the numbers of events inside the seven-dimensional bin for
 703 runs with hydrogen and empty target, respectively. Each event is weighted with the cor-
 704 responding photoelectron correction factor given by Eq. 2.1.12. $F = F(\Delta W, \Delta Q^2, \Delta \tau)$ is the
 705 total efficiency coming from the Monte Carlo simulation, $R = R(\Delta W, \Delta Q^2)$ is the radiative
 706 correction factor, $Q_{full} = 5999.64 \mu\text{C}$ and $Q_{empty} = 334.603 \mu\text{C}$ are the integrated Faraday
 707 cup charges for runs with hydrogen and empty target, respectively. These charges are calcu-
 708 lated by summing up charges of all corresponding *blocks* that are used in the analysis. See
 709 the definition of *block* in Section 3.2. q_e is the elementary charge ($q_e = 1.610^{-19}\text{C}$), ρ is the
 710 density of liquid hydrogen ($\rho = 0.0708 \text{ g/cm}^3$) at $T = 20 \text{ K}$, l is the length of the target
 711 ($l = 2 \text{ cm}$), M_H is the molar density of the natural mixture of hydrogen ($M_H = 1.00794$
 712 g/mol), N_A is Avogadro's number ($N_A = 6.0210^{23} \text{ mol}^{-1}$), ΔW and ΔQ^2 are kinematical
 713 bins that are determined by the electron scattering kinematics, and $\Delta \tau$ is an element of the
 714 hadronic five-dimensional phase space

$$\Delta \tau = \Delta M_{p\pi^+} \Delta M_{\pi^+\pi^-} \Delta(-\cos(\theta_{\pi^-})) \Delta \varphi_{\pi^-} \Delta \alpha_{\pi^-}. \quad (4.2.7)$$

715 In the single photon exchange approximation, the electron scattering cross section is
 716 related to the hadronic cross section $\frac{d\sigma}{dM_{p\pi^+} dM_{\pi^+\pi^-} d\Omega_{\pi^-} d\alpha_{\pi^-}}$ by

$$\frac{d\sigma}{dM_{p\pi^+} dM_{\pi^+\pi^-} d\Omega_{\pi^-} d\alpha_{\pi^-}} = \frac{1}{\Gamma_v} \frac{d\sigma}{dW dQ^2 dM_{p\pi^+} dM_{\pi^+\pi^-} d\Omega_{\pi^-} d\alpha_{\pi^-}}, \quad (4.2.8)$$

717 where Γ_v is virtual photon flux, given by

$$\Gamma_v = \frac{\alpha}{4\pi} \frac{1}{E_{beam}^2 M_p^2} \frac{W(W^2 - M_p^2)}{(1 - \varepsilon)Q^2}, \quad (4.2.9)$$

718 where α is the fine structure constant ($1/137$), M_p is the proton mass, and ε is the virtual
 719 photon transverse polarization, given by

$$\varepsilon = \left(1 + 2 \left(1 + \frac{\omega^2}{Q^2} \right) \tan^2 \left(\frac{\theta_{e'}}{2} \right) \right)^{-1}, \quad (4.2.10)$$

720 where $\omega = E_{beam} - E_{scattered\ electron}$ and $\theta_{e'}$ is the angle of the scattered electron in the lab
 721 frame. W , Q^2 and $\theta_{e'}$ are taken in the center of the bin.

722 Limited statistics does not allow to estimate the five-differential cross section with rea-
 723 sonable accuracy. Therefore, the five-differential hadronic cross sections obtained in each
 724 bin in W and Q^2 are integrated in order to obtain the single-differential cross sections.

725 The following set of the single-differential cross sections are obtained for the second set
 726 of variables mentioned in Sect. 4.1:

$$\begin{aligned} \frac{d\sigma}{dM_{\pi^+\pi^-}} &= \int \frac{d^5\sigma}{d^5\tau} d\tau_{M_{\pi^+\pi^-}}^4; & d\tau_{M_{\pi^+\pi^-}}^4 &= dM_{\pi^+p} d\Omega_{\pi^-} d\alpha_{\pi^-} \\ \frac{d\sigma}{dM_{\pi^+p}} &= \int \frac{d^5\sigma}{d^5\tau} d\tau_{M_{\pi^+p}}^4; & d\tau_{M_{\pi^+p}}^4 &= dM_{\pi^+\pi^-} d\Omega_{\pi^-} d\alpha_{\pi^-} \\ \frac{d\sigma}{d(-\cos\theta_{\pi^-})} &= \int \frac{d^5\sigma}{d^5\tau} d\tau_{\theta_{\pi^-}}^4; & d\tau_{\theta_{\pi^-}}^4 &= dM_{\pi^+\pi^-} dM_{\pi^+p} d\varphi_{\pi^-} d\alpha_{\pi^-} \\ \frac{d\sigma}{d\alpha_{\pi^-}} &= \int \frac{d^5\sigma}{d^5\tau} d\tau_{\alpha_{\pi^-}}^4; & d\tau_{\alpha_{\pi^-}}^4 &= dM_{\pi^+\pi^-} dM_{\pi^+p} d\Omega_{\pi^-} \end{aligned} \quad (4.2.11)$$

with $d^5\tau = dM_{\pi^+\pi^-} dM_{\pi^+p} d\Omega_{\pi^-} d\alpha_{\pi^-}$.

727 For the two other sets of variables from Sect. 4.1 the single-differential cross sections can be
 728 obtained in a similar way.

729 In the actual cross section calculations the integrals in (4.2.11) are substituted by respec-
 730 tive sums over the five-dimensional kinematical grid of hadronic cross sections.

731 To evaluate the absolute statistical error of the five-differential hadronic cross sections
 732 the following error propagation approach is used:

$$\delta_{stat}(M_{p\pi^+}, M_{\pi^+\pi^-}, \theta_{\pi^-}, \varphi_{\pi^-}, \alpha_{\pi^-}) = \frac{1}{F \cdot R} \frac{1}{\Gamma_v} \frac{\sqrt{\left(\frac{\Delta N_{full}}{Q_{full}^2} + \frac{\Delta N_{empty}}{Q_{empty}^2} \right)}}{\Delta W \Delta Q^2 \Delta \tau \left(\frac{l\rho N_A}{q_e M_H} \right)}. \quad (4.2.12)$$

733 Another source of statistical fluctuations is connected to the limited statistics in the Monte
 734 Carlo simulation. From (4.2.6) it is clear that the uncertainty in the efficiency F is affecting

735 the cross section value. The definition of efficiency factor F is simple:

$$F = \frac{N_{rec}}{N_{gen}}, \quad (4.2.13)$$

736 where N_{gen} and N_{rec} are the numbers of Monte Carlo generated and reconstructed events,
737 respectively.

738 Due to the fact that N_{gen} and N_{rec} are not independent the special approach needs to
739 be applied in order to calculate the statistical error of efficiency. This approach is described
740 in [35] and neglecting the events migration between the bins it gives the following expression
741 for the absolute statistical error in F

$$\delta(F) = \sqrt{\frac{(N_{gen} - N_{rec})N_{rec}}{N_{gen}^3}}. \quad (4.2.14)$$

742 It needs to be mentioned that kinematical cells where $N_{rec} >= N_{gen}$ are treated as empty
743 cells with no efficiency. Such cells are very rare and usually located near the edges of the
744 invariant mass distributions where the cross section is close to zero.

745 The absolute error on the cross section due to the limited Monte Carlo statistic is given
746 by

$$\delta_{stat,MC} = \frac{d\sigma}{dM_{\pi^+\pi^-} dM_{\pi^+p} d\Omega_{\pi^-} d\alpha_{\pi^-}} \left(\frac{\delta(F)}{F} \right) \quad (4.2.15)$$

747 Finally two statistical errors that come from fluctuation in the data and from the Monte
748 Carlo are combined quadratically, so the total absolute statistical error is given by

$$\delta_{stat,tot} = \sqrt{\delta_{stat,MC}^2 + \delta_{stat}^2}. \quad (4.2.16)$$

749 4.3 Radiative corrections

750 The radiative corrections are done using the new double-pion event generator (see Iu. Sko-
751 rodumina wiki page [33] and Sect 4.4). For that purpose double-pion events are generated
752 with and without radiative effects. After that radiative correction factor R in formula (4.2.6)
753 is determined by

$$R = \frac{N_{rad}^{2D}}{N_{norad}^{2D}}, \quad (4.3.1)$$

754 where N_{rad}^{2D} and N_{norad}^{2D} are the numbers of generated events in each (W, Q^2) bin with and
755 without radiative effects, respectively. The quantity one over R is plotted on the left side of
756 Fig. 4.7 as a function of W for various Q^2 bins. As it can be seen in Fig. 4.7 the dependence
757 of the radiative correction factor on Q^2 is rather small. So, for the actual cross section
758 calculations the factor R is averaged over all Q^2 bins (see right side of Fig. 4.7). The

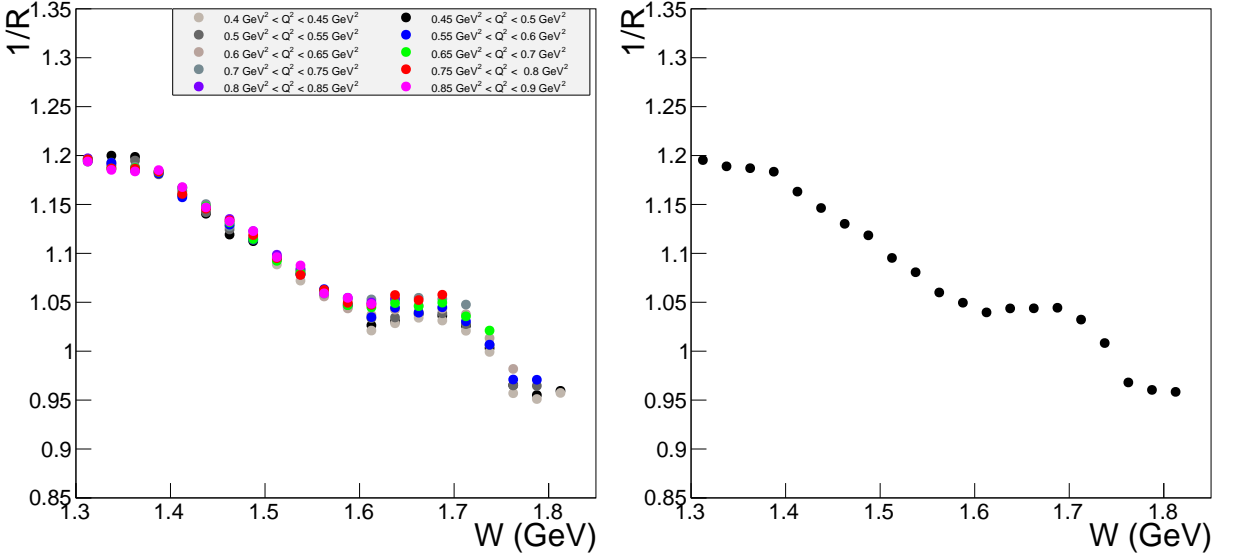


Figure 4.7: One over radiative correction factor (see formula 4.2.6) as function of W , for various bins over Q^2 (left plot) and averaged over all Q^2 bins (right plot).

759 statistical uncertainties associated with the number of generated events are also small and
 760 not seen in Fig. 4.7.

761 It should be noted that to account for radiative effects, the new double-pion event gen-
 762 erator uses the well known approach taken from Mo and Tsai [31]. In this approach the soft
 763 part is evaluated explicitly, while for the calculation of the hard part the "inclusive" hadronic
 764 tensor is used. The applicability of this approximation for the hard part of radiative effects
 765 is subject of special attention. The single-differential double-pion cross sections (4.2.11)
 766 obtained in this analysis represent the over four variables integrated five-differential cross
 767 sections. This integration considerably reduces the influence of the final hadron kinematics
 768 on the radiative correction factor. Therefore, the "inclusive" Mo and Tsai procedure is in
 769 the case of double-pion cross sections more applicable than in a case of non-integrated cross
 770 sections that are typically obtained for instance in the single-pion data analysis.

771 It also should be mentioned that this correction should be applied before the empty cells
 772 (see Sect. 4.5) are filled, since the cross sections that are used for the purpose of filling empty
 773 cells are already corrected for radiative effects.

774 4.4 Efficiency evaluation

775 For the efficiency calculation the Monte Carlo event generator of the Genova group is used.
 776 This event generator uses the JM05 model [36] for double-pion channel. Although the cross

sections on which the event generator is based do not include the latest modifications of the JM model [7–9], it describes the data well enough to use it for the purpose of the efficiency evaluation.

To take into account the multi-pion background, three-pion events are generated simultaneously with the double-pion ones, the relative weight of these two channels is determined according to their integral cross sections at the photon point, see Fig. 4.8. The event generator does not assume any model for the channel $ep \rightarrow e'p'\pi^+\pi^-\pi^0$, so for this channel phase space distributions are generated. It needs to be mentioned that even at high W (around 1.8 GeV) three-pion background contributes only few percent to the double-pion events that survive after the exclusivity cut (see Sect. 3.4).

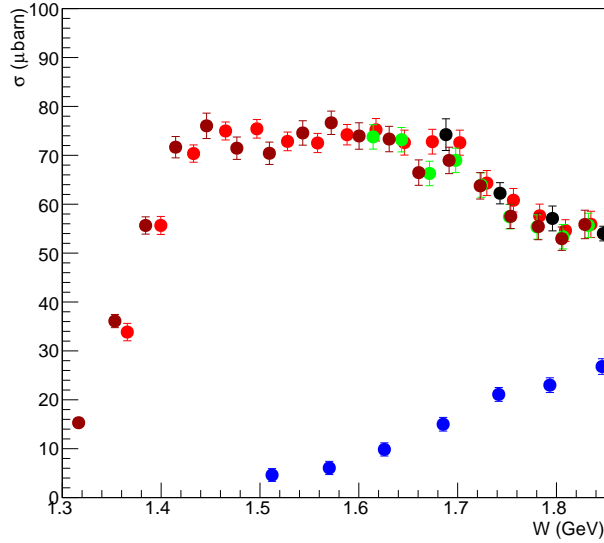


Figure 4.8: Integral cross sections of the reactions $ep \rightarrow e'p'\pi^+\pi^-$ and $ep \rightarrow e'p'\pi^+\pi^-\pi^0$ at the photon point. Black and red circles are double-pion data from [32]. Green and brown circles are double-pion data from [37]. Blue circles are three-pion data from [38].

All generated events are passed through GSIM, GPP and RECSIS. The parameters for the simulation are taken to be the same as in [39]. After applying all cuts and corrections described above, the reconstructed events are compared with the data. As it is seen on the left side of Fig. 4.9 MC reconstructed events reproduce the data rather well.

On the right side of Fig. 4.9 the average efficiency in five-dimensional kinematical cell is shown as functions of the hadron variables that describe the double-pion final state. No distributions show any significant efficiency variation.

The efficiency in some five-dimensional cells is not determined precisely enough, this leads to the fact that the cross sections obtained in them are not reliable. These cells should be excluded from the analysis and treated as empty cells (see Sect. 4.5). In order to determine

the criterion for cell exclusion the distribution shown in Fig. 4.10 is produced. This figure shows the relative efficiency error (absolute efficiency error is given by 4.2.14) that is plotted versus efficiency, color code in this figure represents the number of five-dimensional cells. As it is seen in Fig. 4.10 cells with relative efficiency errors greater than 30% are clustered along horizontal stripes. This effect can be explained taking into account that efficiency is obtained by division of two integer numbers, and it indicates too small statistics of generated events that in turn leads to higher efficiency errors. Moreover these horizontal stripes contain many cells with extremely small efficiency values that one can not count on anyway. Therefore, the five-dimensional cells that are located above the horizontal red line in Fig. 4.10 are excluded from the analysis and treated as empty cells (see Sect. 4.5).

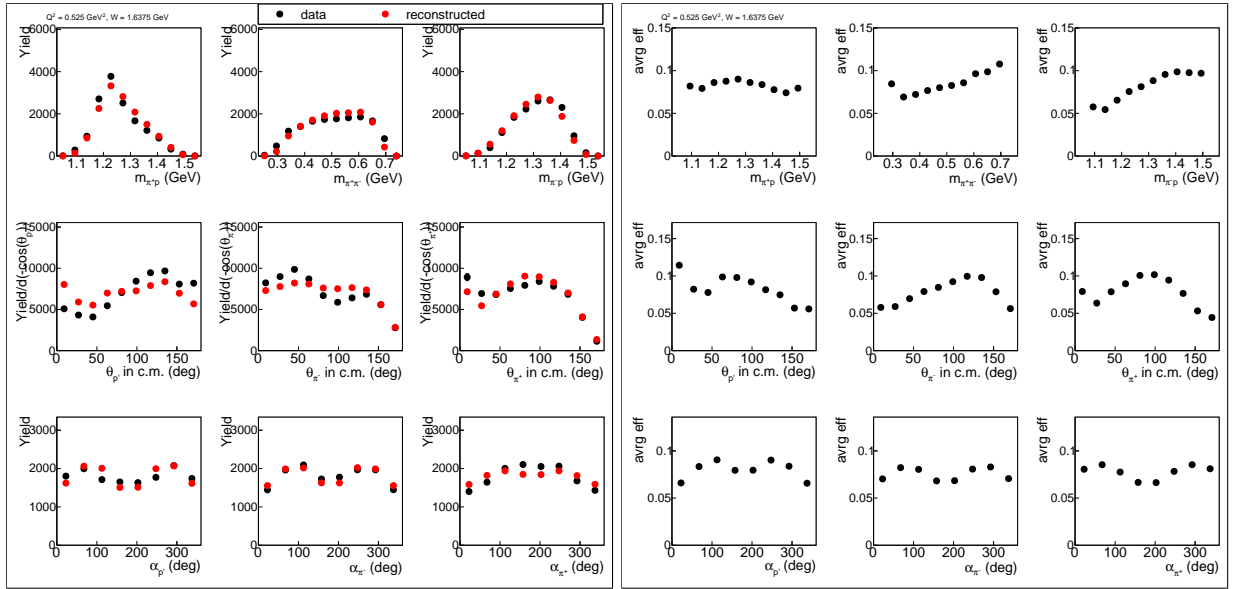


Figure 4.9: Plots in the left frame show the comparison of data and reconstructed MC yields as functions of various hadronic variables that describe the double-pion final state. Plots in the right frame show the average efficiency in the five-dimensional kinematical cell as functions of the final state hadronic variables. All distributions are given for one particular bin in W and Q^2 ($W = 1.6375 \text{ GeV}$, $Q^2 = 0.525 \text{ GeV}^2$).

4.5 Filling kinematical cells with zero acceptance

Since the CLAS detector does not cover full 4π solid angle, there are some blind areas or so-called "empty cells" in the kinematic phase space of the double-pion production. In the case when fully differential cross sections are obtained (for example in single pion production analyses) the presence of these cells is not a problem of big importance. Due to the statistical limitations in the double-pion analyses only the single-differential cross sections

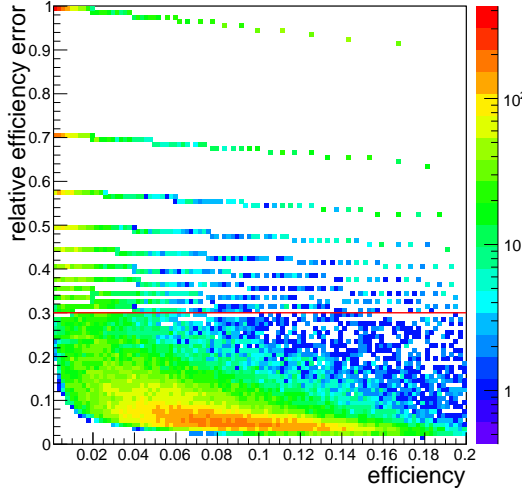


Figure 4.10: Relative efficiency error versus efficiency for one particular bin in W and Q^2 ($W = 1.6375$ GeV, $Q^2 = 0.525$ GeV 2). Color code shows the number of five-dimensional cells.

can be obtained. It means that the five-differential cross sections need to be integrated over four variables (see formulae 4.2.11). To obtain correct integrals, some assumptions on the cross sections in the empty cells are needed. It makes the problem of filling empty cells a point of special attention.

The map of the empty cells is determined by the Monte Carlo simulation. A cell is treated as empty, if it contains generated events, but does not contain any reconstructed events. One should not confuse these cells with those that contain both generated and reconstructed events, but do not contain data. The latter do not contain real events due to the limited experiment duration, and should not be filled since normalization on the charge in Faraday cup is applied.

To consider contributions from empty cells to the integrals (4.2.11) in detail model assumptions on the cross sections in these cells are needed. Recently for the purpose of the development of new double-pion event generator [33] a special procedure that allows to obtain the five-differential double-pion cross sections in the given kinematical cell was worked out. This procedure employs the five-differential cross sections from the recent version of the JM15 model fit to all results on charged double pion photo- and electroproduction cross sections from CLAS (both published and preliminary [1, 6, 7, 40]). In the area not yet covered by CLAS data an additional extrapolation technique was applied, that included additional world data on W dependencies of double-pion photoproduction integrated cross sections [32, 37]. The set of the cross sections obtained using this procedure was used for the purpose of filling empty cells in this analysis.

In Fig. 4.11 the single-differential cross sections are plotted for the two cases: when empty cells are not filled (red circles) and when empty cells are filled by the way described above

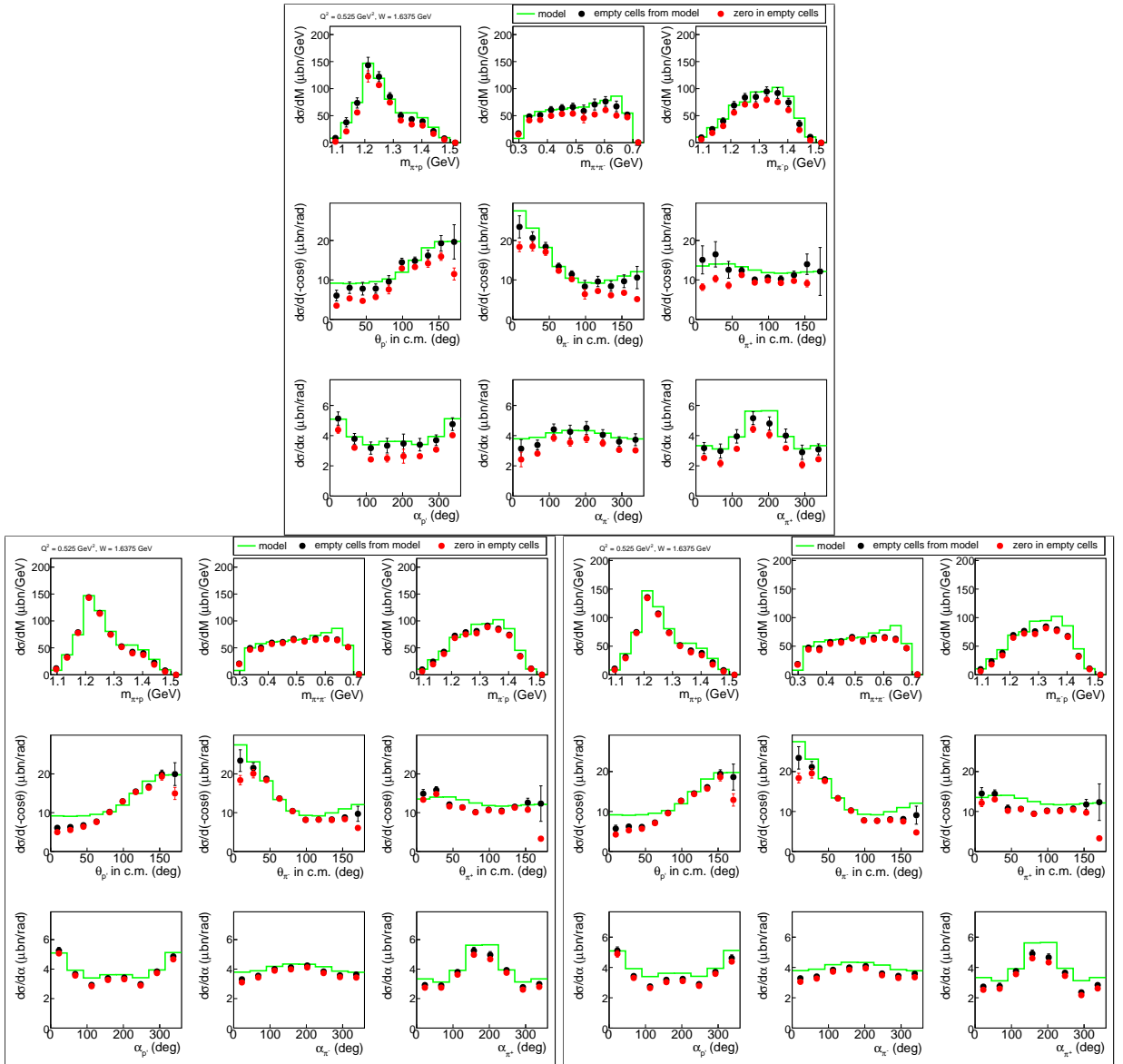


Figure 4.11: Comparison of various ways of combining topologies. Plots in the top frame are for the case when the cross sections are obtained using the topology where π^- is missing combined with the exclusive topology. Plots in the bottom left frame are for the case when the cross sections are obtained using the sum of data and reconstructed events for all four topologies. Plots in the bottom right frame are for the case when the cross sections are obtained using the selection of five-dimensional cells based on the maximum efficiency. See text for more details. In all plots the red circles are for the cross sections with unfilled empty cells and the black circles are for the cross sections with filled empty cells. Green curves show the cross sections that are used for the purpose of filling empty cells. All distributions are given for one particular bin in W and Q^2 ($W = 1.6375 \text{ GeV}$, $Q^2 = 0.525 \text{ GeV}^2$).

836 (black circles). The cross sections that are used to fill empty cells are shown by the green
837 curves. The plot in the top frame of Fig. 4.11 corresponds to the topology where π^- is missing
838 combined with the exclusive topology, while the two plots in the bottom frames correspond
839 to different ways of combining of all available topologies (ways in which the topologies may
840 be combined are described in more detail in Sect. 4.6).

841 The plot in the left bottom frame in Fig. 4.11 corresponds to the method of the topologies
842 combination that is selected to be the best. As it can be seen in the left bottom frame in
843 Fig. 4.11 the contribution from empty cells to the total cross sections is reasonably small.
844 Although the cross sections that are used to fill empty cells describe the data well an ad-
845 dditional 50% relative error is assigned to the part of the cross section that comes from the
846 empty cell contributions. For finally obtained cross sections (shown by black circles) this
847 additional error is combined with the total statistical one.

848 4.6 Combination of various topologies

849 It is mentioned in Sect. 3.4 that the topology where π^- is missing combined with the exclusive
850 one accounts about 80% of all double-pion events. In previously published analyses [6, 41]
851 only these two topologies were used to obtain final cross sections.

852 In this analysis it is found that the use of only the combination of the exclusive and
853 π^- missing topologies leads to significant contributions from empty cells to the total cross
854 sections in some phasespace regions (see plot in the top frame of Fig. 4.11). Moreover, the
855 last point in θ_{π^+} angular distribution does not contain data at all and the cross section in this
856 point is totally determined by the procedure of filling empty cells as described in Sect. 4.5.

857 Hence to minimize the part of the cross section that comes from filling of the empty cells
858 and therefore the model dependence of the obtained cross sections, it was decided to use all
859 available topologies.

860 There are two methods in which topologies can be combined. One of them is chosen as
861 preferable and used to obtain the final cross sections. In this method data events for all
862 topologies are summed up in each five-dimensional kinematical cell. The same is done for
863 the reconstructed events, while the number of generated events remains the same. Then
864 the cross sections are calculated in a usual way. The cross sections for the case when all
865 topologies are combined by this method are shown in the bottom left frame of Fig. 4.11.
866 One can see that the usage of this method allows to minimize the part of the cross section
867 that comes from the empty cells contributions in comparison with the case when only the
868 exclusive and π^- missing topologies are used. Moreover even the last point in θ_{π^+} angular
869 distribution now is partially determined by data and therefore less model dependent.

870 Another way to combine topologies is used to check the consistency of the results. In this
871 way in each five-dimensional kinematical cell reconstructed and data events are taken from

872 the topology that has maximum efficiency, while the number of generated events remains the
873 same. The cross sections that are obtained using this method are shown in the bottom right
874 frame of Fig. 4.11. Although this method gives almost the same result as the previous one,
875 it has several shortcomings. One of them is slightly bigger contribution from empty cells.
876 Another one is the fact that this method does not allow to use the whole available statistics
877 of the data. As a result the error of the obtained cross sections becomes a little bit higher
878 than in the previous method. That is why this method is not chosen as a primary one. The
879 difference between the cross sections obtained by the two methods described above is used
880 as part of the systematical error of the integrated cross sections (see Sect. 6.2).

881 Finally it needs to be mentioned that independently of the way the cross sections are
882 calculated (see all plots in Fig. 4.11), the final cross sections obtained after filling the empty
883 cells are very close to each other. That indicates the stability and reliability of the cross
884 section extraction procedure.

885 **Chapter 5**

886 **Correction for binning effects**

887 Since the bins in which the cross sections are obtained have finite sizes, the cross section
888 values can be distorted due to the averaging within the bins. For instance, if there is a
889 sharp peak in the middle of a bin, then the average value of the cross section in that bin
890 will always be smaller than the peak value. Any non-linear behavior of the cross section will
891 likely result in an offset of the obtained value. There are two ways to deal with this issue.
892 Either one uses the corrected values of the kinematical quantities associated with the bin,
893 instead of the central values or one calculates the correction to the cross section in the center
894 of the bin. In this analysis the second method is chosen, in order to keep the initial binning
895 over kinematical variables. For that purpose some model assumption about the cross section
896 behavior is needed. The ratio of the model value at the center of the bin to the model value
897 averaged within the bin is considered as a multiplicative correction factor, and the corrected
898 cross section is found as

$$\begin{aligned}\sigma_{corr} &= \sigma_{uncorr} \times C_{bin} \quad \text{with} \\ C_{bin} &= \frac{\sigma_{model,cntr}}{\sigma_{model,avg}},\end{aligned}\tag{5.0.1}$$

899 where σ_{uncorr} is the experimental cross section value before binning corrections, $\sigma_{model,cntr}$
900 is the cross section from the model in the center of the data bin, and $\sigma_{model,avg}$ is the cross
901 section from the model averaged in data bin.

902 In the first step the corrections are applied to all single-differential cross sections. For
903 the model cross sections the cubical spline approximation is chosen. The results are shown
904 in Fig. 5.1. The black and red points in this figure stand for the cross sections before
905 and after binning corrections, respectively, while the curves correspond to the model. For
906 the invariant masses and θ angular distributions splines are forced to pass through the
907 intermediate points that are obtained by averaging of two neighboring cross section points.
908 This method reduces the splines sensitivity to accidental cross section fluctuations. For the
909 α distributions another method is chosen. As it seen in Fig. 4.11 the obtained α distributions
910 are slightly asymmetrical. However after the integration over φ , the cross section must be

symmetrical with respect to the α angle. So, it was decided to force the splines to pass through the points that are obtained by averaging the cross section values in the points that are symmetrical with respect to $\alpha = 180^\circ$.

After that the corrected single-differential cross sections are integrated and corrected to the Q^2 dependence inside the Q^2 bins and the W dependence inside the W bins. In Fig. 5.2 integrated cross sections are shown as functions of Q^2 (left plot) and W (right plot) before (black points) and after (red points) binning corrections. To fit the Q^2 dependencies a second order polynom is chosen, while for W distributions cubical splines are the best choice (splines are forced to pass through the intermediate points that are obtained by averaging two neighboring cross section points). These assumptions for Q^2 and W cross sections behaviors are shown by the curves in Fig. 5.2.

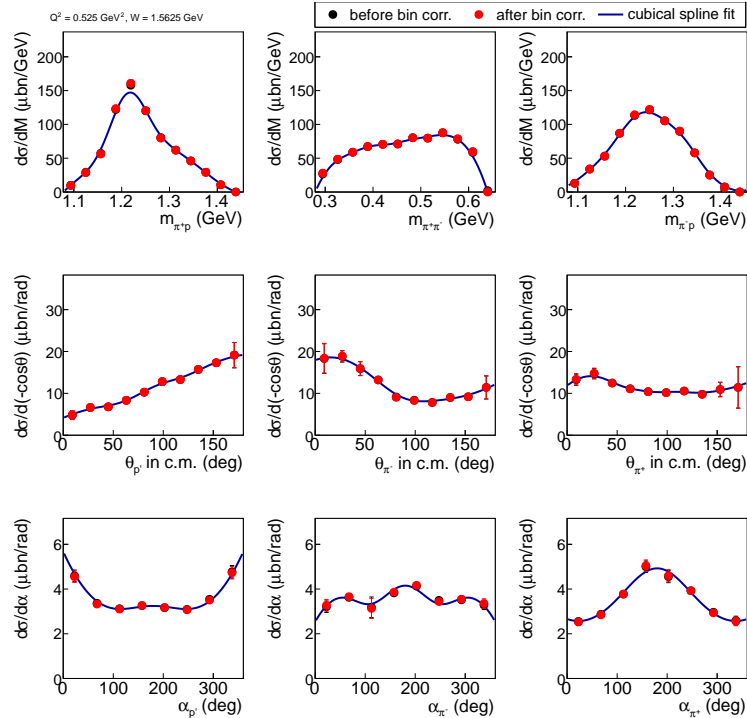


Figure 5.1: The single-differential cross sections as functions of the final hadron variables for one particular bin in W and Q^2 ($W = 1.5625 \text{ GeV}$, $Q^2 = 0.525 \text{ GeV}^2$) before (black points) and after (red points) the binning corrections. Curves stand for the cubical spline approximation.

Since in this analysis the detailed binning over all kinematical variables is chosen, the effect of the binning correction is rather small ($\sim 1\%$) and only in some points at low W it can rise up to 4%. That is why in the Figs. 5.1 and 5.2 the black points (before the correction) are almost completely covered up by the red ones (after the correction).

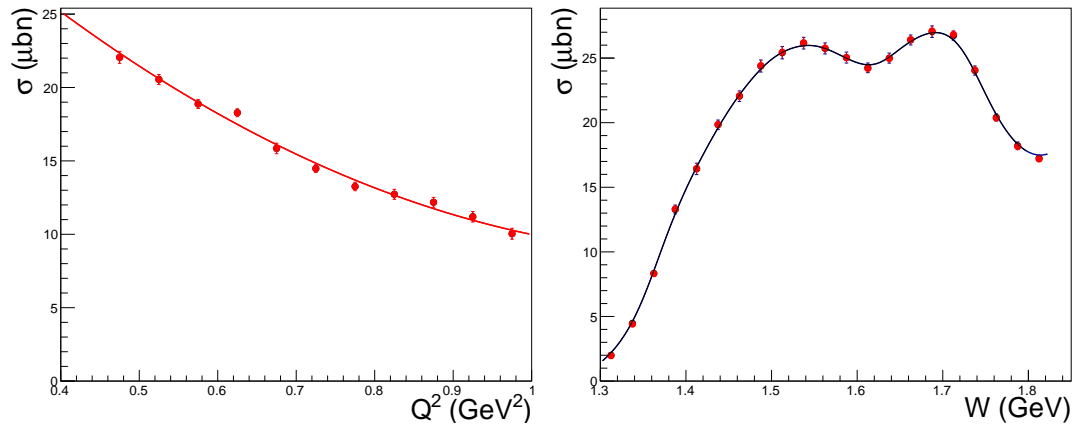


Figure 5.2: Q^2 dependence of integral cross section at $W = 1.4625 \text{ GeV}$ (left plot) and W dependence of integral cross section at $Q^2 = 0.475 \text{ GeV}^2$ (right plot). On both plots black and red points correspond to the cross sections before and after the binning corrections, respectively. The curve on the left plot represents the second order polinomial fit, while the curve on the right plot correspond to the cubical spline approximation.

₉₂₆ **Chapter 6**

₉₂₇ **Systematical errors**

₉₂₈ **6.1 Errors due to normalization, electron identifica-**
₉₂₉ **tion, and electron detection efficiency**

₉₃₀ One of the main sources of systematical errors in this experiment is the uncertainty in
₉₃₁ the normalization. This can arise from miscalibrations of the Faraday cup, target density
₉₃₂ instabilities, and errors in determining the target length and its temperature, DAQ live-time,
₉₃₃ and other factors. However, the presence of the elastic events in the data set allows to check
₉₃₄ the normalization of the cross sections by comparing the elastic cross sections to the world
₉₃₅ data. In this way one can combine normalization, electron detection, electron tracking,
₉₃₆ and electron identification errors into one global uncertainty factor. In Fig. 6.1 the ratio of
₉₃₇ the measured elastic cross section to a parametrization of the elastic cross sections [42] is
₉₃₈ shown. The parametrized cross sections are "radiated" and the elastic cross sections from
₉₃₉ the CLAS data are not corrected for radiative effects. As it is seen in Fig. 6.1, all the points
₉₄₀ are within the green lines that indicate $\pm 5\%$ offsets. This procedure allows to assign a 3%
₉₄₁ global uncertainty due to normalization, electron identification, and electron efficiency.

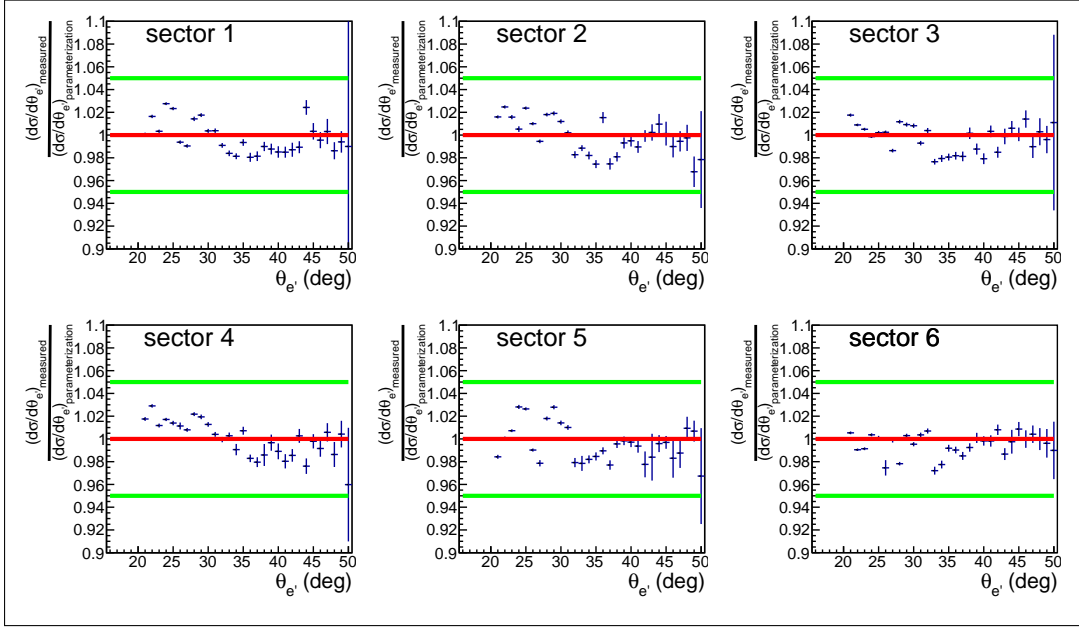


Figure 6.1: Ratio of the elastic cross section to the parametrization [42], plotted versus $\theta_{e'}$ angle of the electron in the lab frame for the six CLAS sectors. Red lines correspond to unity and green lines indicate a $\pm 5\%$ deviation from the parametrization.

942 6.2 Errors due to the different ways of combining 943 topologies

944 In this analysis two ways of combining topologies are used (see Sect. 4.6). The integrated
945 cross sections obtained in these two ways are slightly different. As in the case of the integration
946 over different kinematical grids, this difference is interpreted as systematical error.
947 Since different topologies correspond to the different registered final hadrons (and therefore
948 to the different hadron cut combinations) this systematical error includes partially the error
949 due to the shapes of the cuts that are used in the analysis. The error is calculated for each
950 bin in W and Q^2 and typically is of the order of 2%.

951 6.3 Errors due to the integration over different final 952 hadron variables

953 As it is mentioned in Sect. 4.1 three sets of kinematical variables are used in this analysis. The
954 cross sections obtained by integration over these three kinematical grids should be the same.
955 However, it is found that they are slightly different due to the fact that data and efficiency
956 propagate differently to the different kinematical grids. This difference is interpreted as

957 systematical error and computed for each bin in W and Q^2 . This systematic effect varies
958 depending on the bin in W and Q^2 and is typically of the order of 5%.

959 6.4 Systematical error summary

960 As final integrated cross sections, the cross sections that are averaged over three grids of the
961 kinematical variables are reported (see Fig. 6.2). In Fig. 6.2 the systematical uncertainties
962 are shown as the red bands at the bottom of each plot. This uncertainties include the errors
963 due to the effects mentioned above and extra 5% global error due to the inclusive radiative
964 corrections procedure (see Sect. 4.3). To obtain the red bands all the errors are summed up
965 in quadrature.

966 The statistical cross section uncertainties are typically smaller than the systematical ones.
967 The total uncertainty is obtained as the sum of the systematical and statistical ones and is
968 shown by the hatched red areas in Fig. 6.2.

969 The typical values of the integral systematical errors with their sources are presented in
970 Tab. 6.1.

Error source	Error value
Normalization, electron id, and electron detection efficiency	3%
Different ways of combining topologies	$\sim 2\%$
Integration over different final hadron variables	$\sim 5\%$
Radiative corrections	5%

Table 6.1: The typical values of the integral systematical errors.

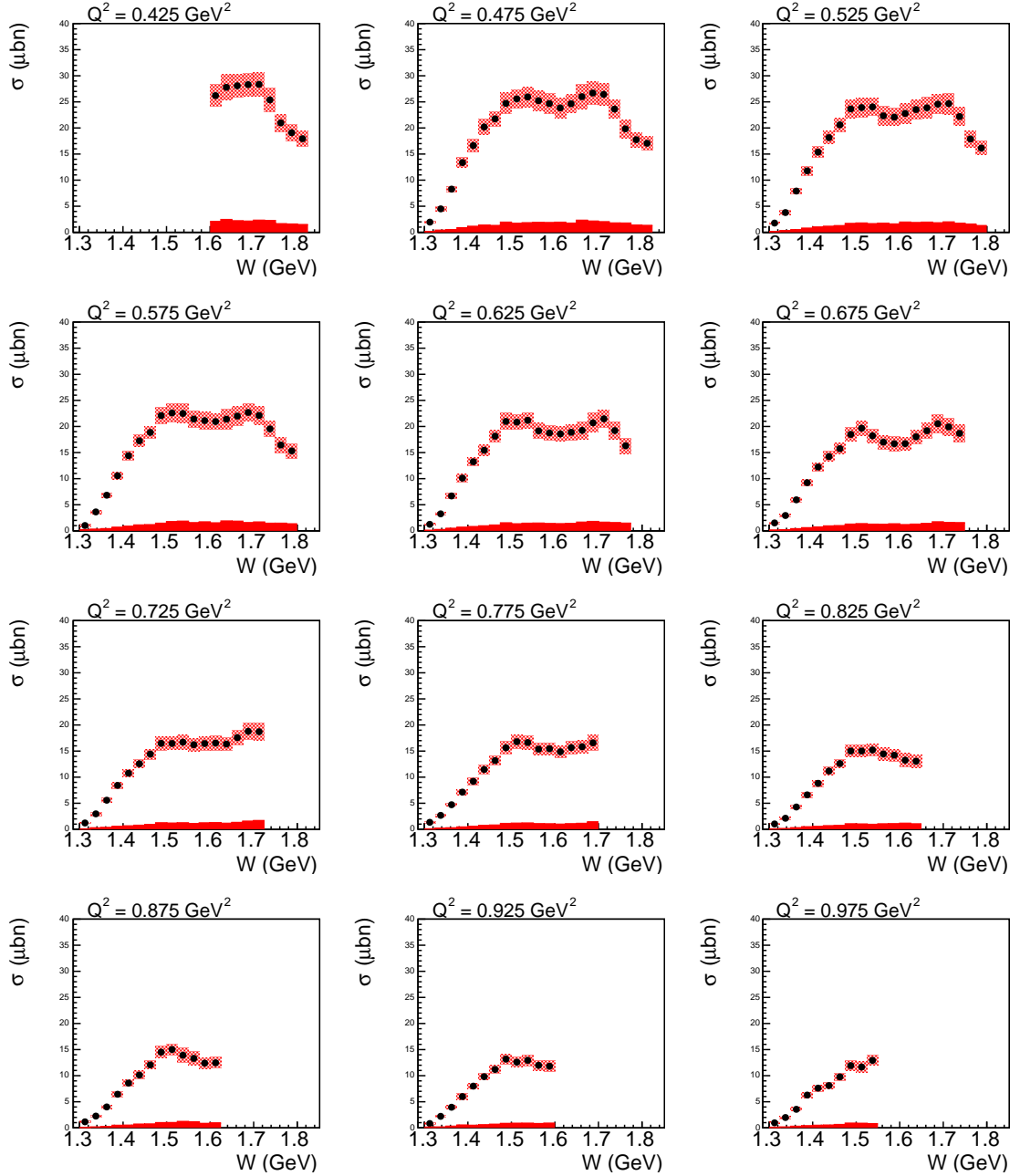


Figure 6.2: Systematical errors of the integrated cross sections. The plots show W dependencies of the integrated cross section in various bins in Q^2 . The systematical uncertainties are shown as the red bands at the bottom of each plot. The total cross section uncertainty (both statistical and systematical ones summed up in quadrature) is shown by the hatched red areas.

₉₇₁ Chapter 7

₉₇₂ Conclusions

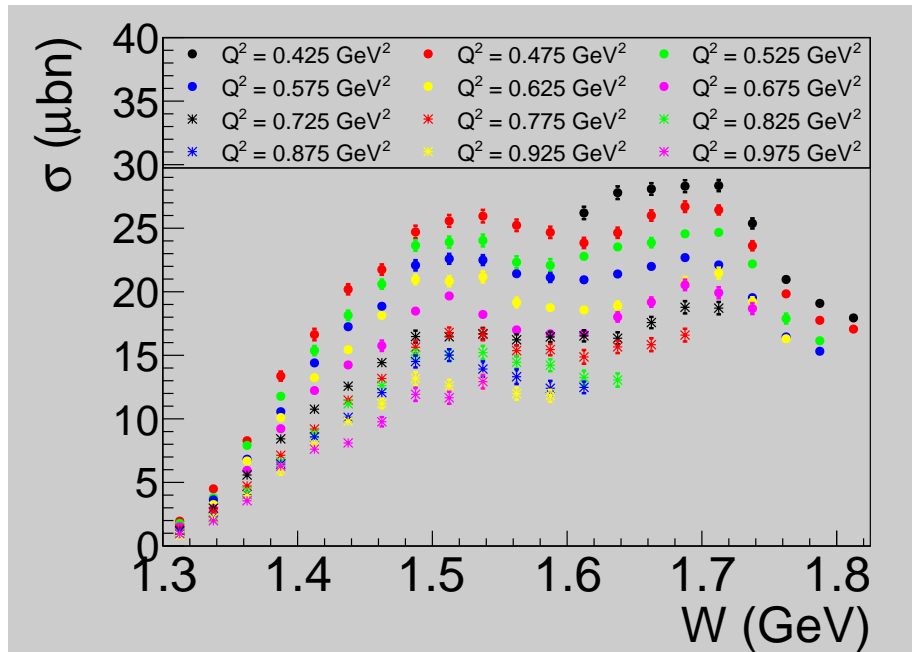


Figure 7.1: W dependencies of the integrated cross sections for various bins in Q^2 . The statistical errors are small and invisible under the symbols.

- ₉₇₃ • The complete set of the single-differential (see appendix A) and integrated cross sections (see Fig. 7.1) for the reaction $\gamma_vp \rightarrow p\pi^+\pi^-$ is obtained in the range of W from 1.3 GeV to 1.825 GeV and Q^2 from 0.45 GeV^2 to 1 GeV^2 . The Q^2 binning of the cross sections in the kinematical area of high-lying nucleon resonances is six times finer than in previously available data.
- ₉₇₄
- ₉₇₅
- ₉₇₆
- ₉₇₇

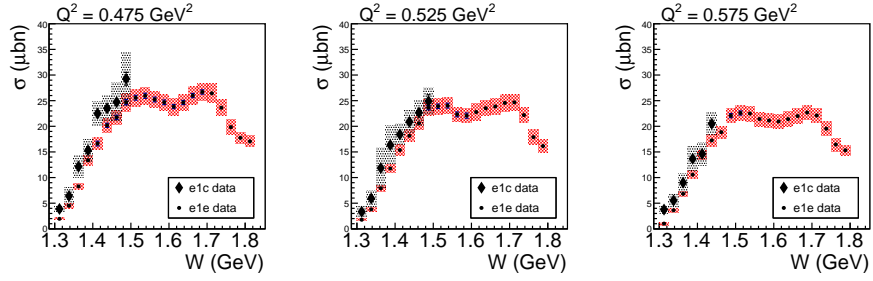


Figure 7.2: W dependencies of the obtained in this analysis cross sections (e1e dataset) in comparison with the cross sections from [6] (e1c dataset) for three bins in Q^2 . Hatched areas correspond to the total uncertainties (sistemtical and statistical).

- 978 • The comparison of the obtained cross sections with the available ones [6] shows the
979 reasonable agreement within the statistical uncertainties (see Fig. 7.2). It needs to be
980 mentioned that this comparison is not fully justified since the cross sections from [6]
981 and this analysis are obtained with different beam energies.
- 982 • The fit of these data by the meson-baryon reaction model JM [7–9] will provide for the
983 first time information on the Q^2 evolution of high-lying resonances with very detailed
984 binning.

₉₈₅ **Appendix A: Measured cross sections**

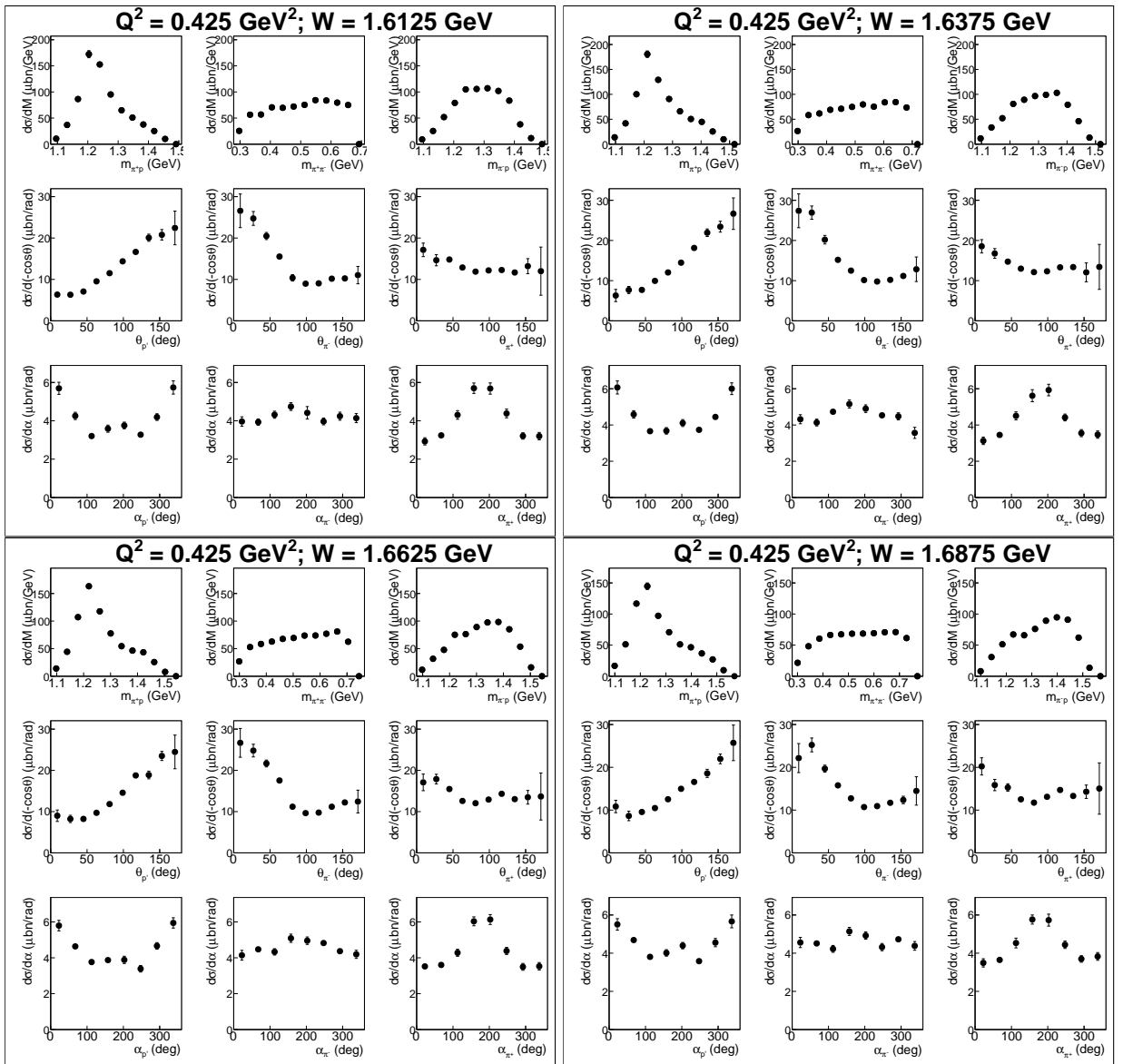


Figure A.1:

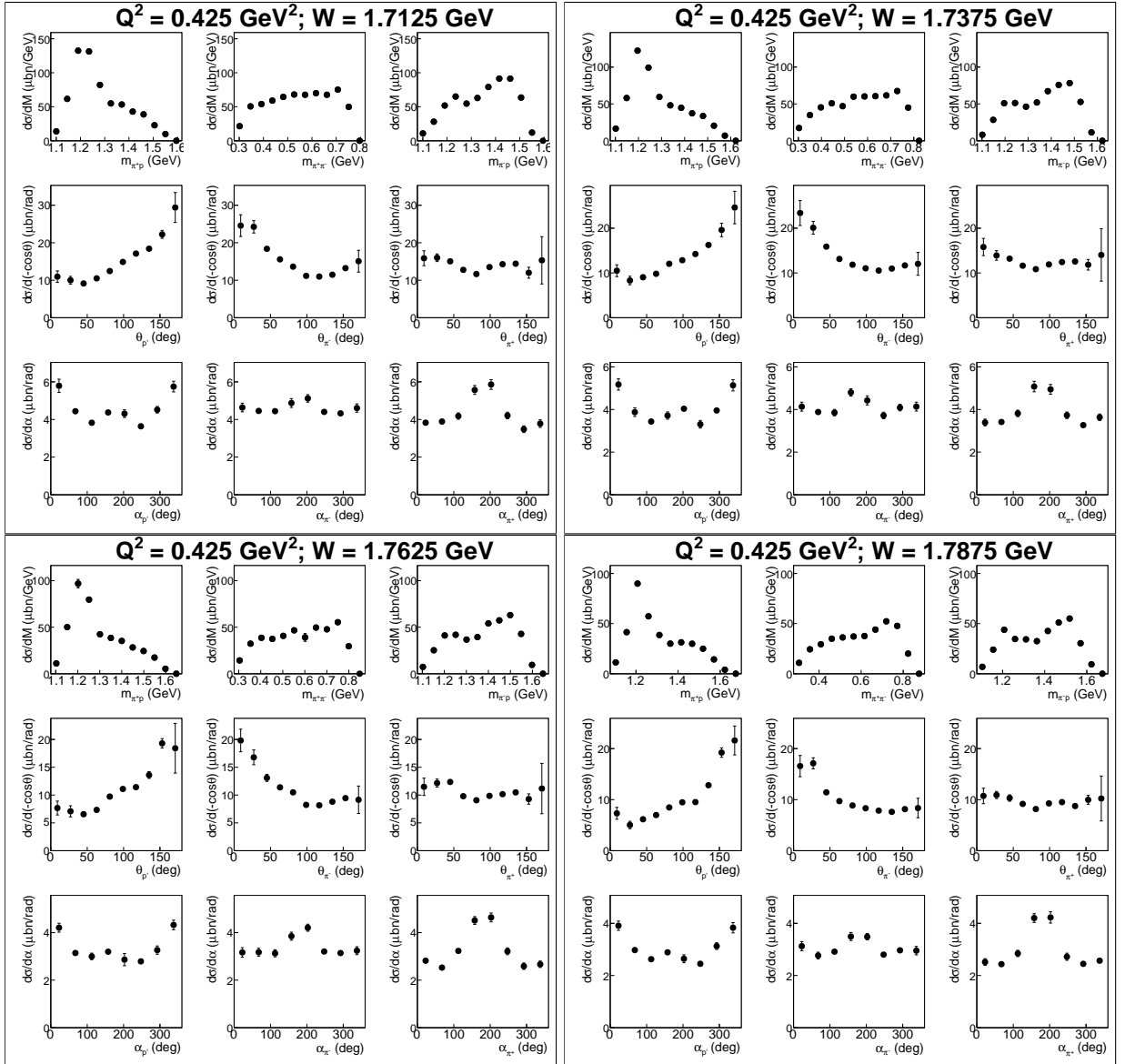


Figure A.2:

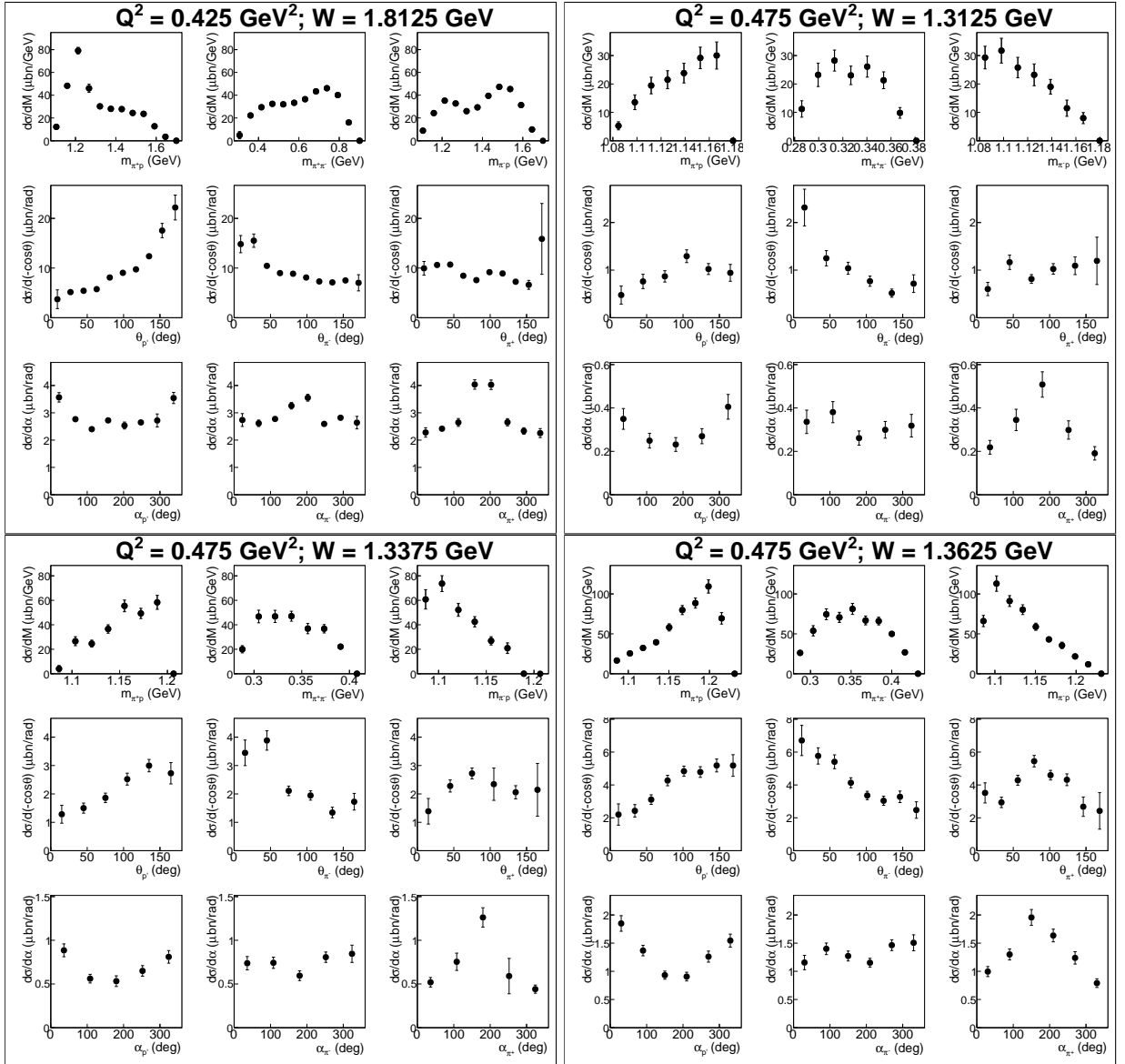


Figure A.3:

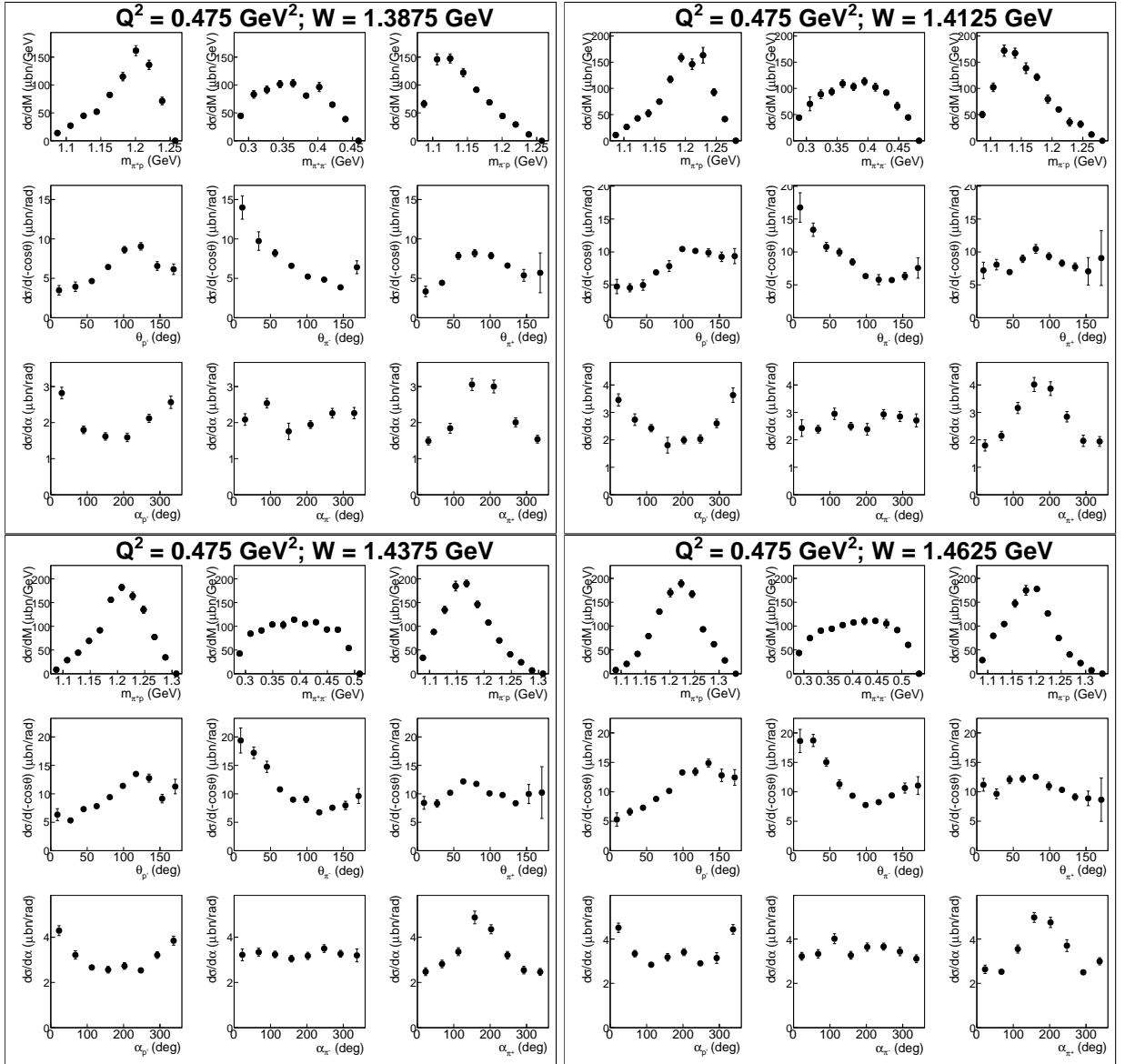


Figure A.4:

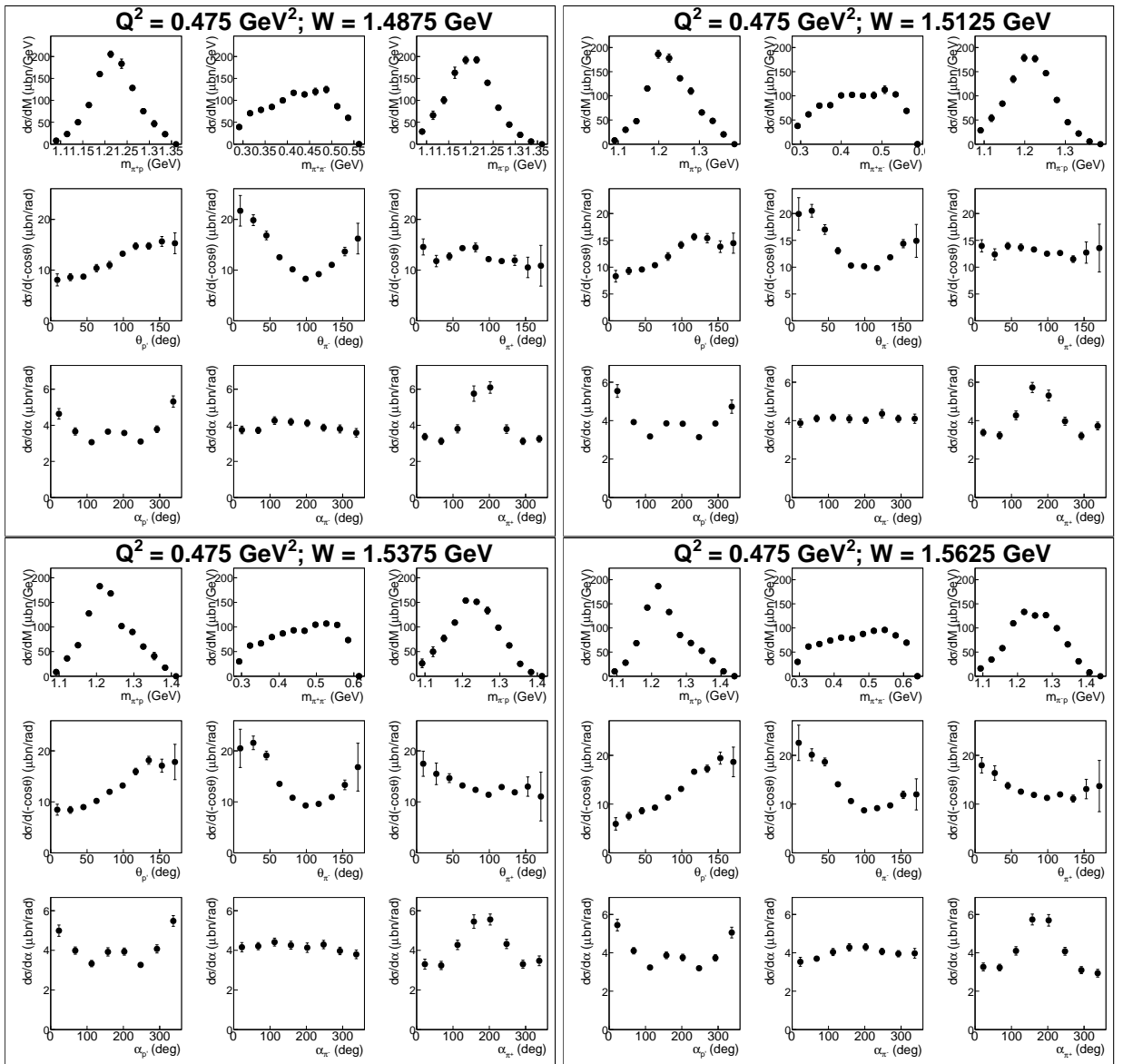


Figure A.5:

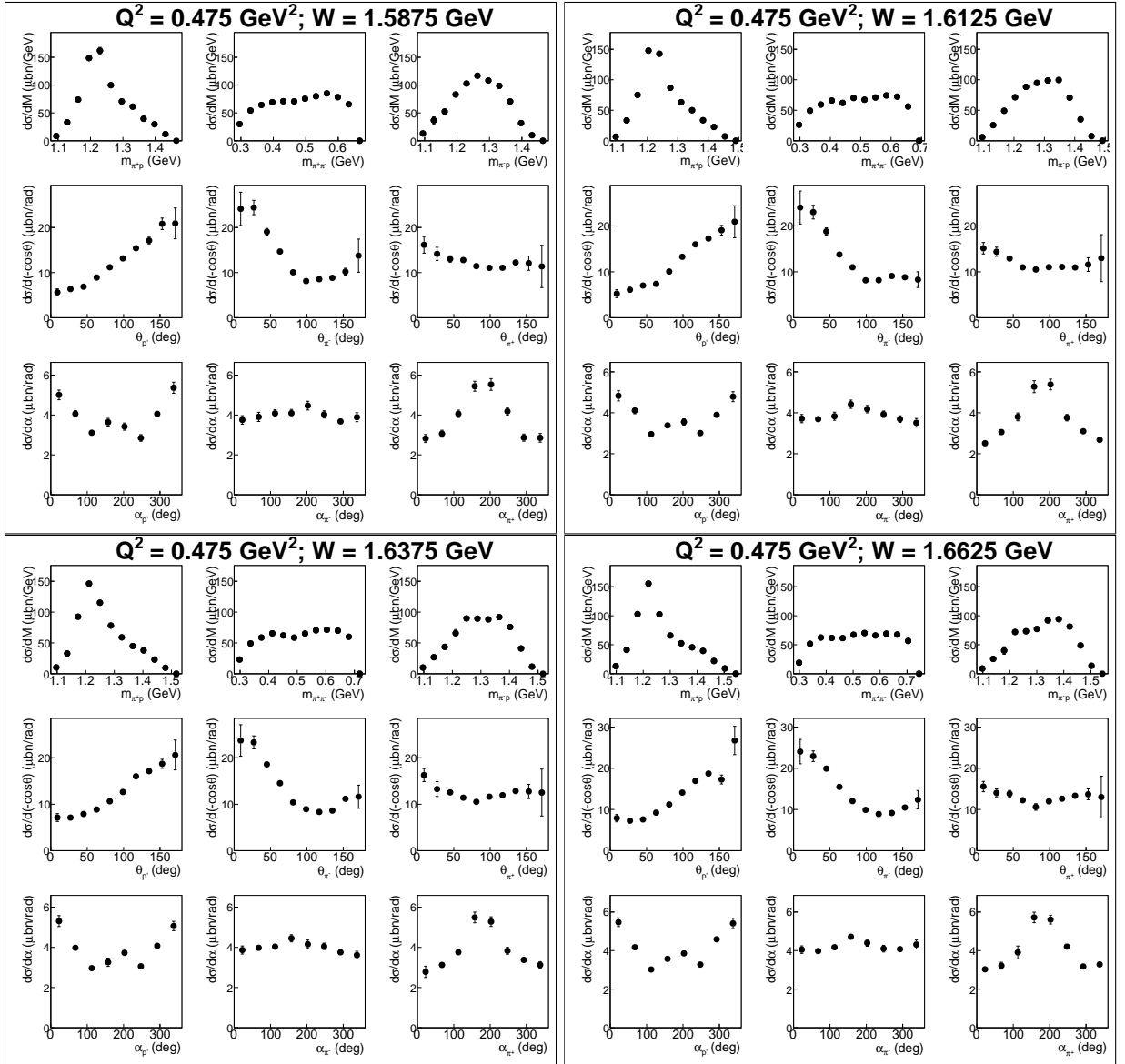


Figure A.6:

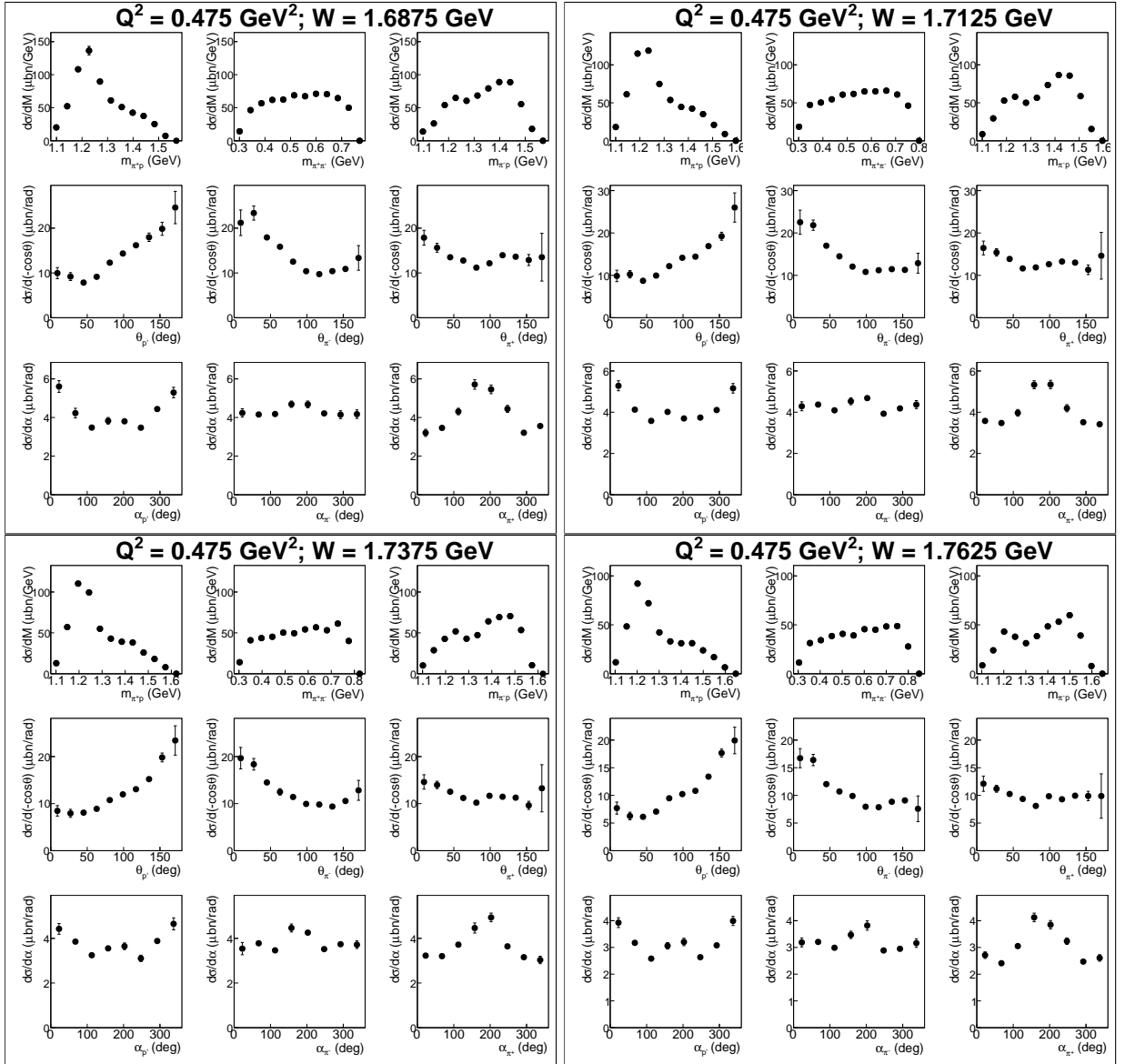


Figure A.7:

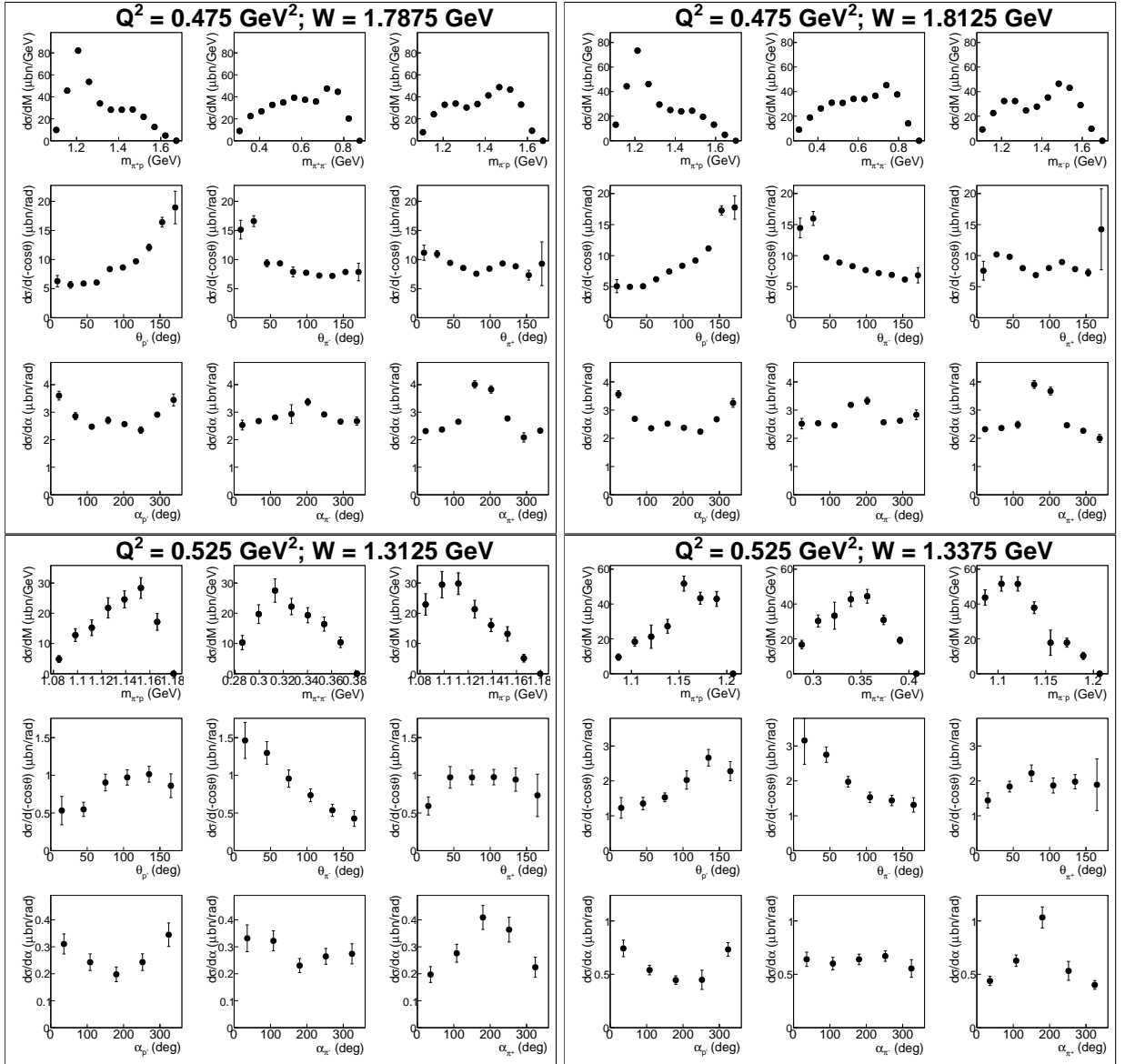


Figure A.8:

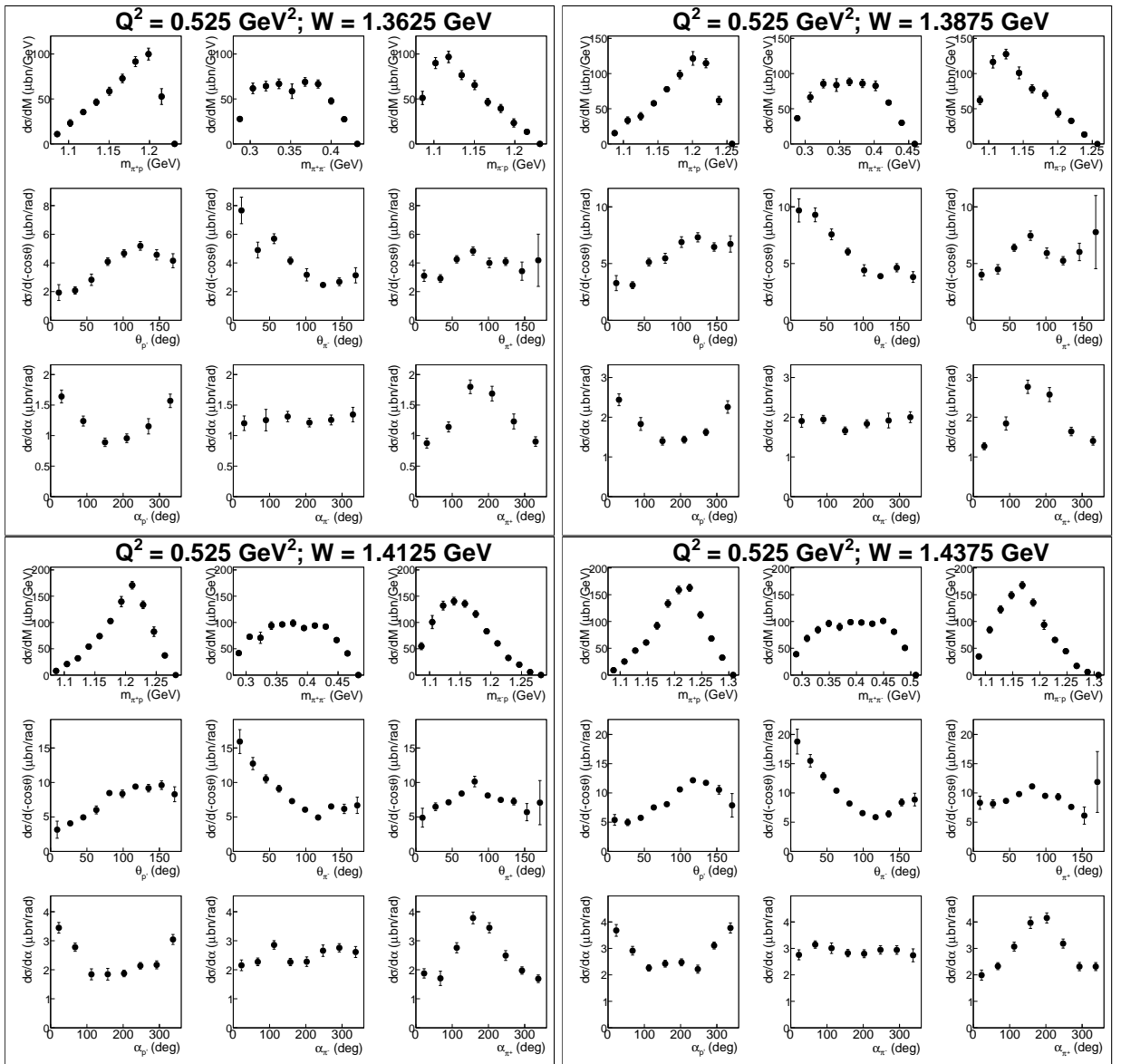


Figure A.9:

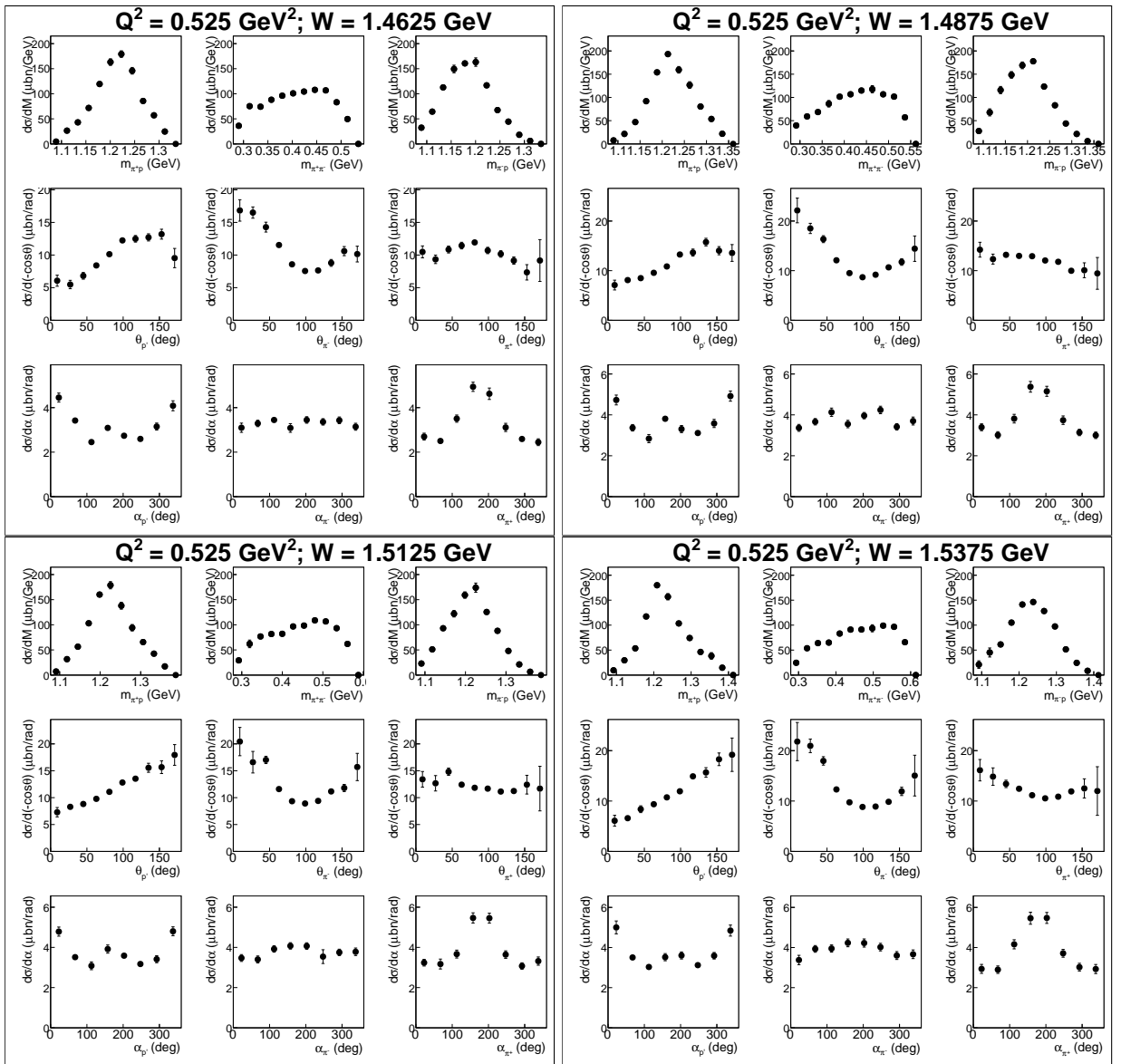


Figure A.10:

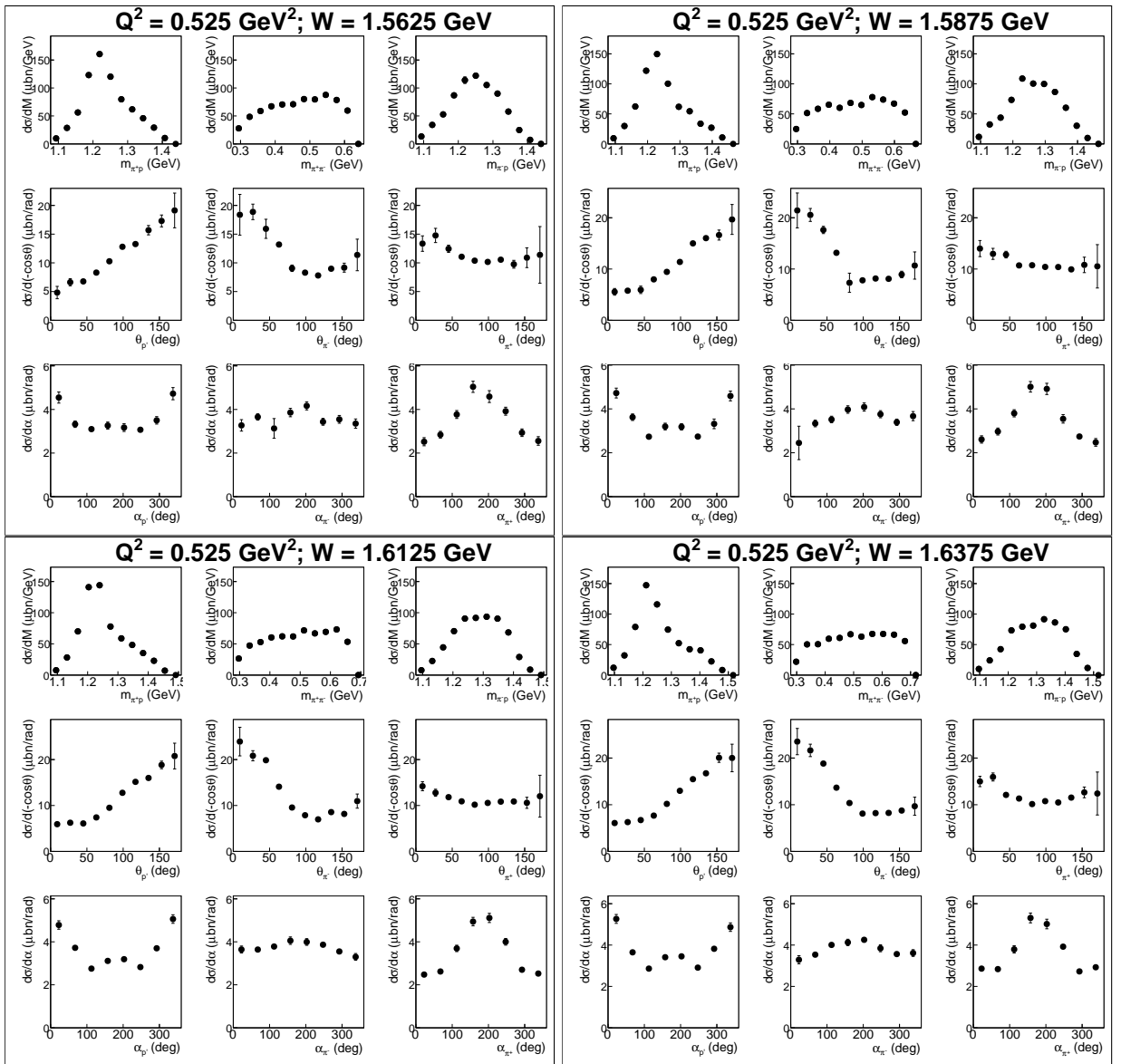


Figure A.11:

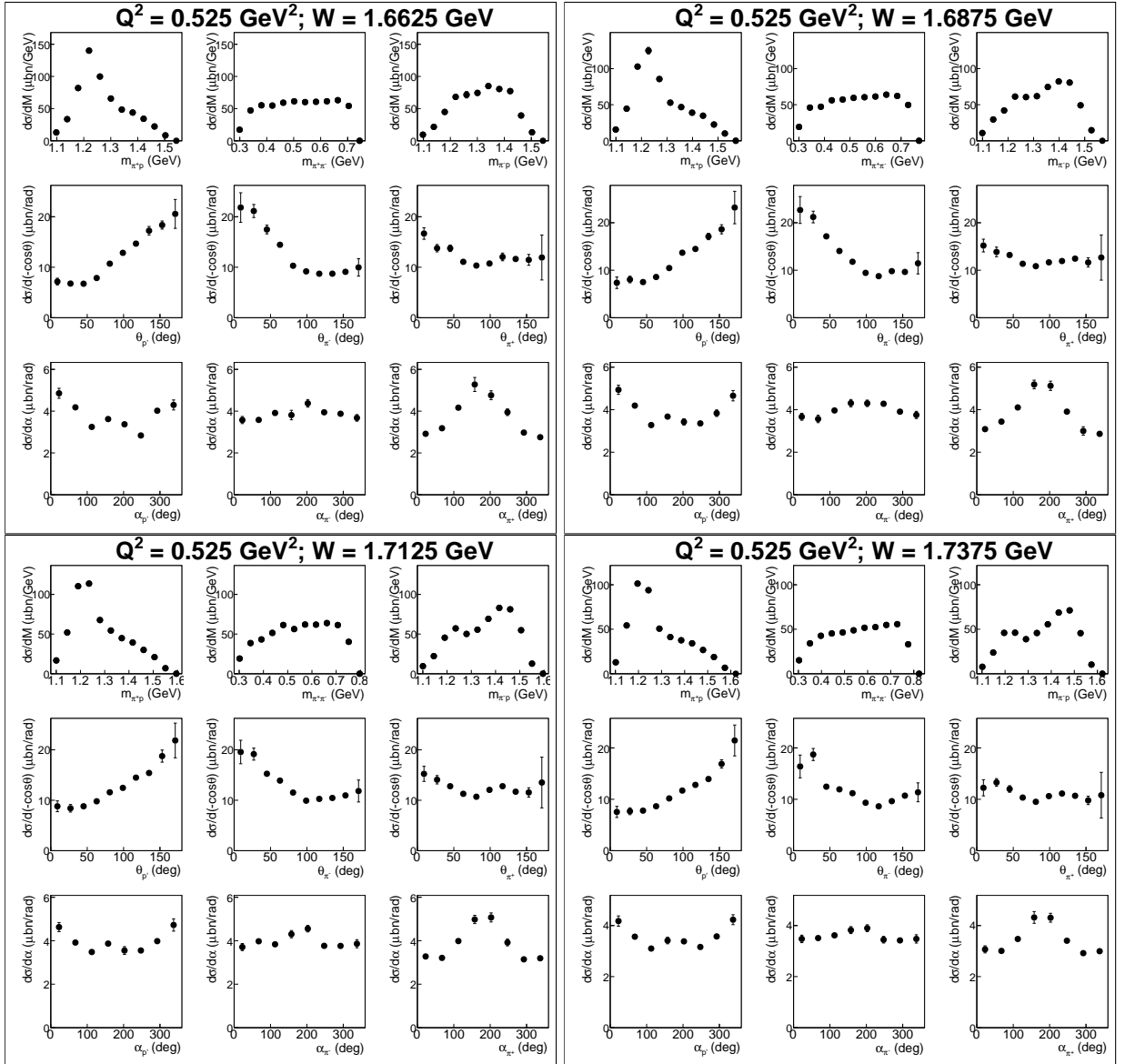


Figure A.12:

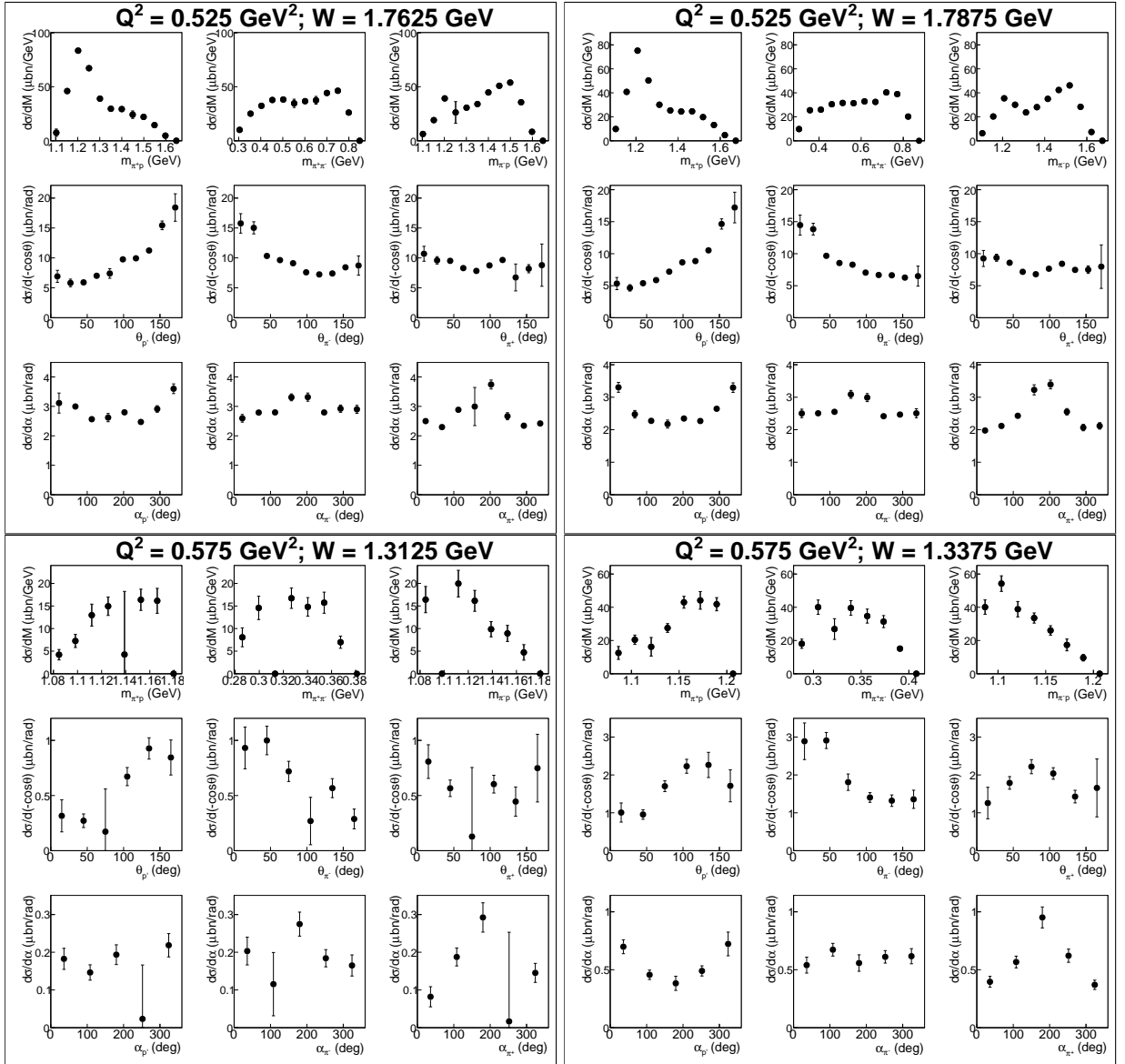


Figure A.13:

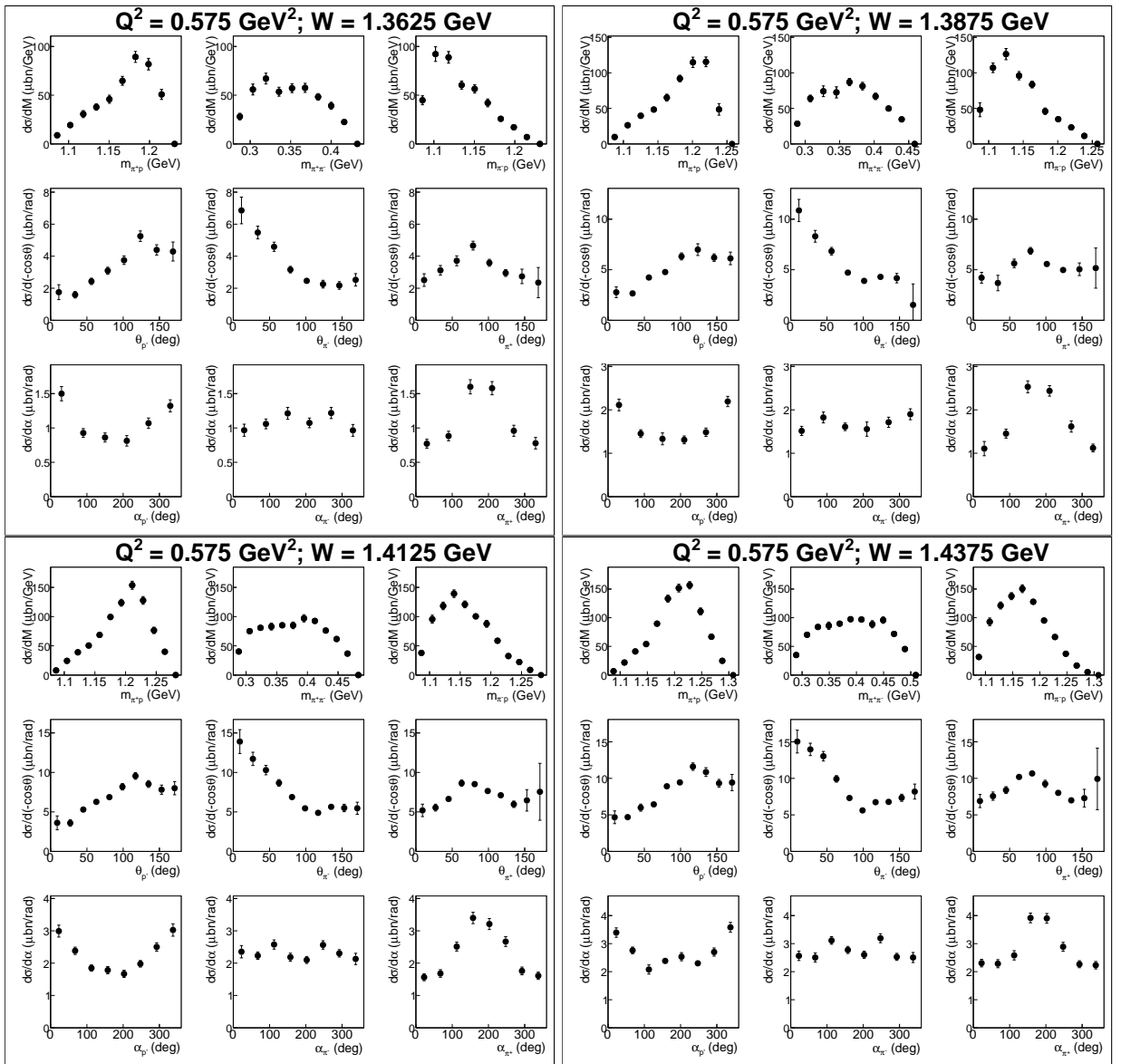


Figure A.14:

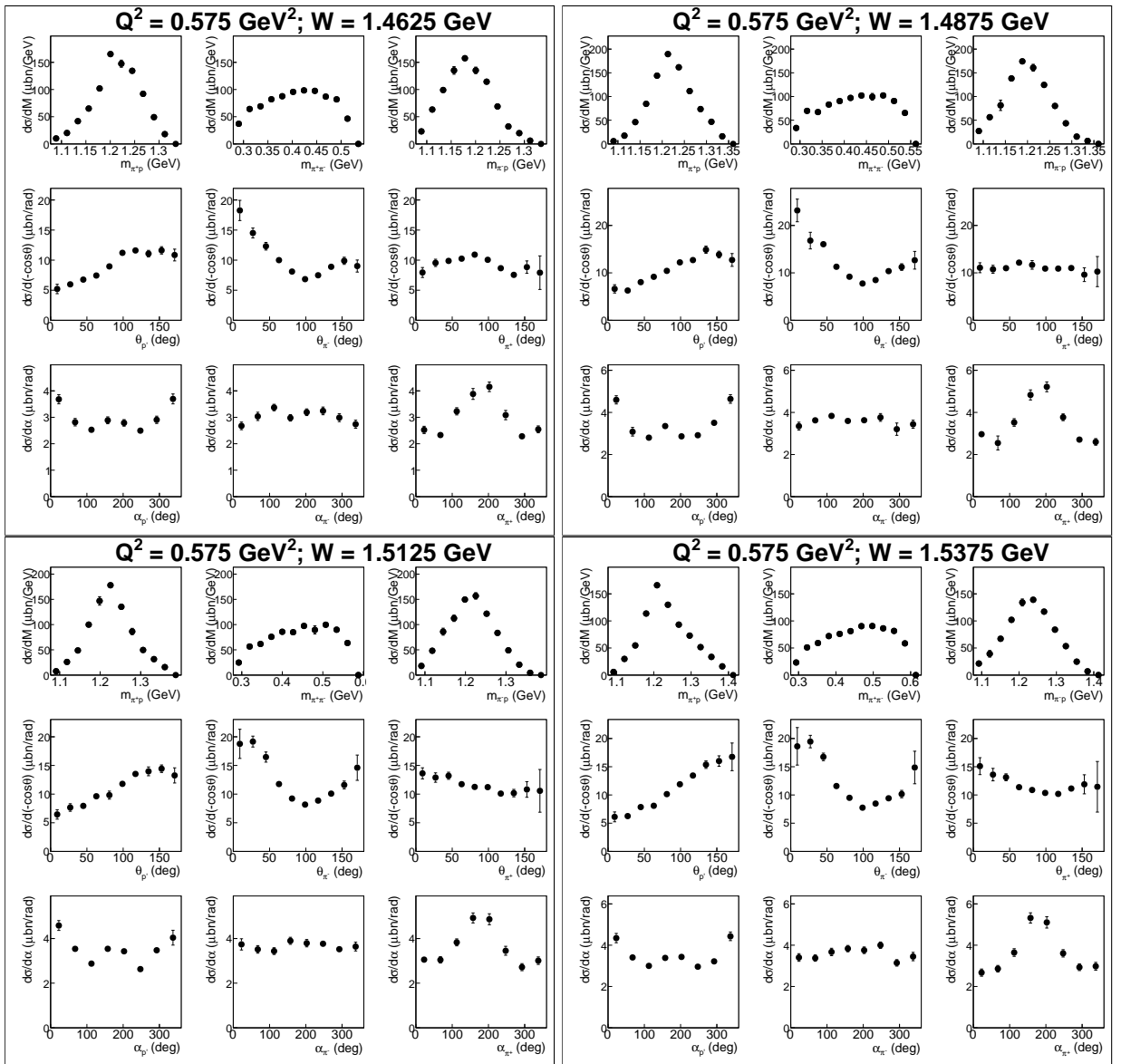


Figure A.15:

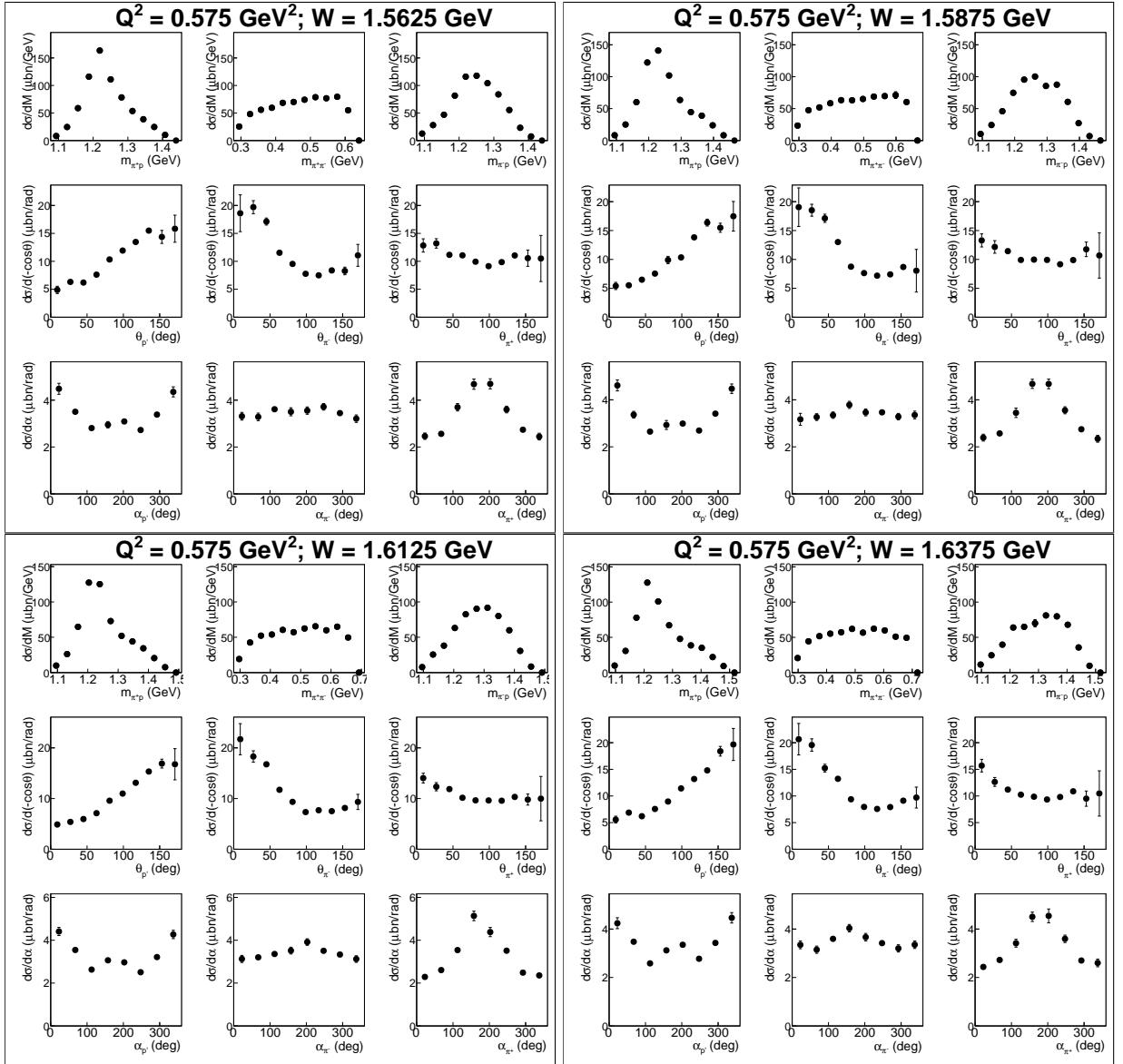


Figure A.16:

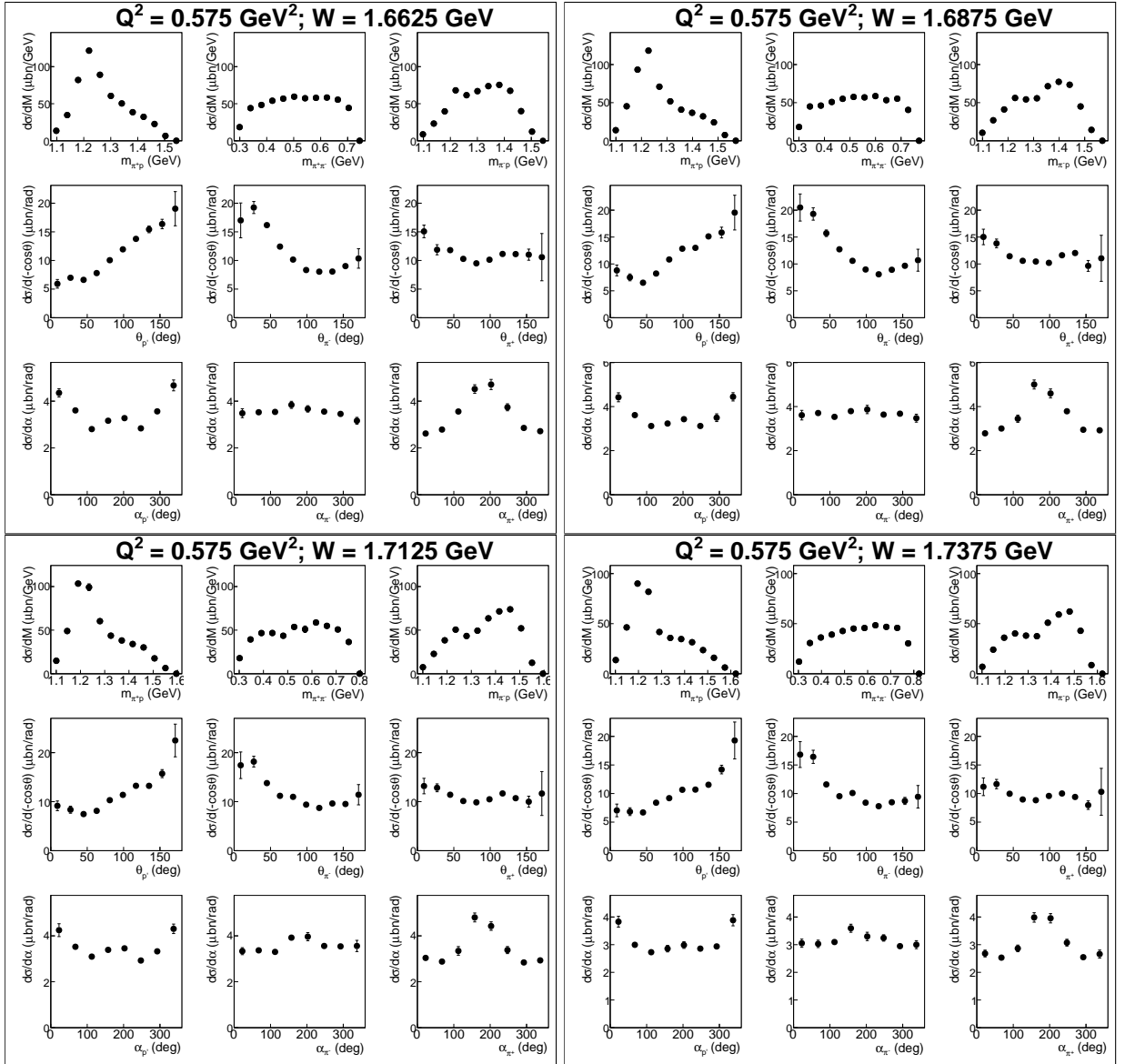


Figure A.17:

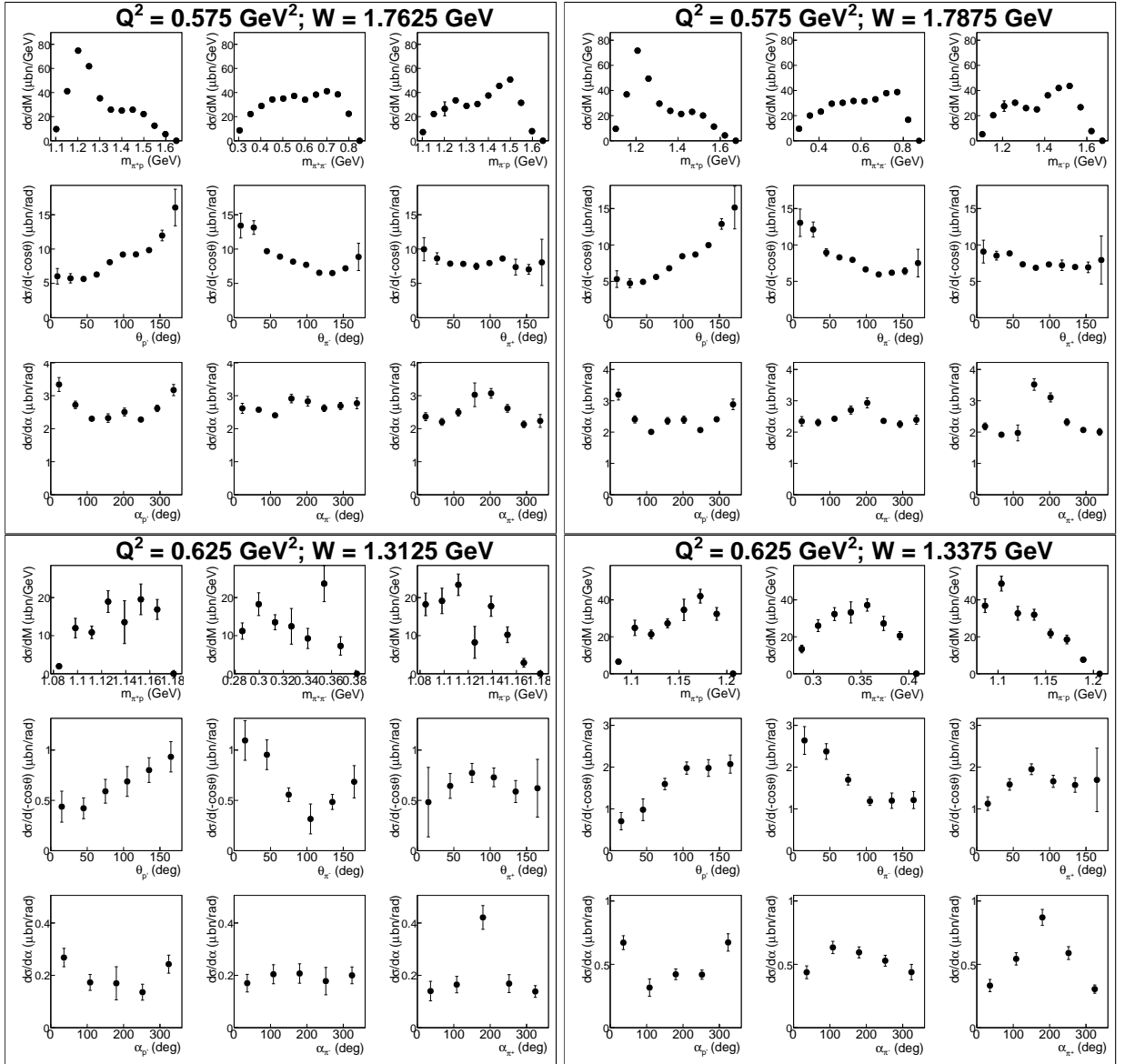


Figure A.18:

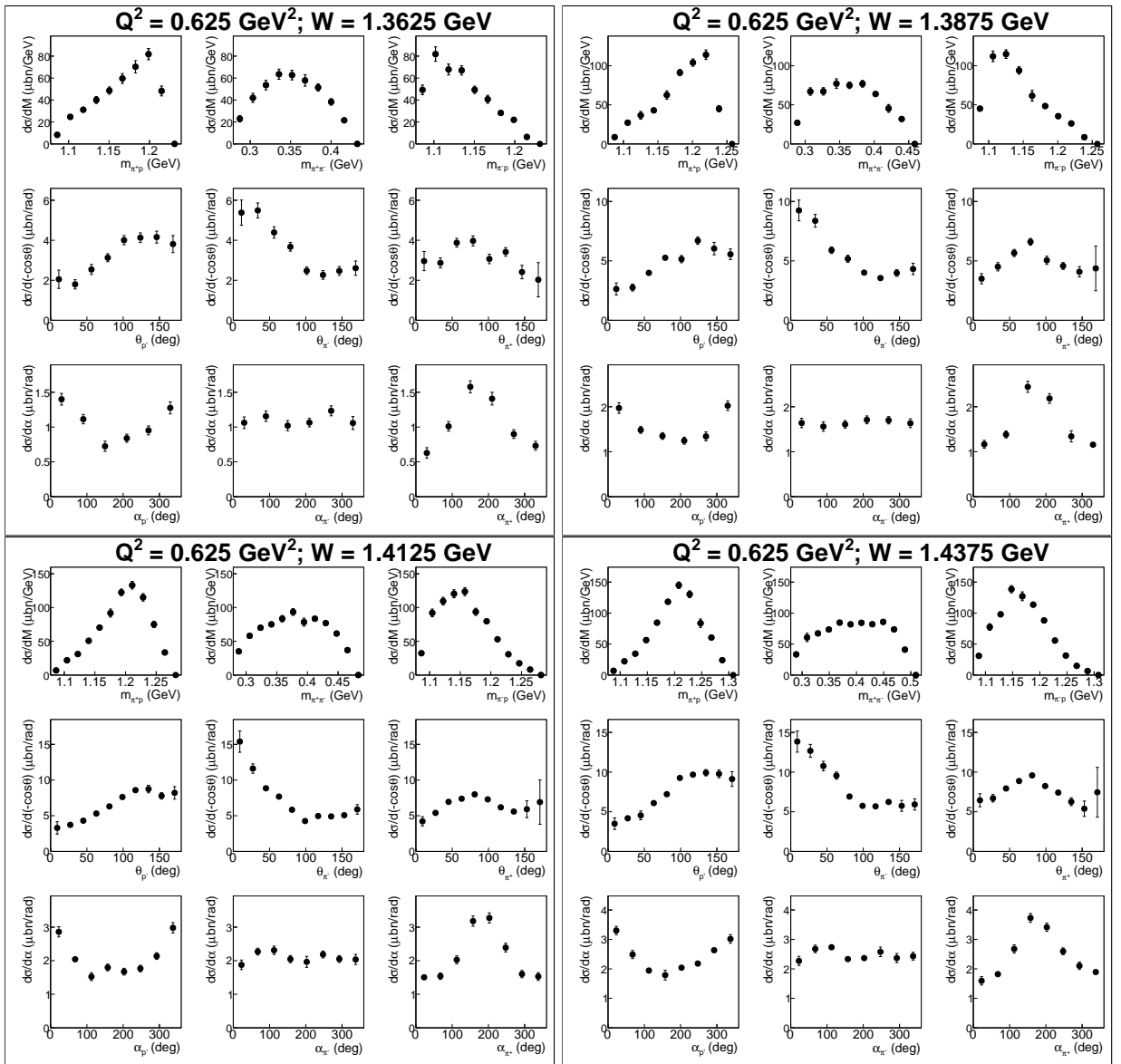


Figure A.19:

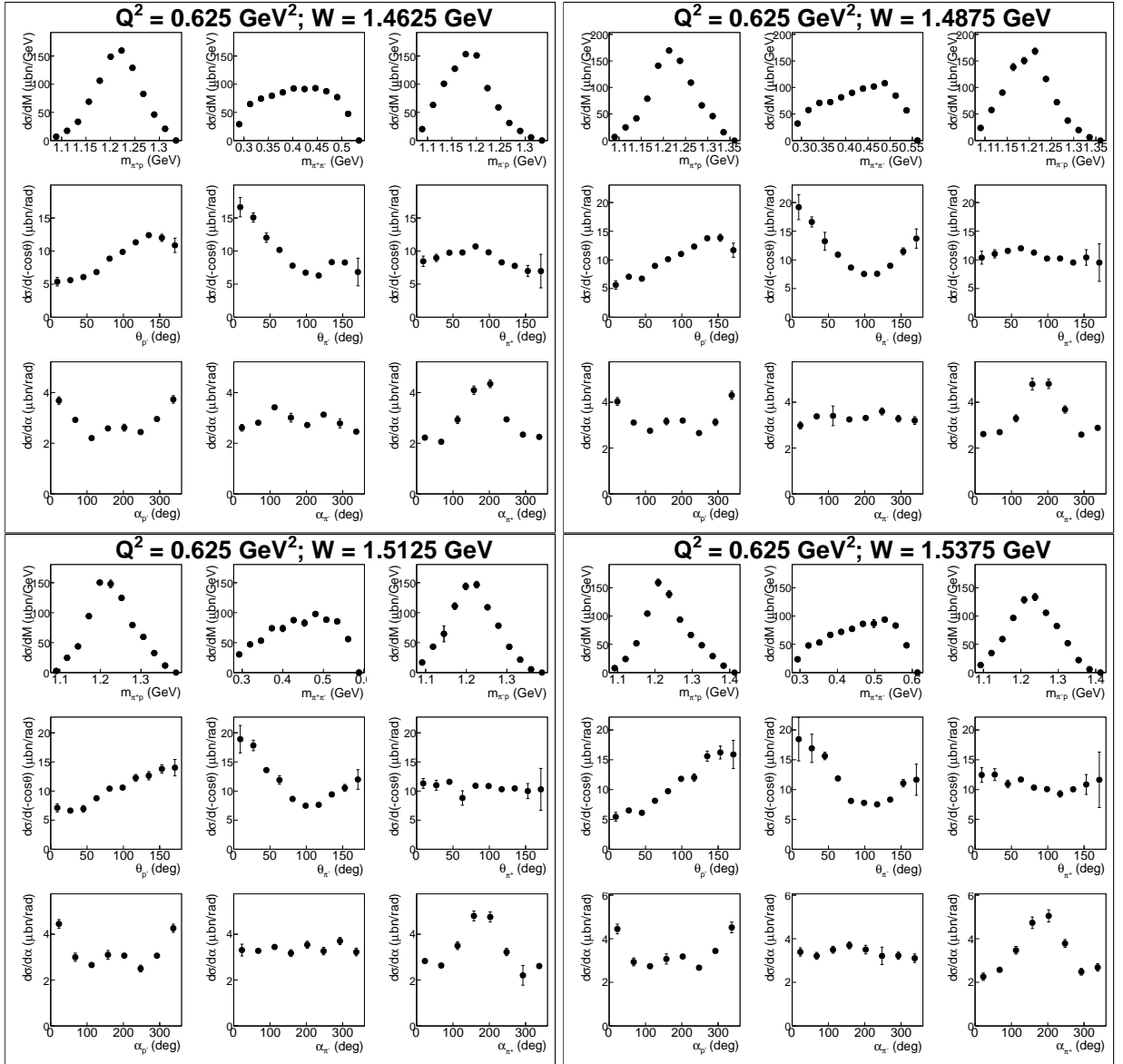


Figure A.20:

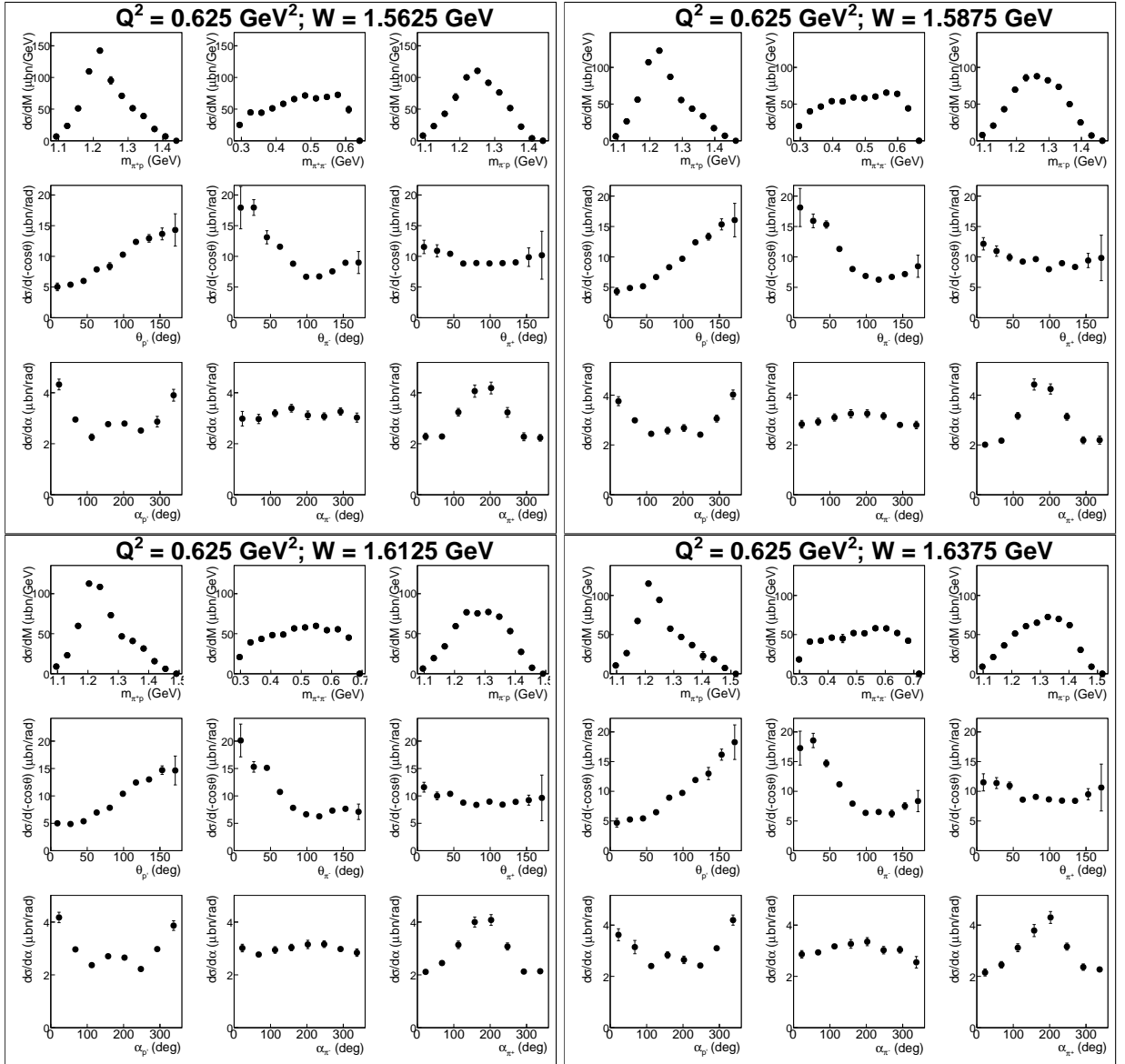


Figure A.21:

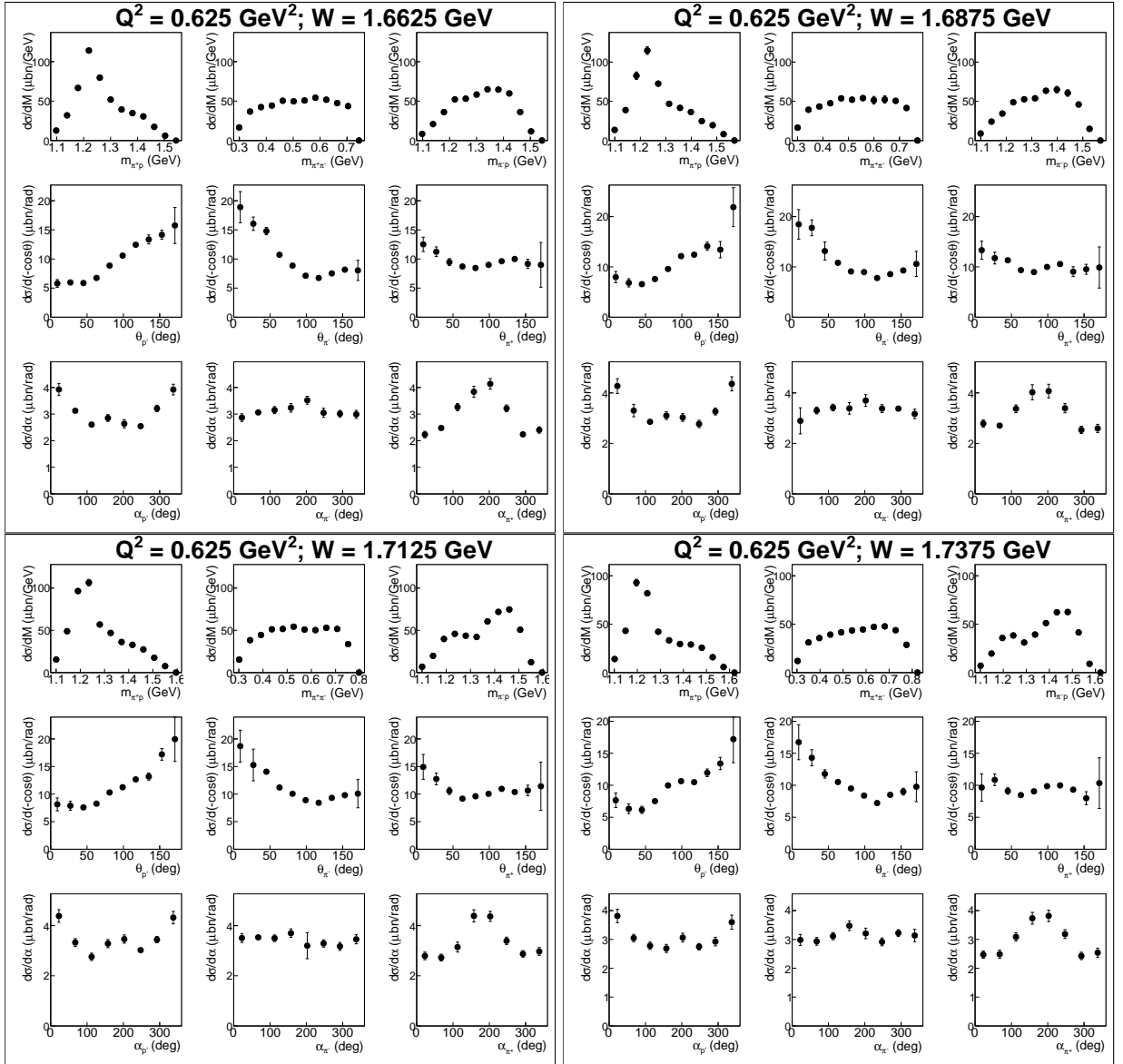


Figure A.22:

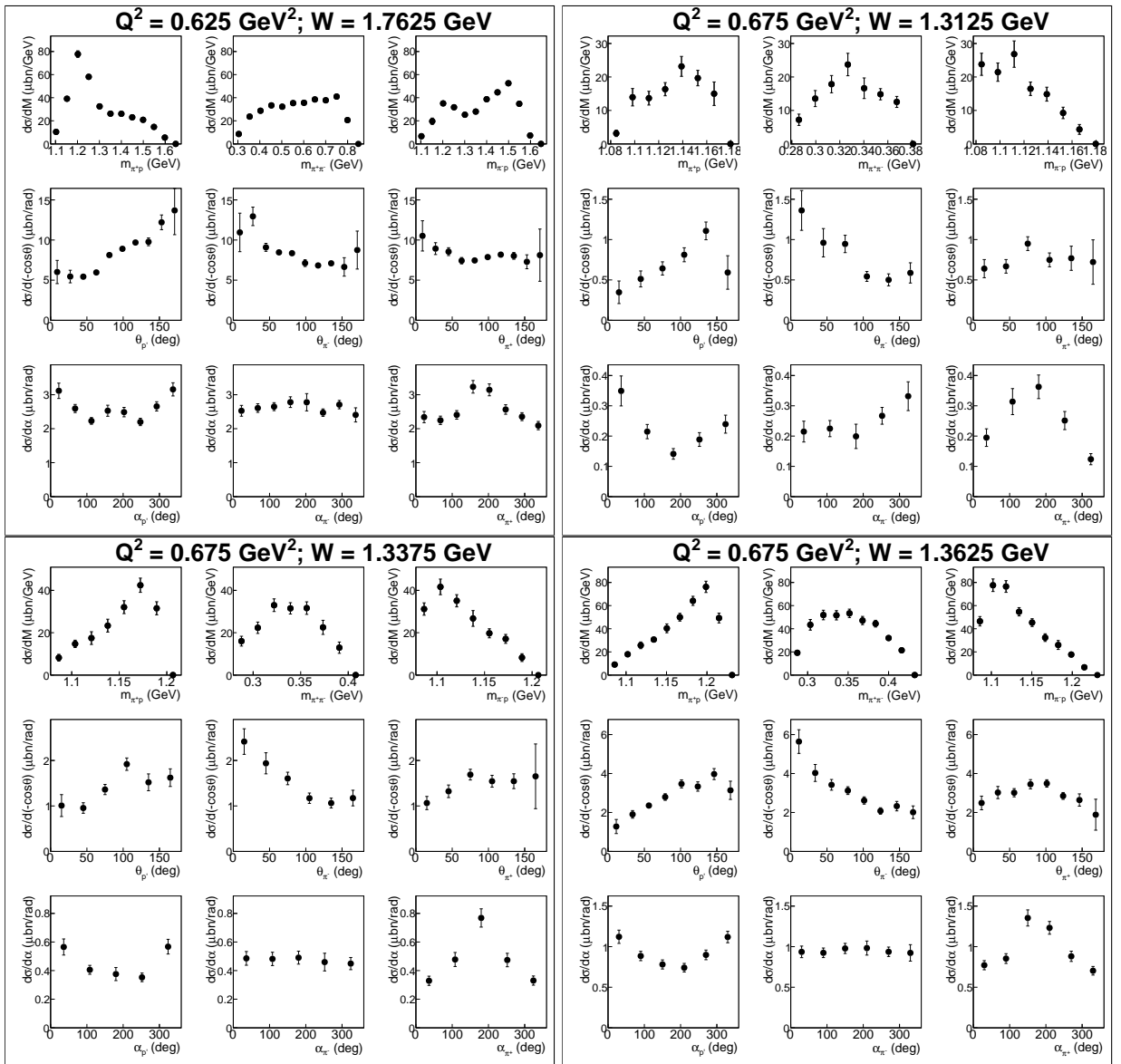


Figure A.23:

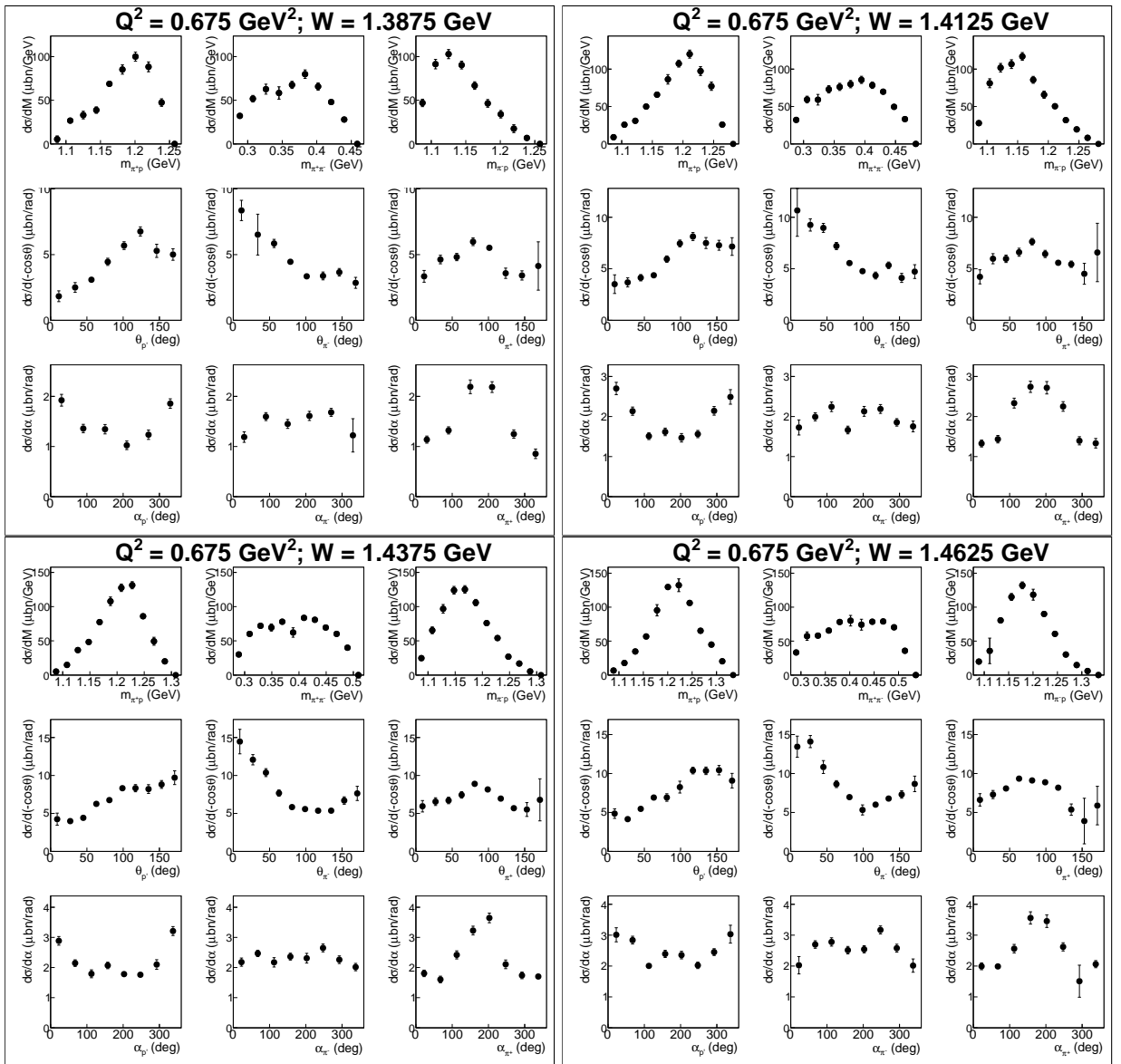


Figure A.24:

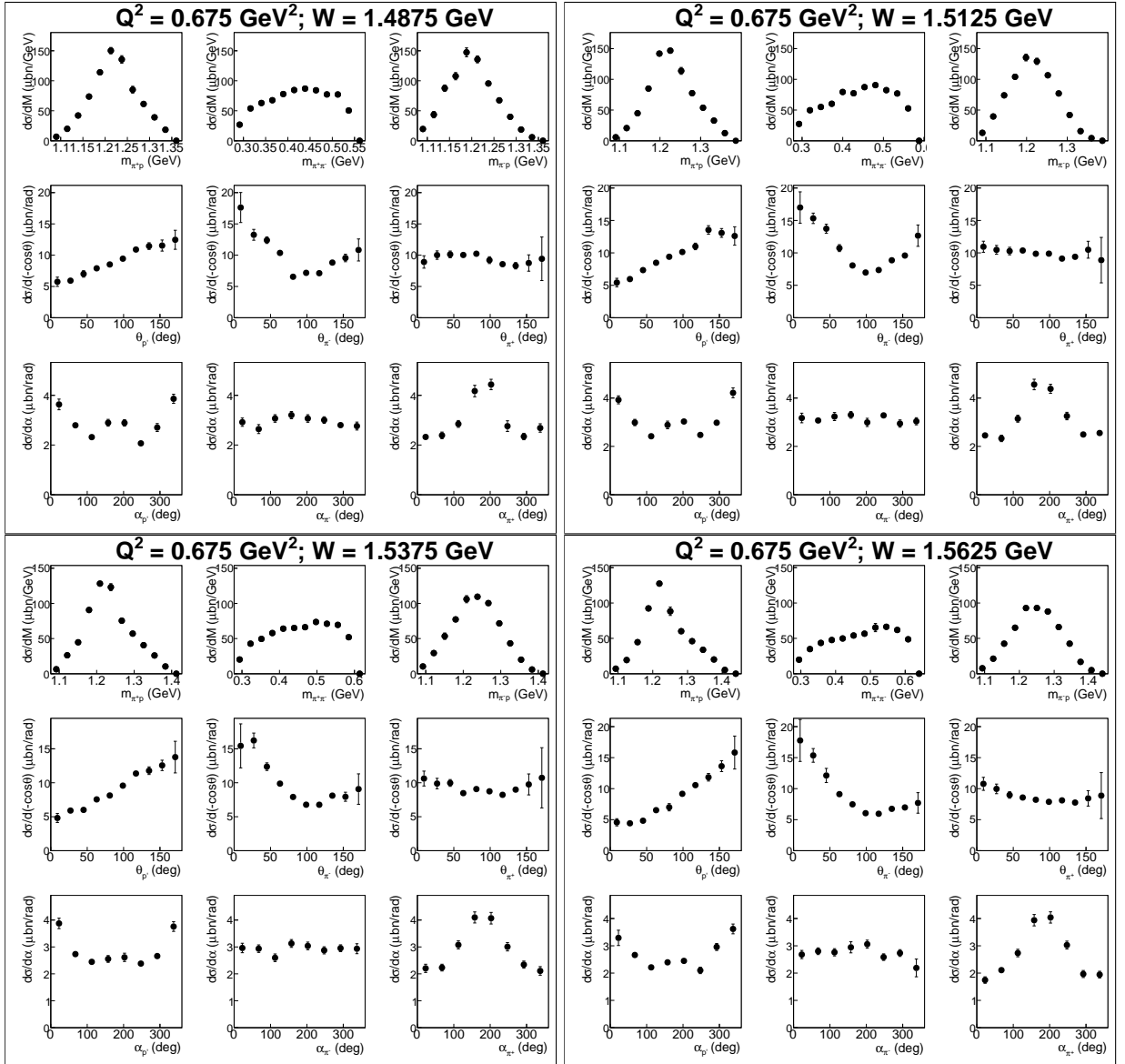


Figure A.25:

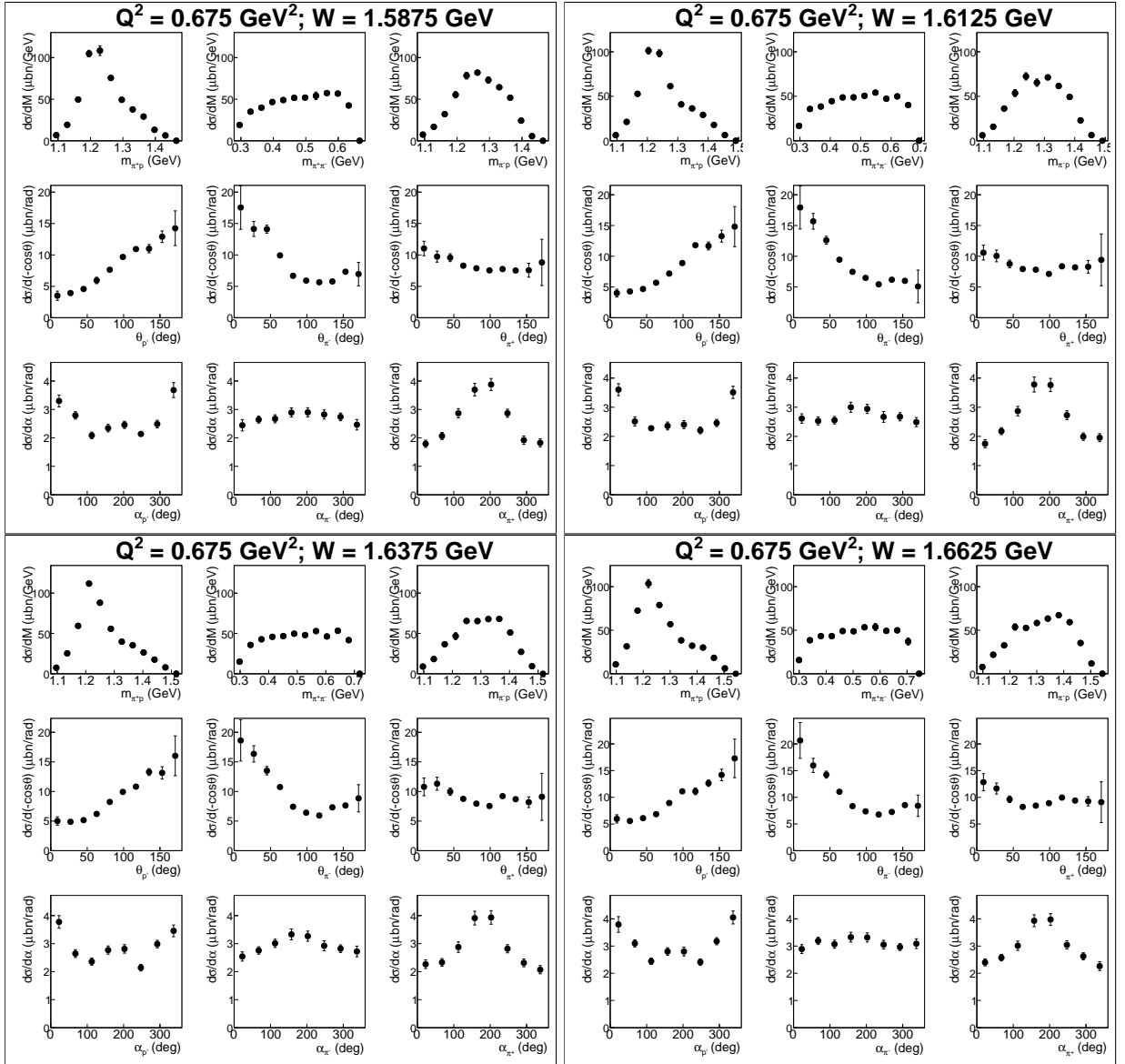


Figure A.26:

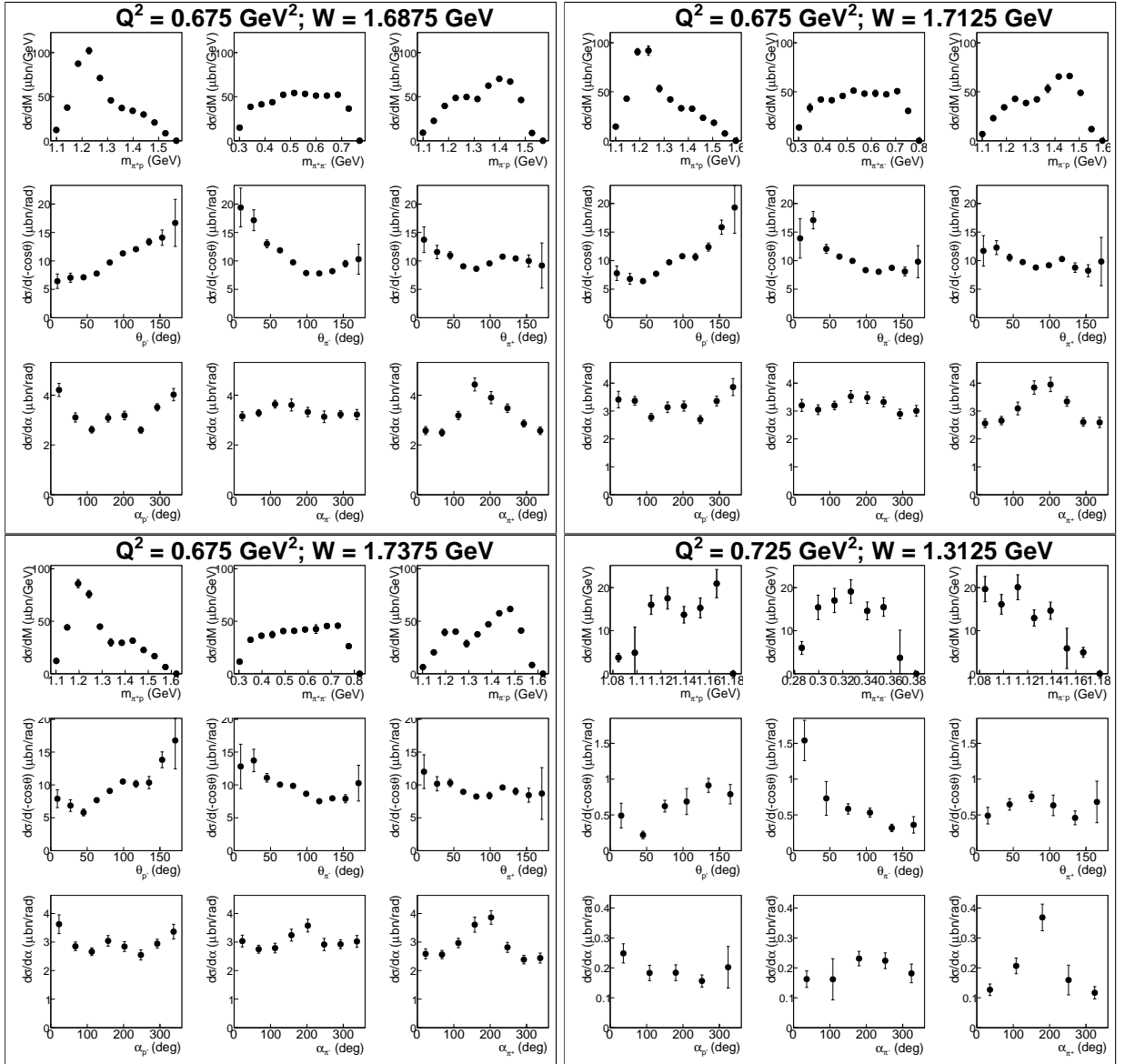


Figure A.27:

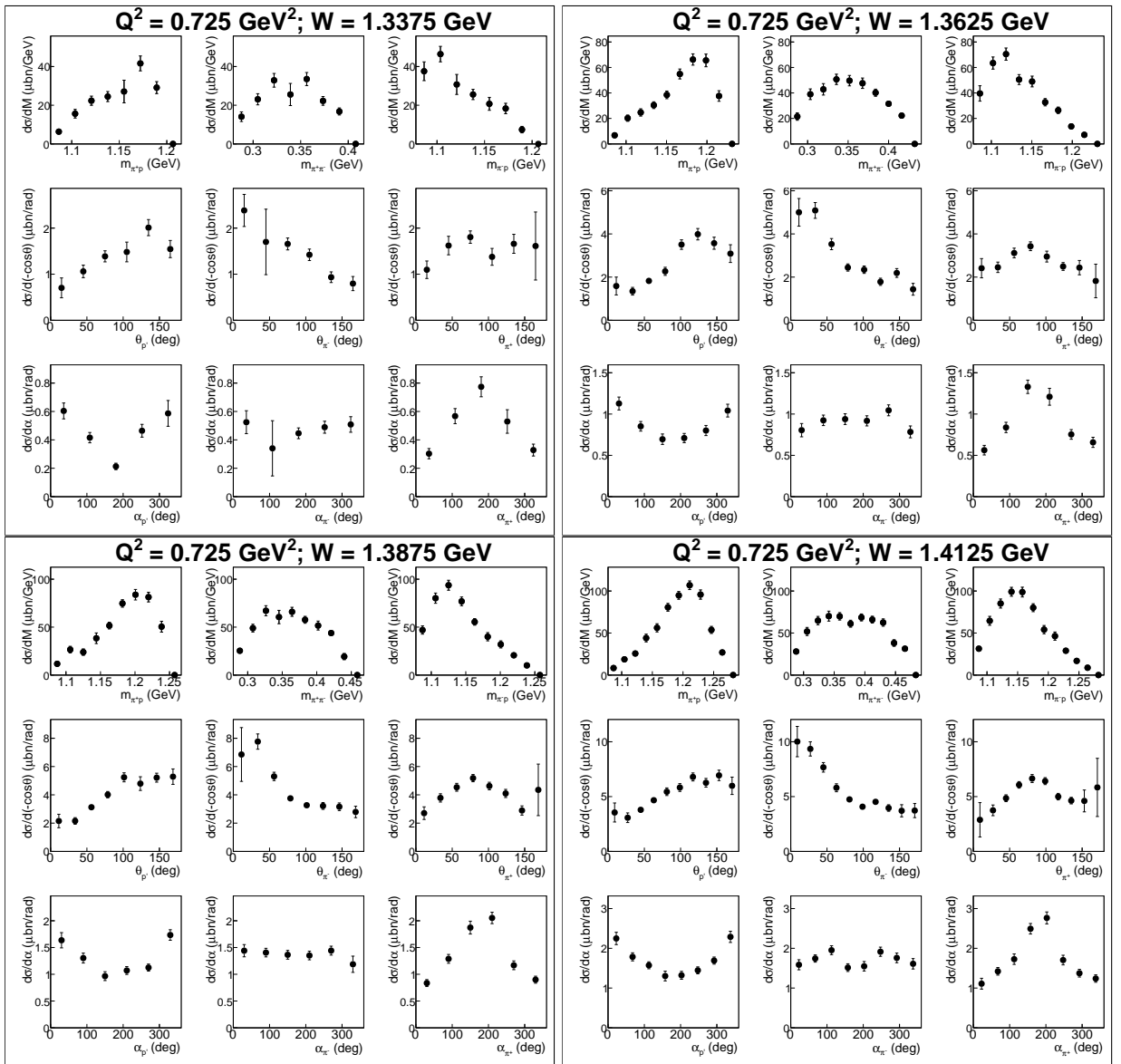


Figure A.28:

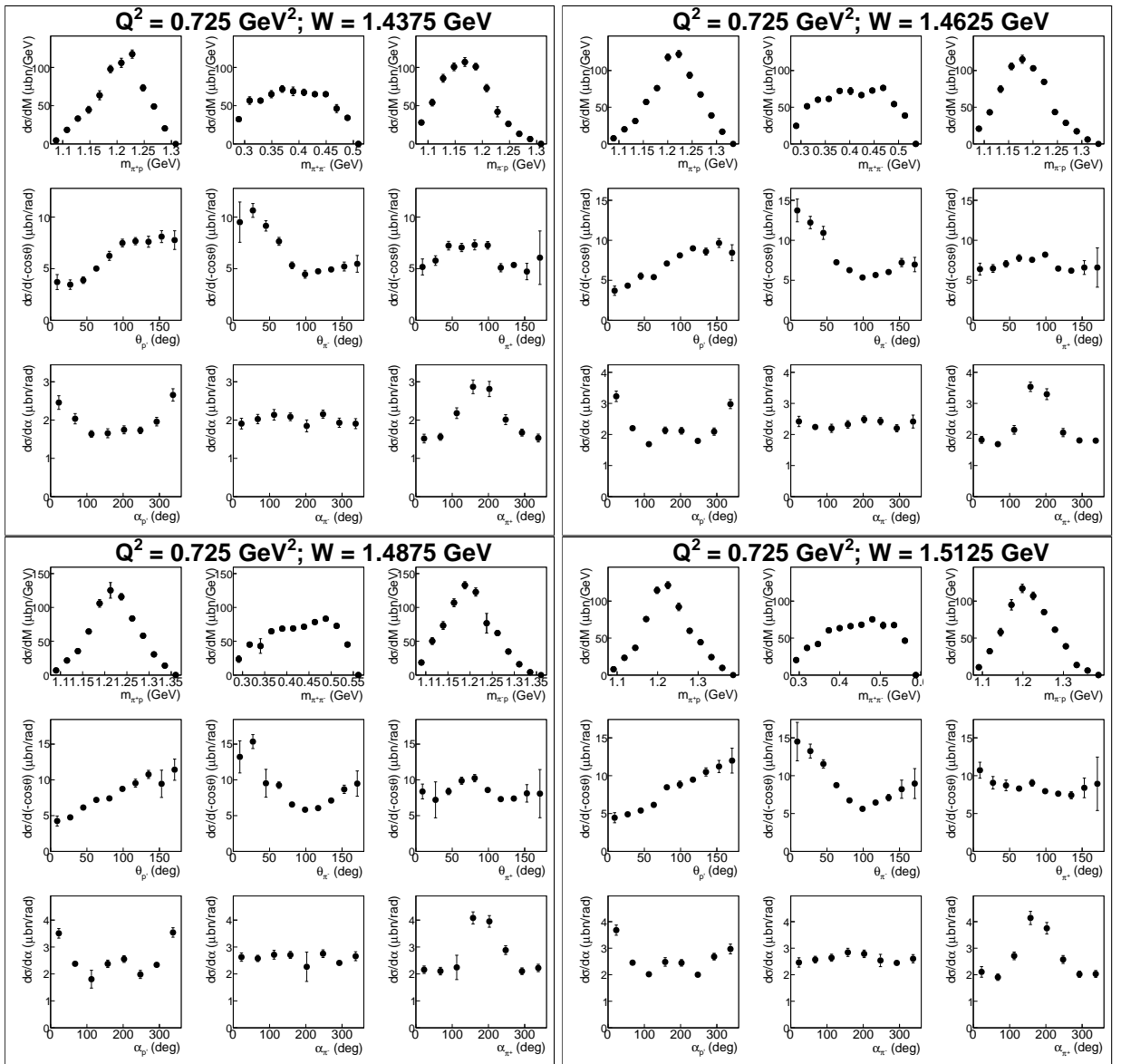


Figure A.29:

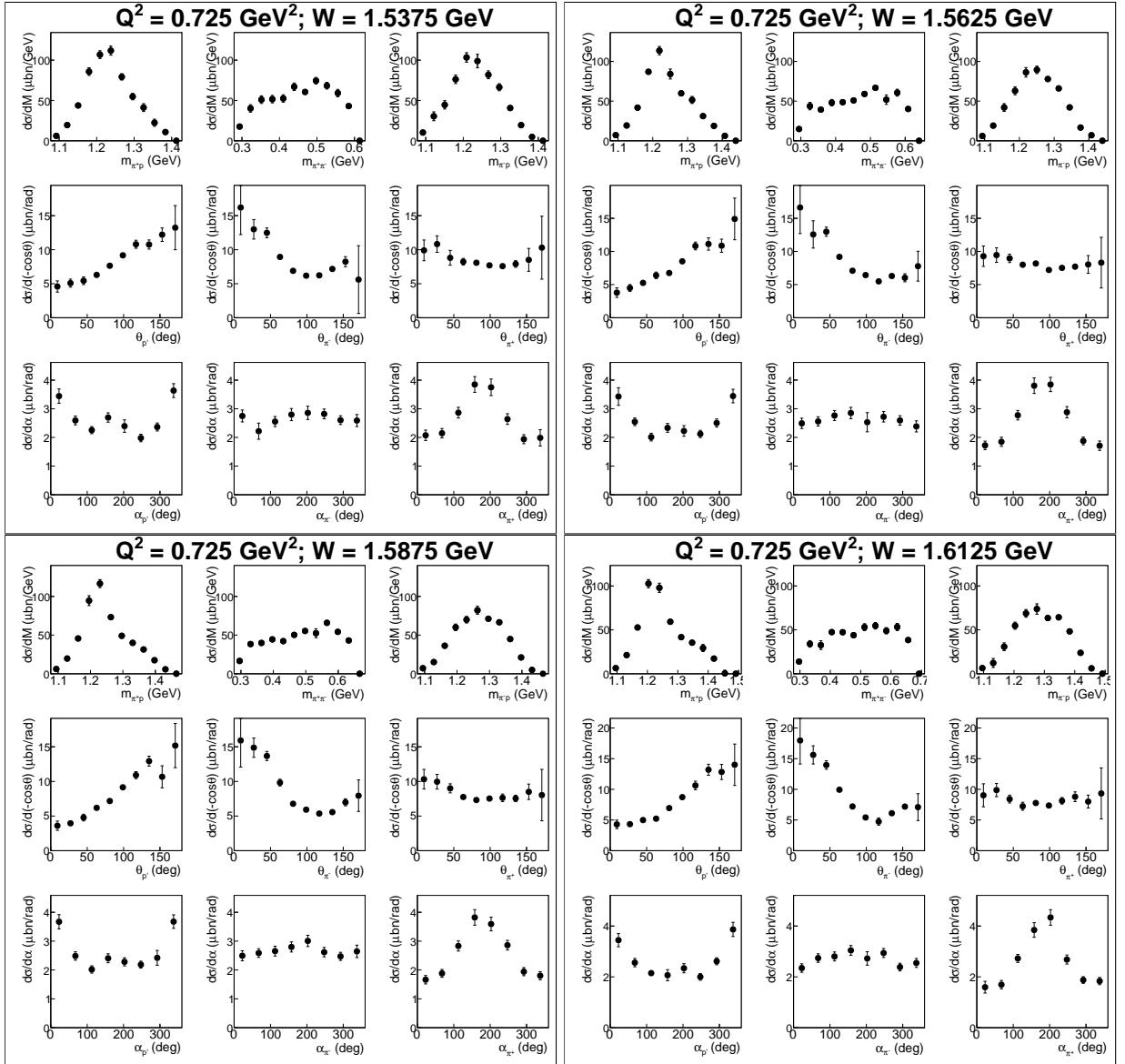


Figure A.30:

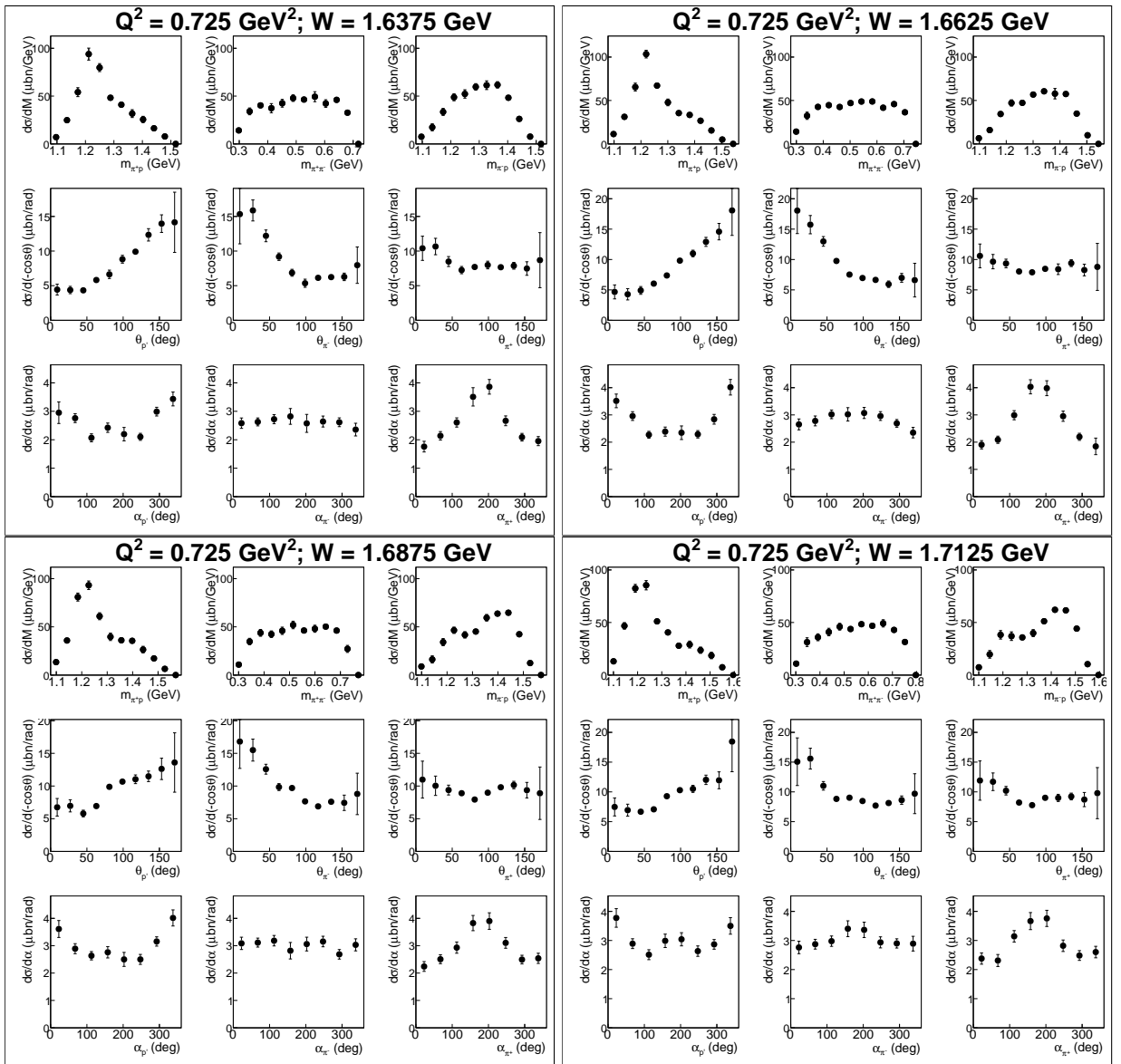


Figure A.31:

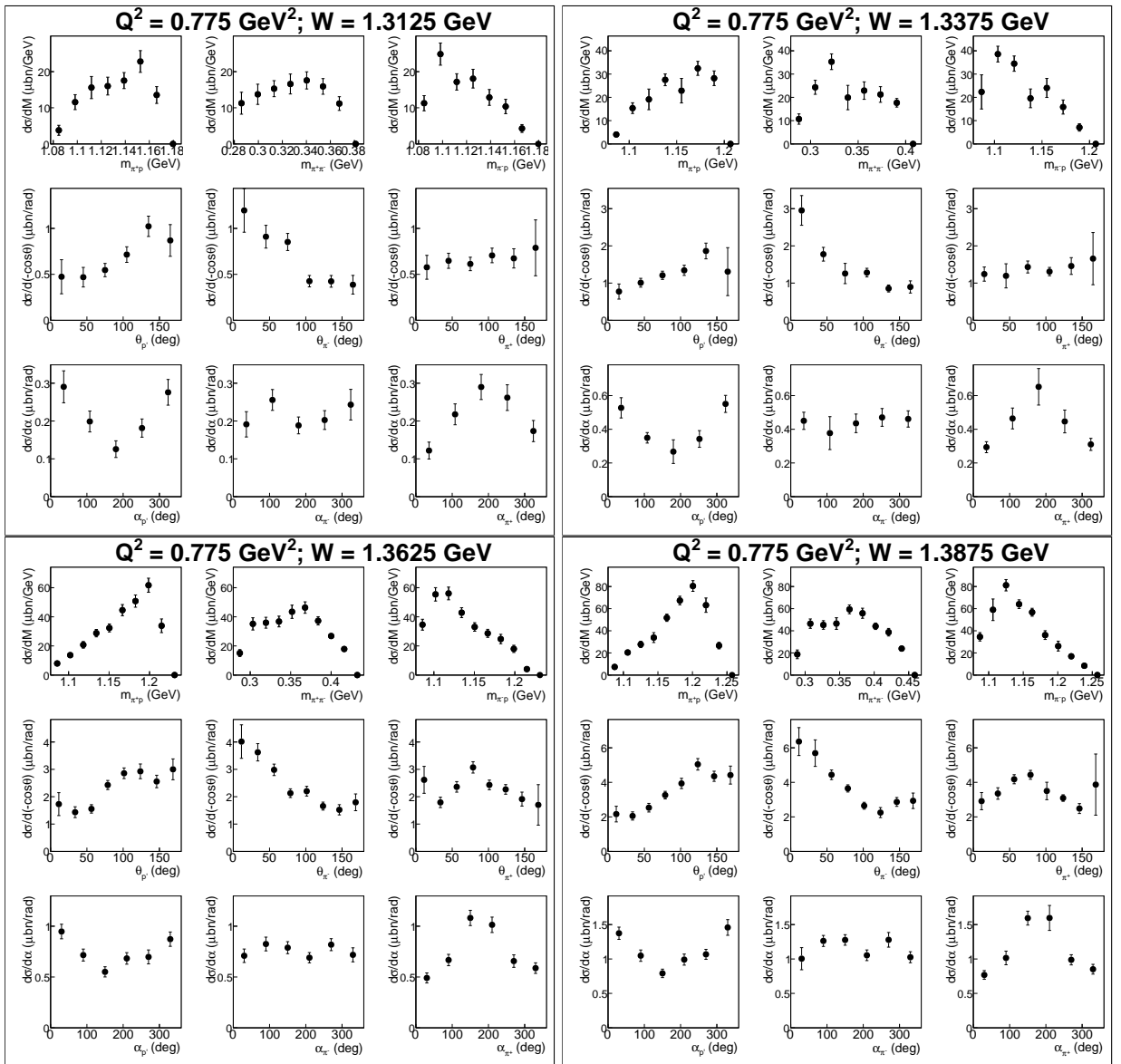


Figure A.32:

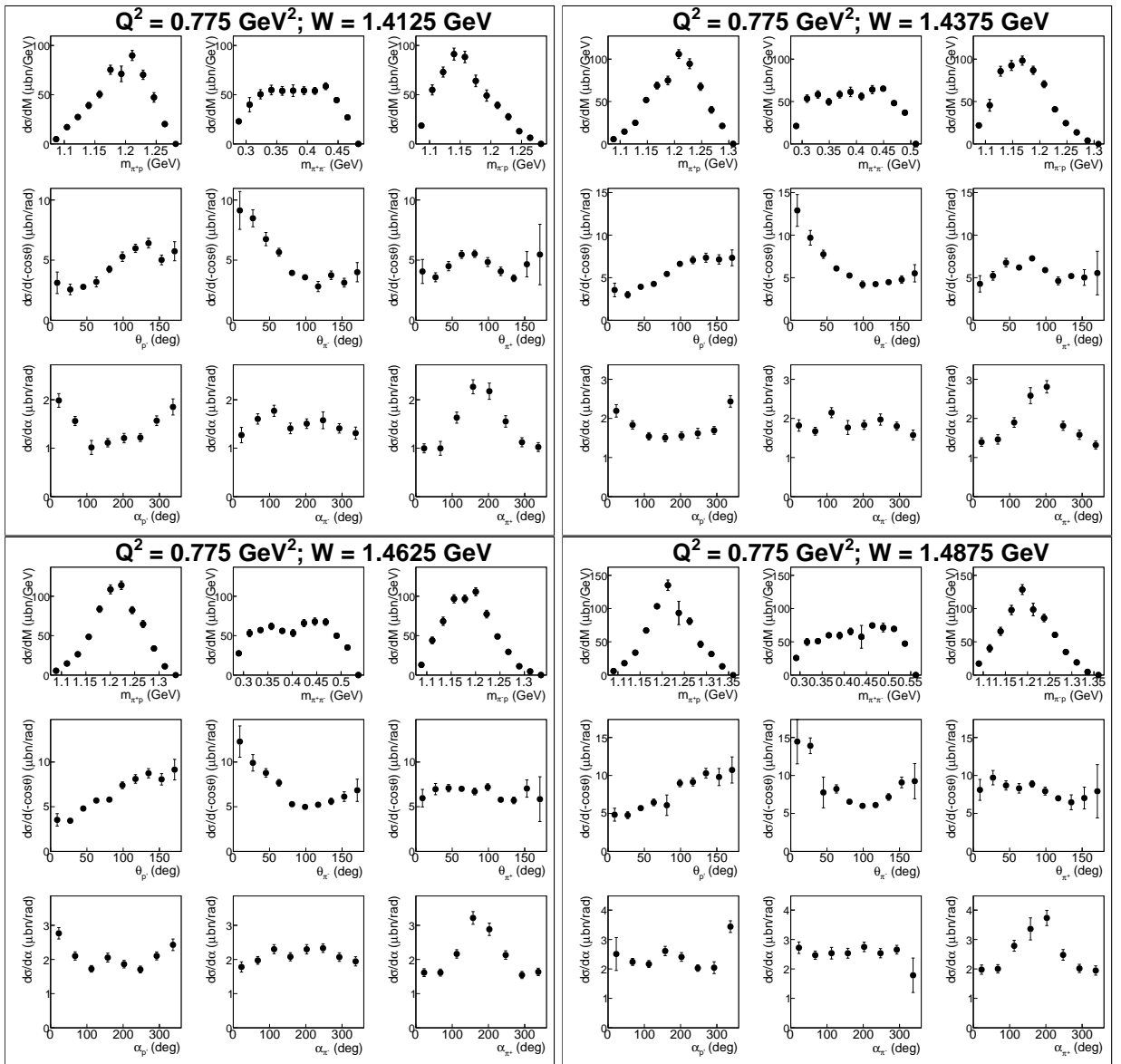


Figure A.33:

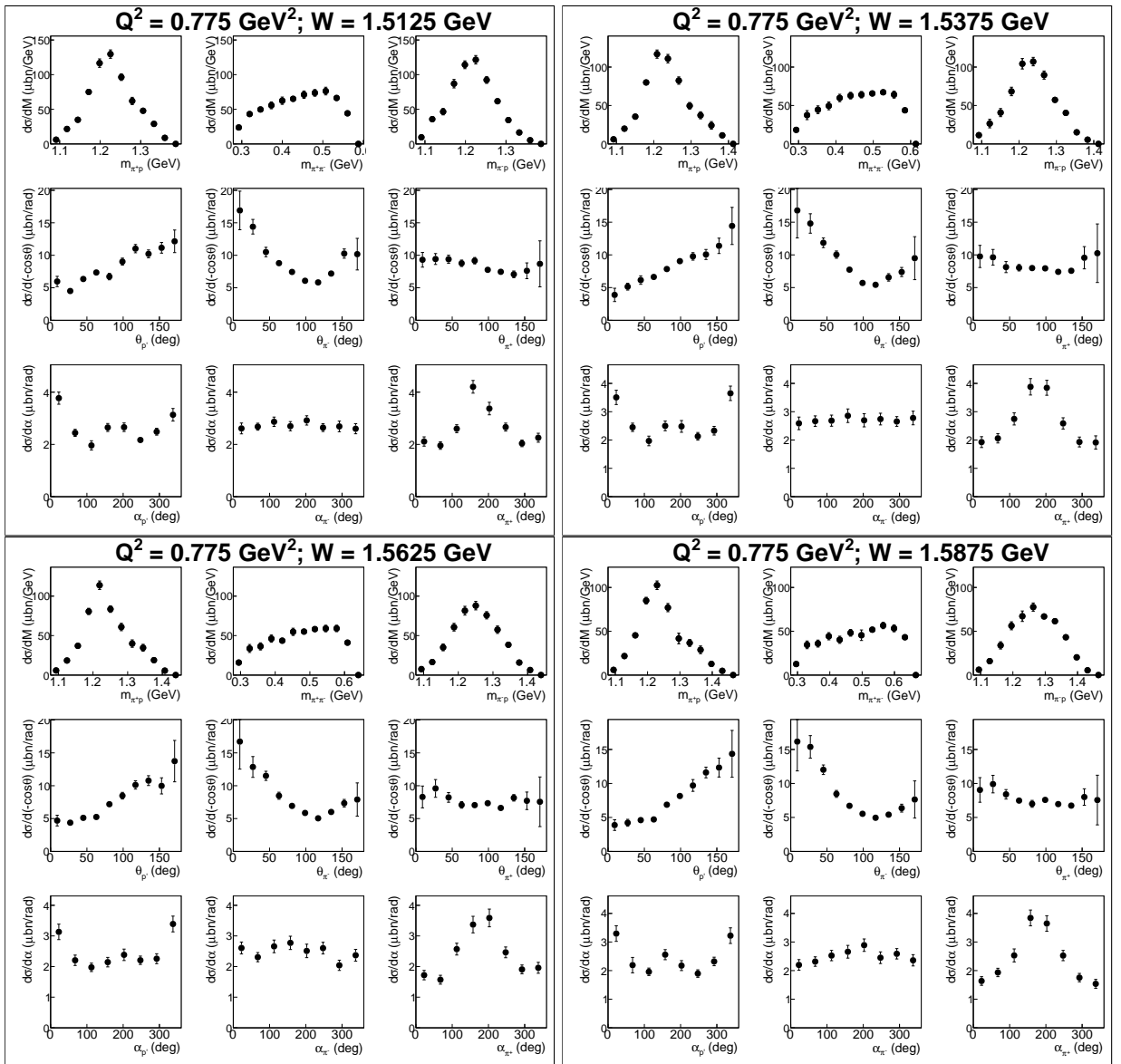


Figure A.34:

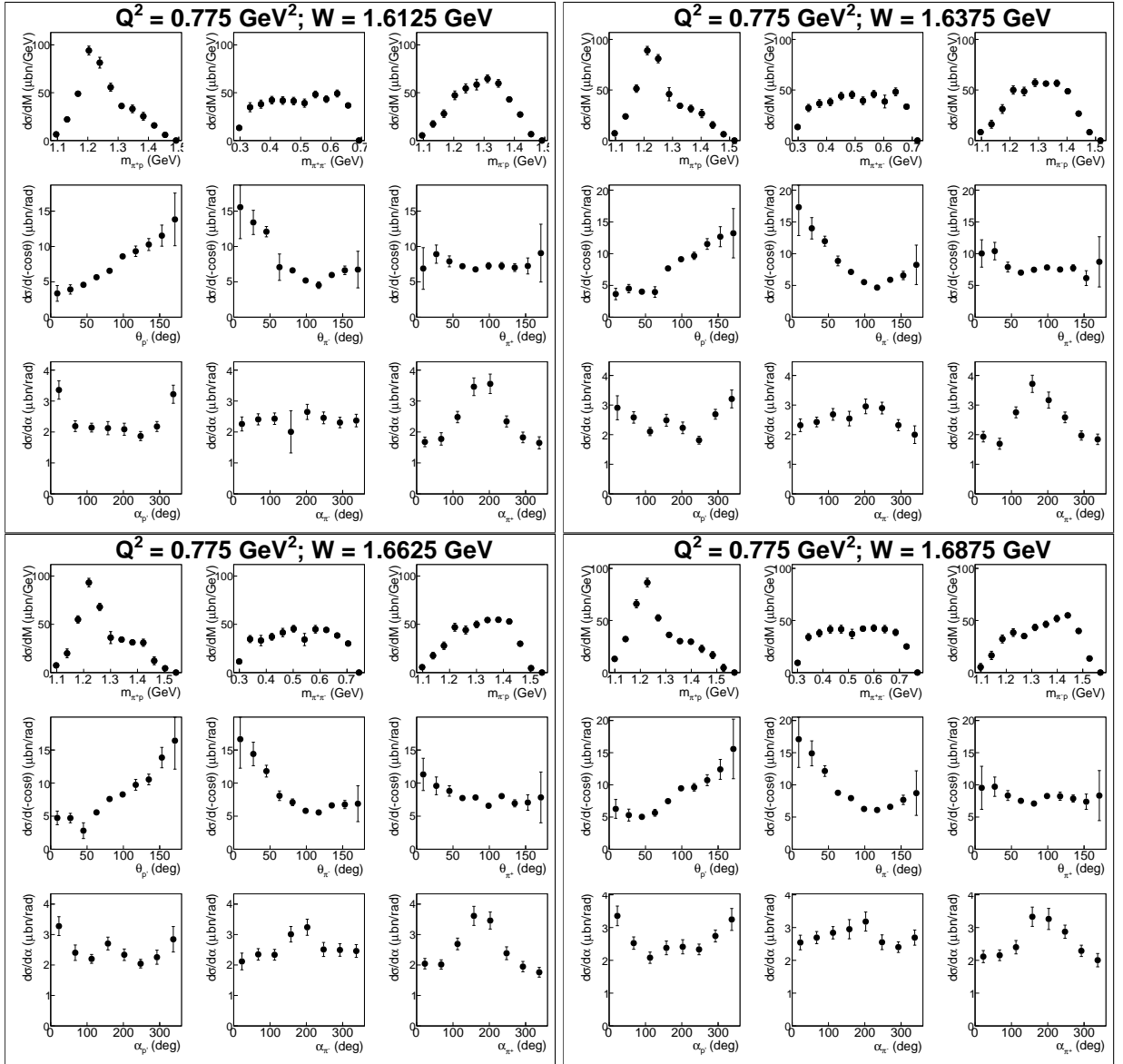


Figure A.35:

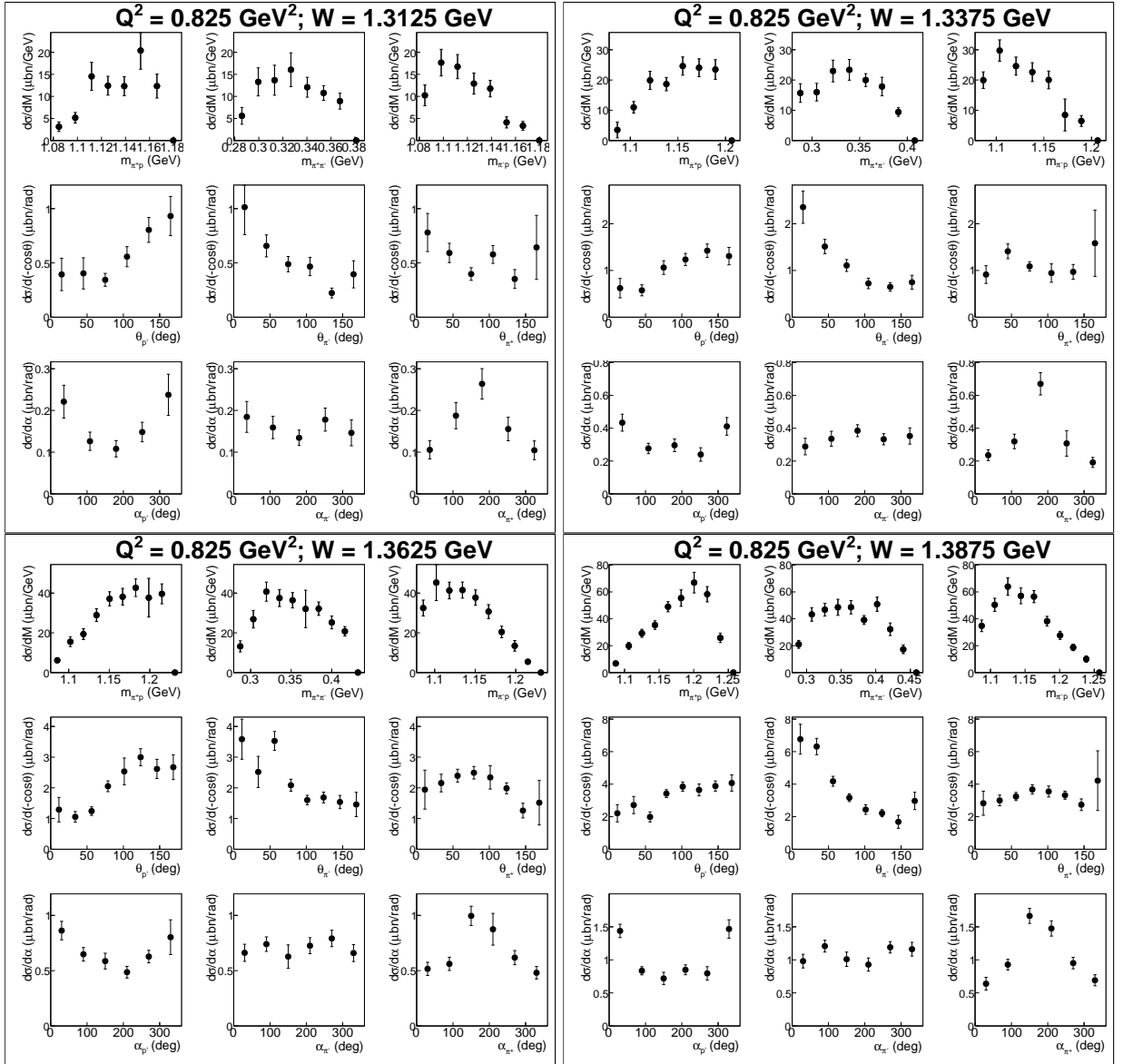


Figure A.36:

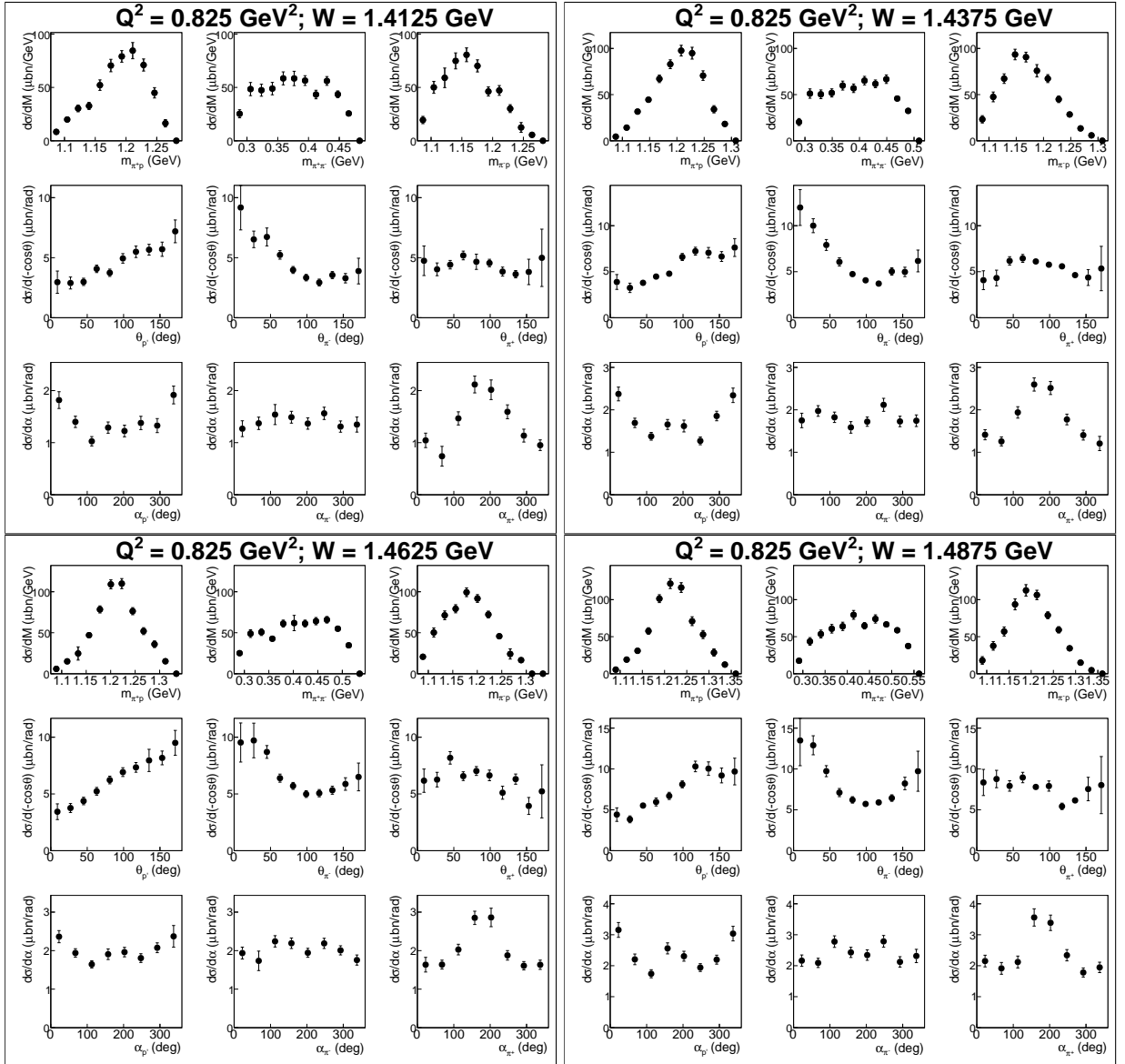


Figure A.37:

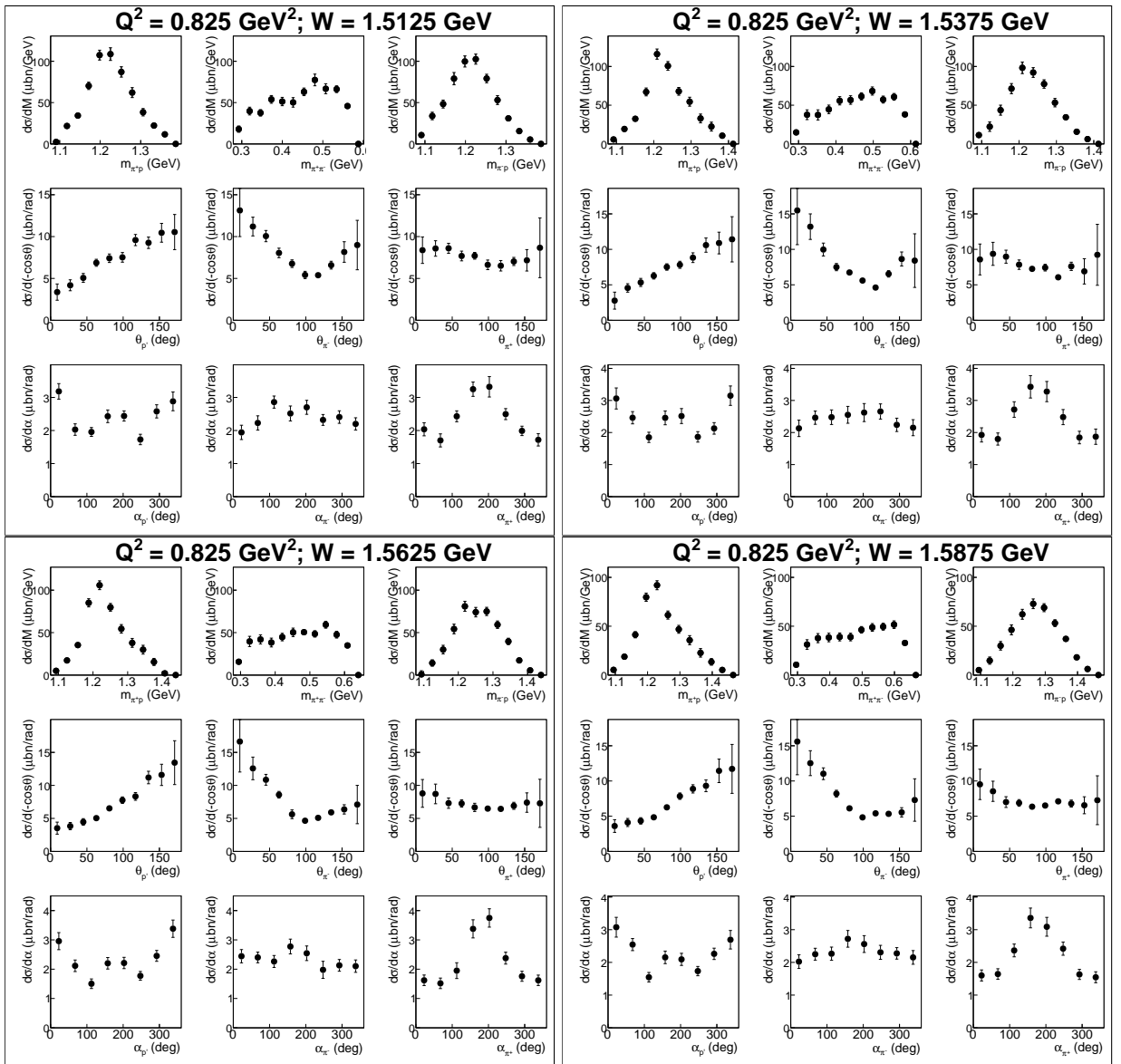


Figure A.38:

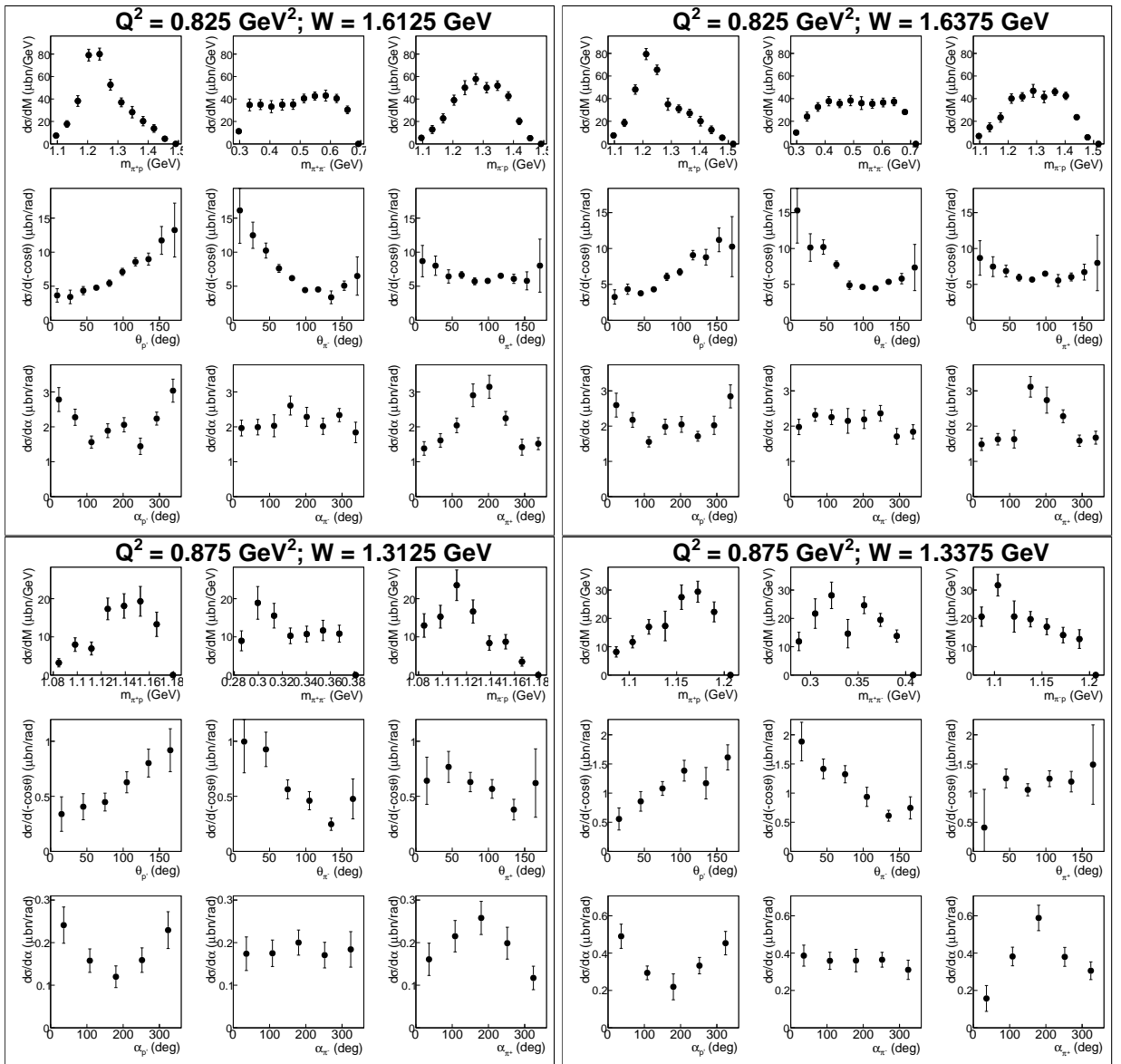


Figure A.39:

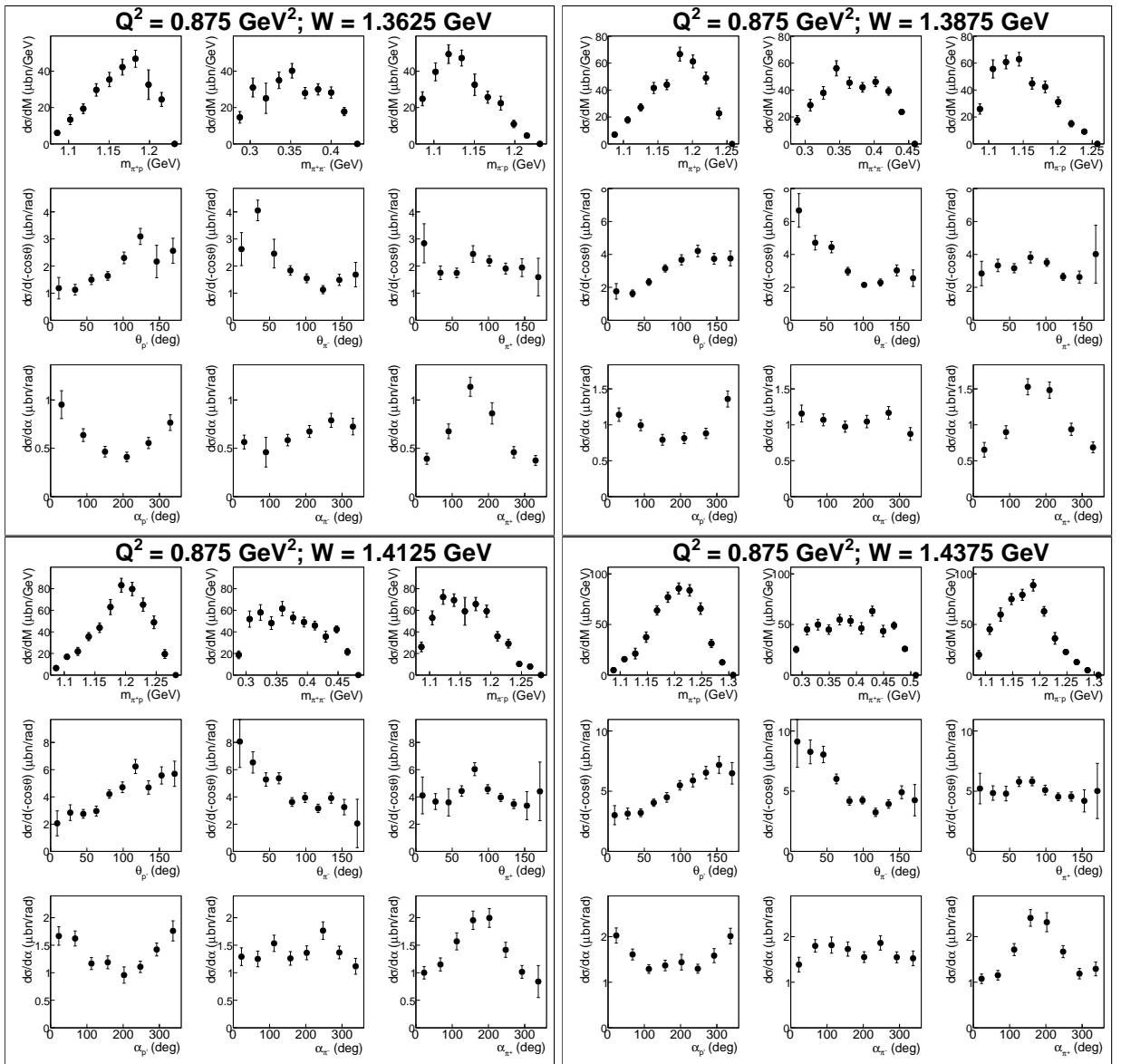


Figure A.40:

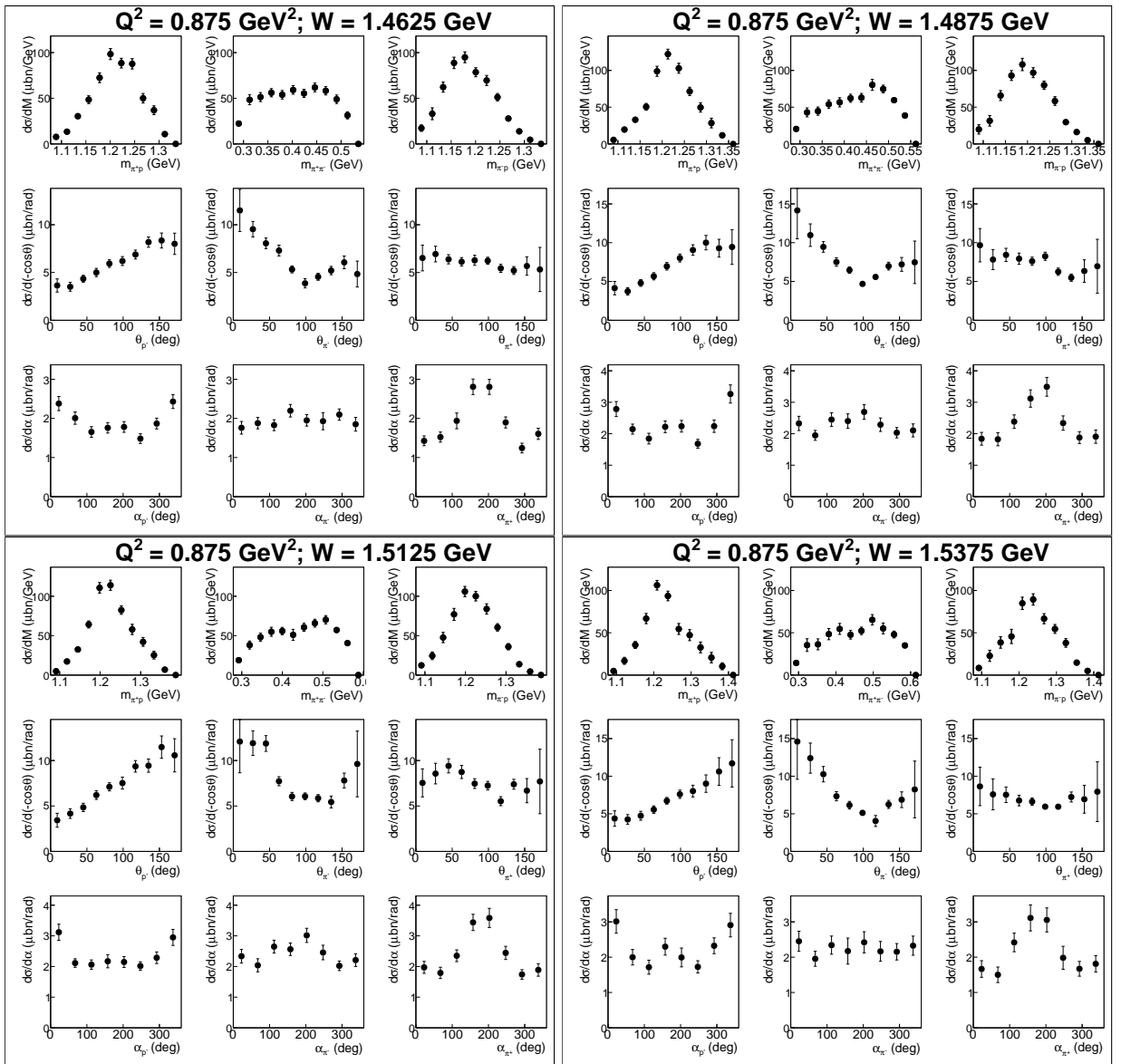


Figure A.41:

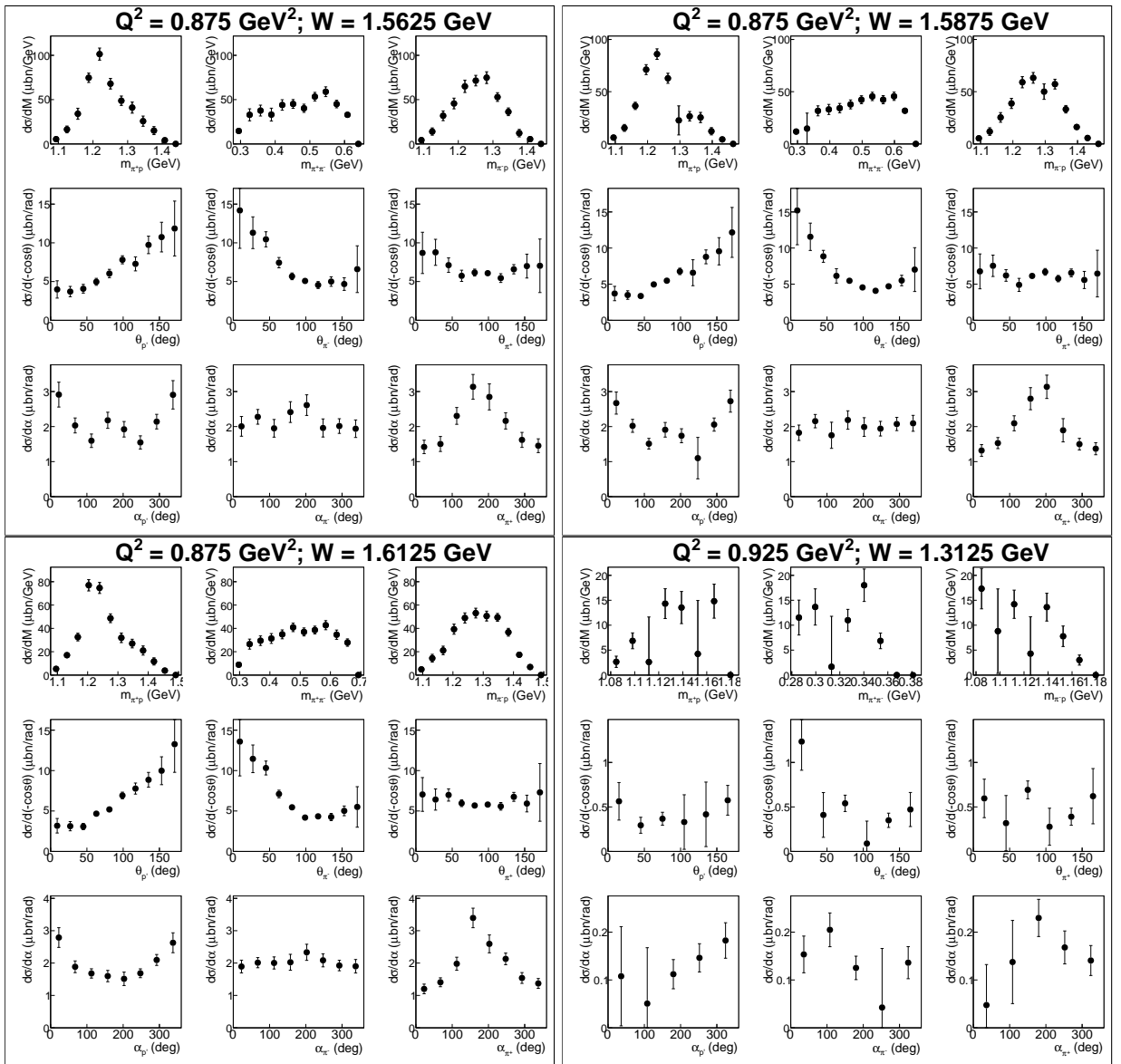


Figure A.42:

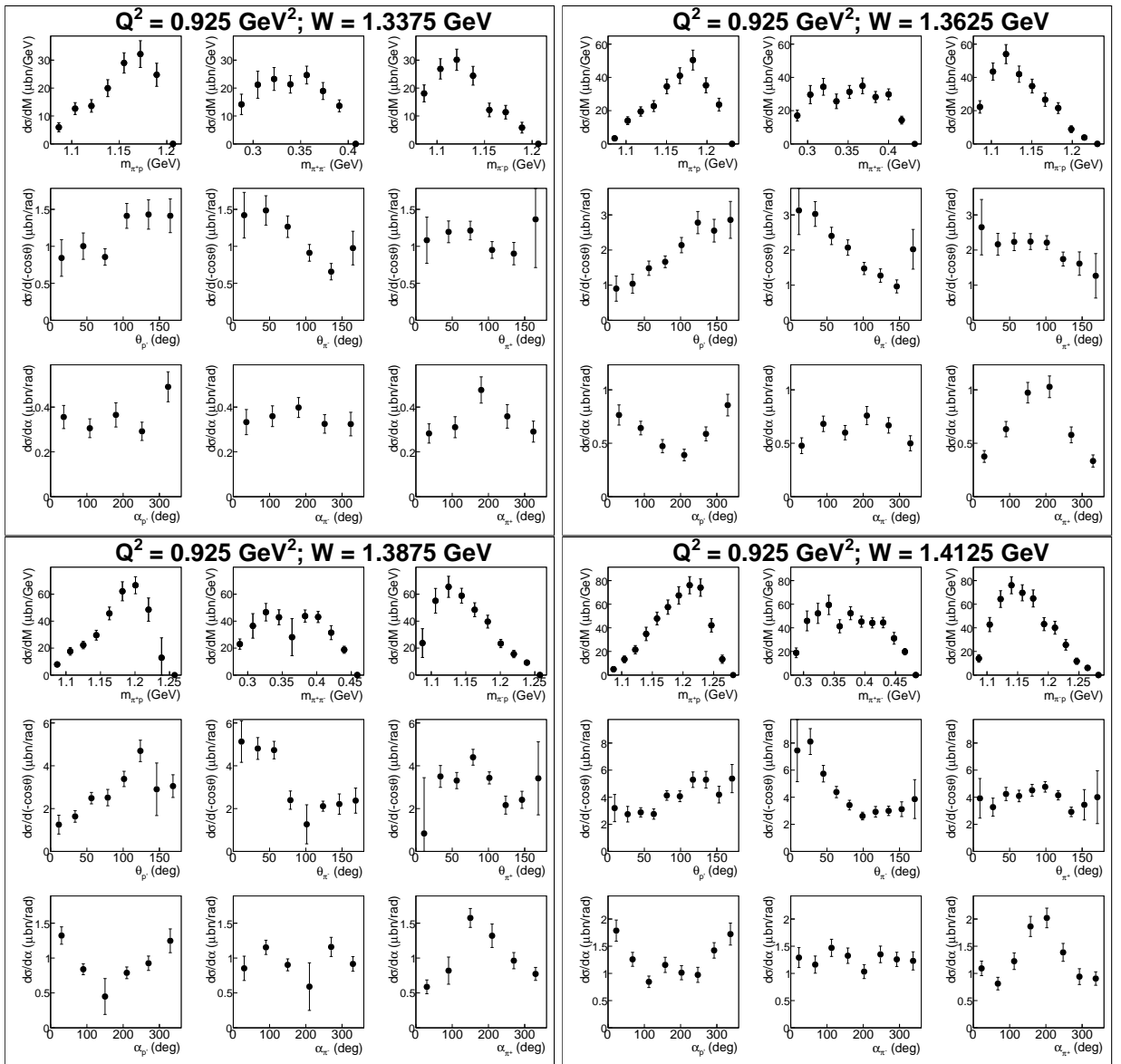


Figure A.43:

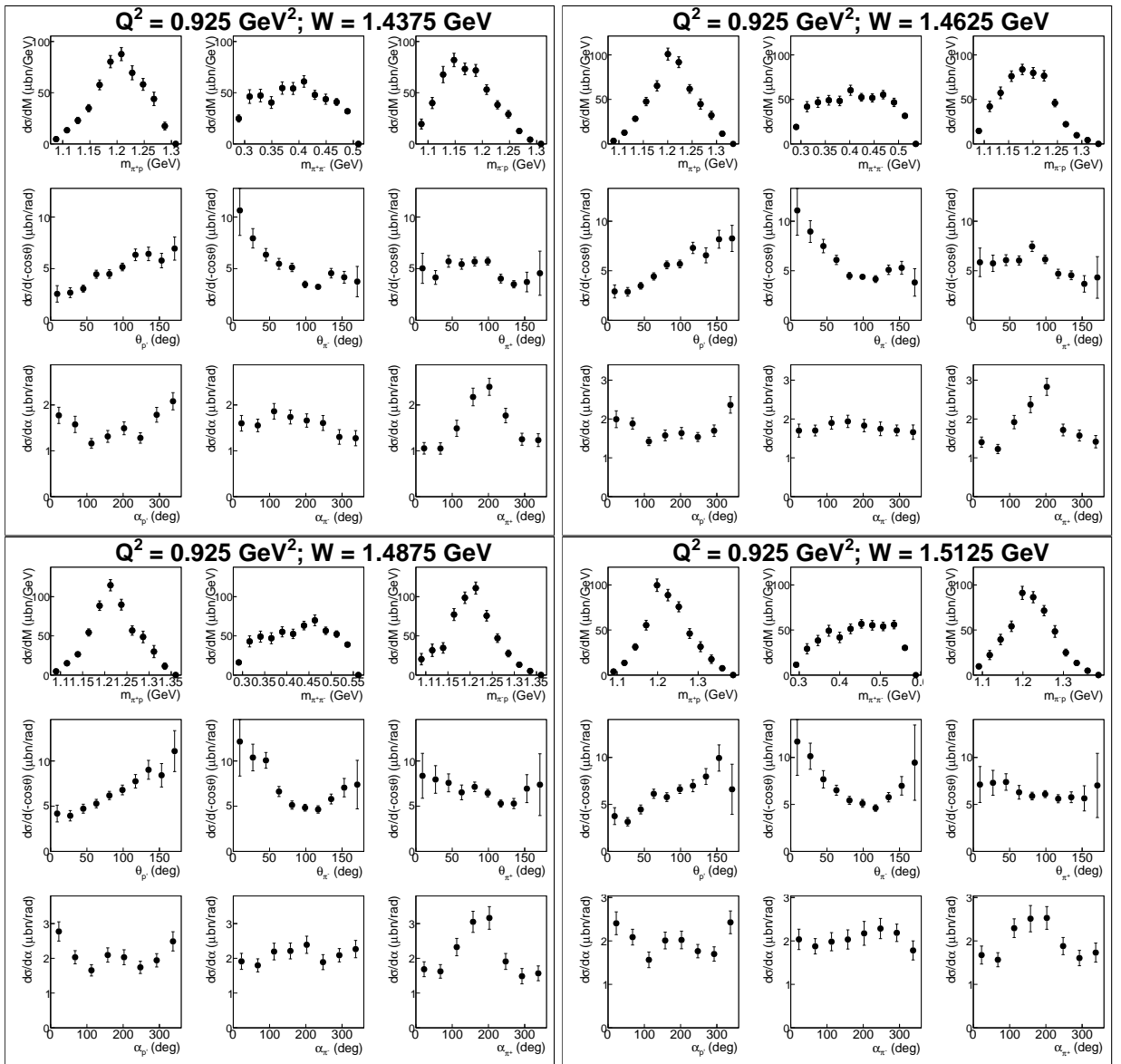


Figure A.44:

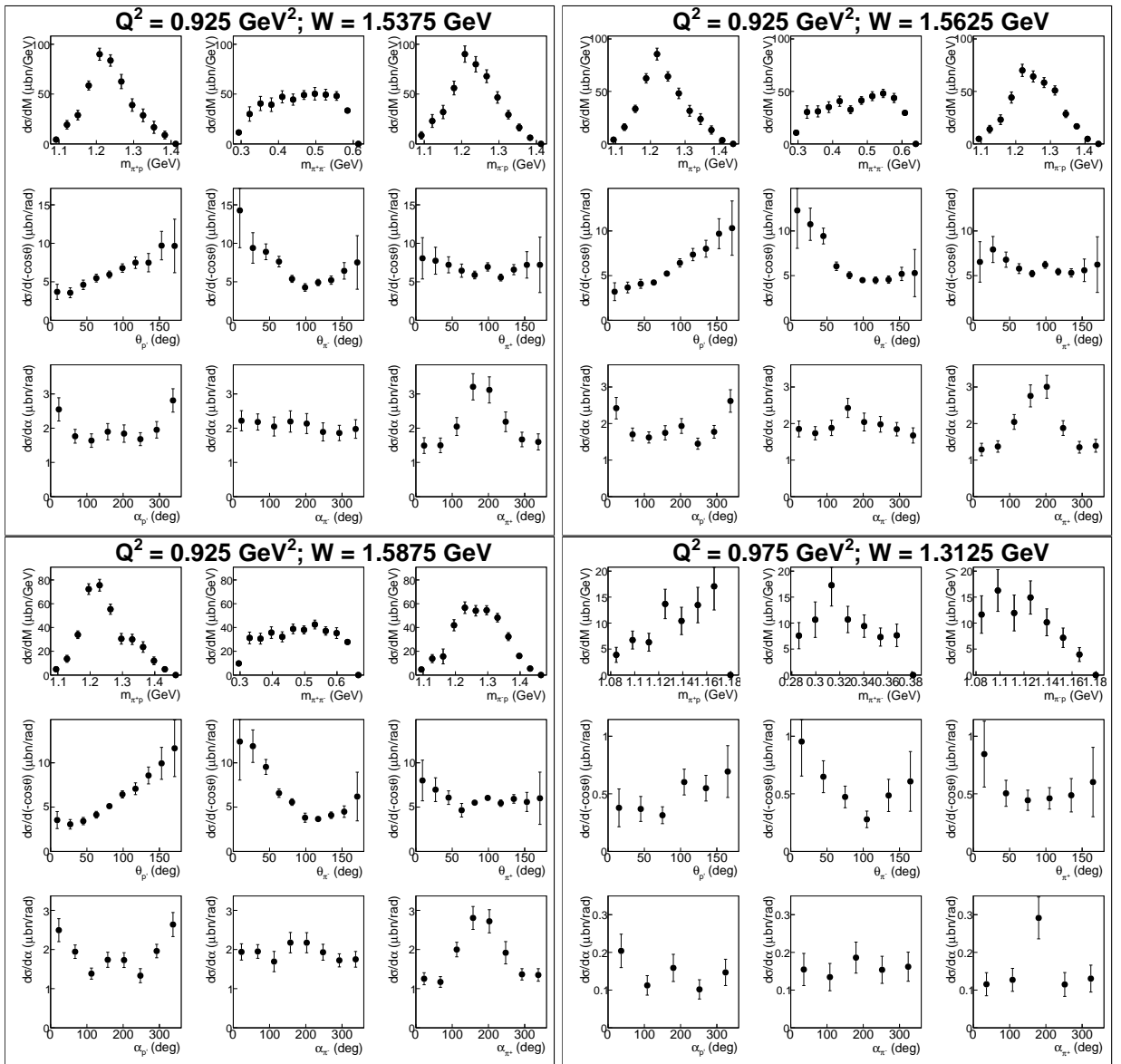


Figure A.45:

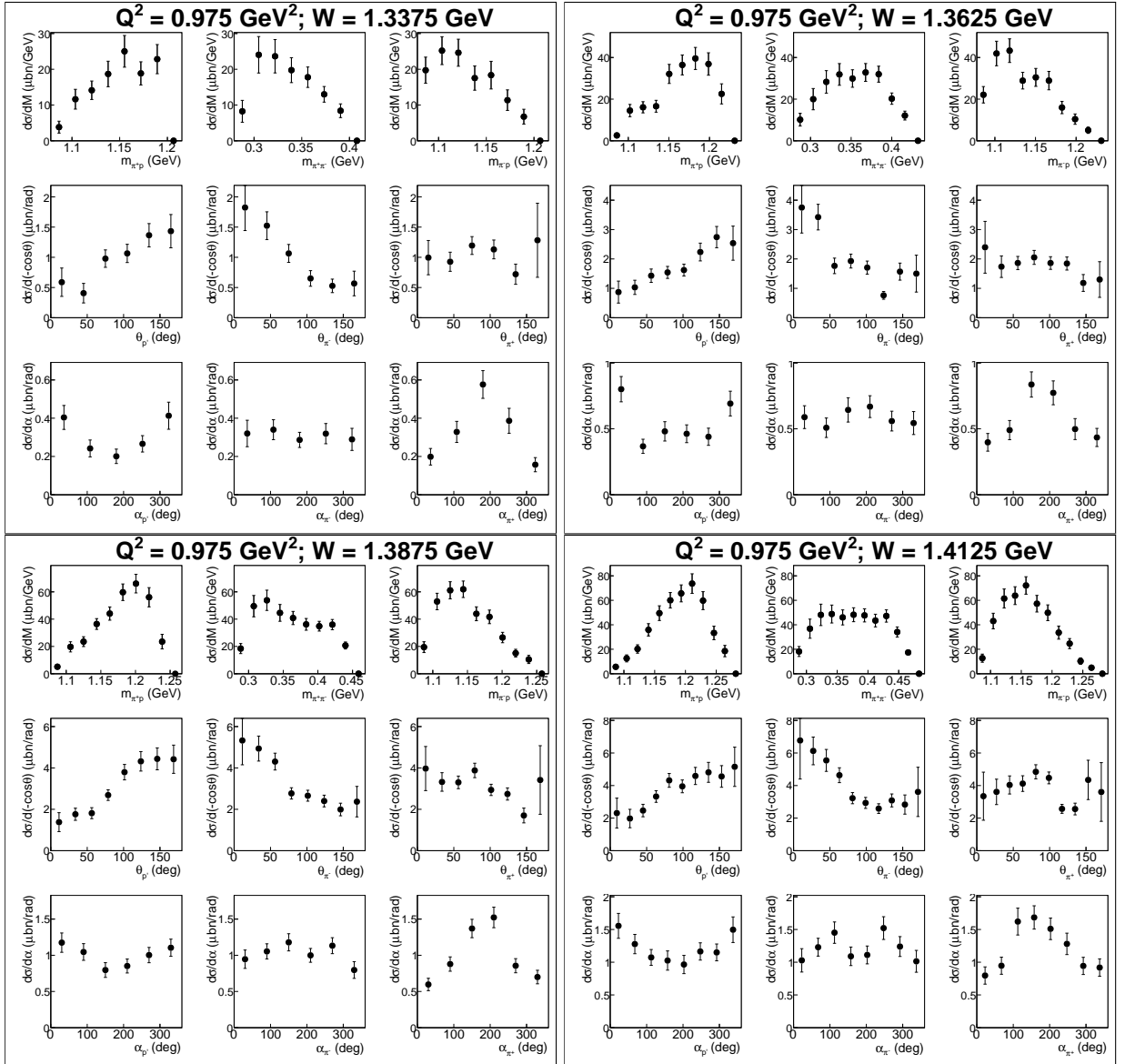


Figure A.46:

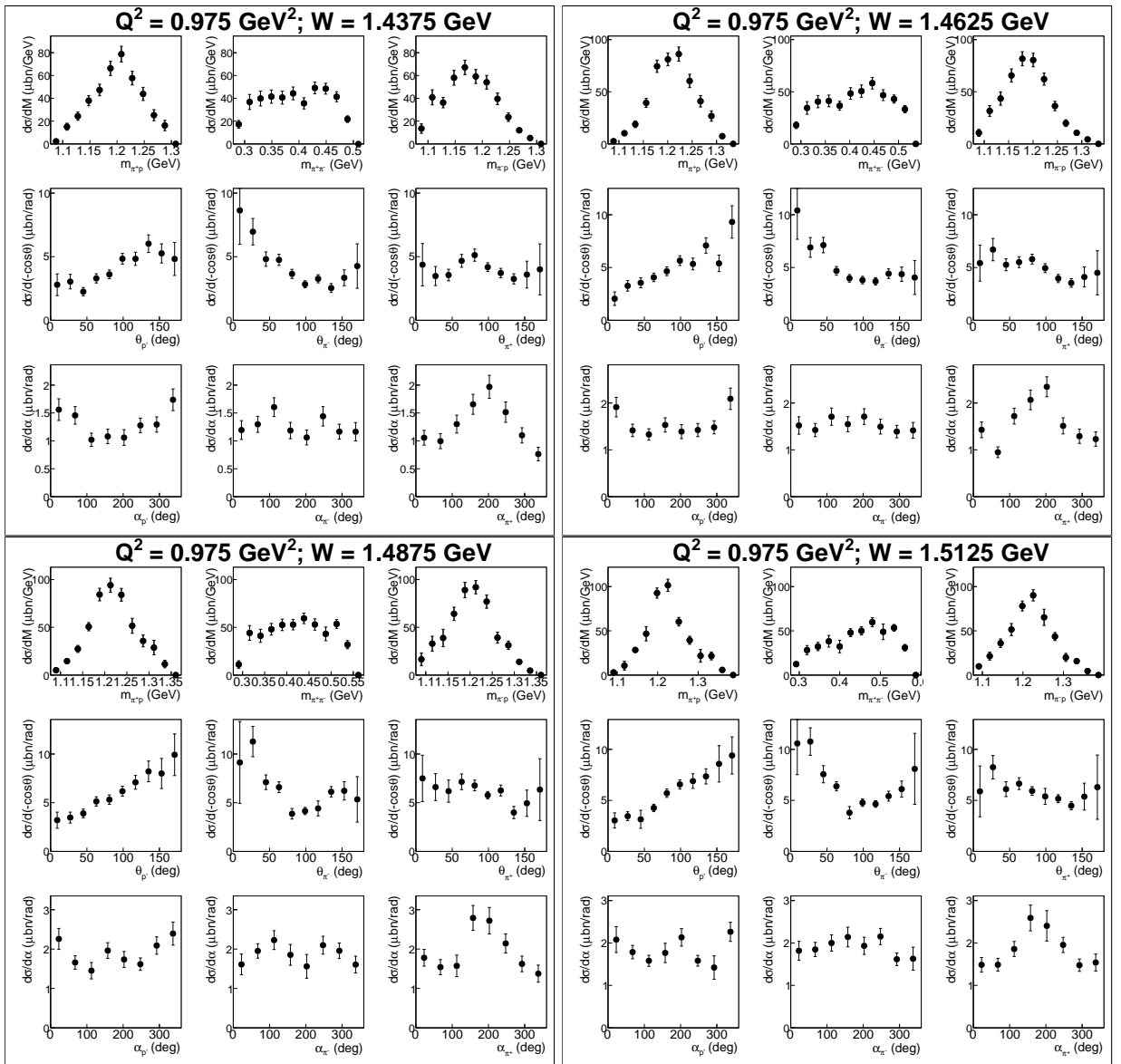


Figure A.47:

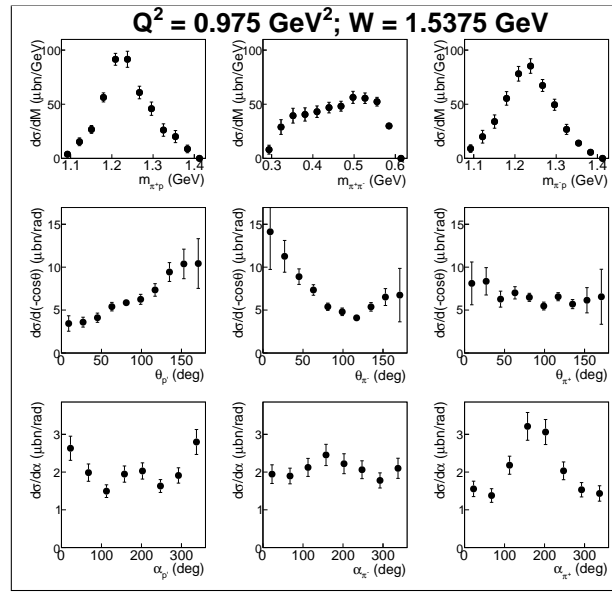


Figure A.48:

Bibliography

- [1] M. Ripani *et al.*, “Measurement of $e p \rightarrow e' \pi^+ \pi^-$ and baryon resonance analysis,” *Phys. Rev. Lett.*, vol. 91, p. 022002, 2003.
- [2] I. G. Aznauryan and V. D. Burkert, “Electroexcitation of nucleon resonances,” *Prog. Part. Nucl. Phys.*, vol. 67, pp. 1–54, 2012.
- [3] I. Aznauryan, V. D. Burkert, T. S. H. Lee, and V. I. Mokeev, “Results from the N* program at JLab,” *J. Phys. Conf. Ser.*, vol. 299, p. 012008, 2011.
- [4] I. G. Aznauryan *et al.*, “Electroexcitation of nucleon resonances from CLAS data on single pion electroproduction,” *Phys. Rev.*, vol. C80, p. 055203, 2009.
- [5] K. Park *et al.*, “Measurements of $ep \rightarrow e' \pi^+ n$ at $W = 1.6 - 2.0$ GeV and extraction of nucleon resonance electrocouplings at CLAS,” *Phys. Rev.*, vol. C91, p. 045203, 2015.
- [6] G. V. Fedotov *et al.*, “Electroproduction of $p \pi^+ \pi^-$ off protons at $0.2 \leq Q^2 \leq 0.6$ -GeV 2 and $1.3 \leq W \leq 1.57$ -GeV with CLAS,” *Phys. Rev.*, vol. C79, p. 015204, 2009.
- [7] V. I. Mokeev *et al.*, “Experimental Study of the $P_{11}(1440)$ and $D_{13}(1520)$ resonances from CLAS data on $ep \rightarrow e' \pi^+ \pi^- p'$,” *Phys. Rev.*, vol. C86, p. 035203, 2012.
- [8] V. I. Mokeev *et al.*, “New Results from the Studies of the $N(1440)1/2^+$, $N(1520)3/2^-$, and $\Delta(1620)1/2^-$ Resonances in Exclusive $ep \rightarrow e' p' \pi^+ \pi^-$ Electroproduction with the CLAS Detector,” *Phys. Rev.*, vol. C93, no. 2, p. 025206, 2016.

- [9] V. I. Mokeev, V. D. Burkert, T.-S. H. Lee, L. Elouadrhiri, G. V. Fedotov, and B. S. Ishkhanov, “Model Analysis of the p pi+ pi- Electroproduction Reaction on the Proton,” *Phys. Rev.*, vol. C80, p. 045212, 2009.
- [10] V. I. Mokeev and I. G. Aznauryan, “Studies of N^* structure from the CLAS meson electroproduction data,” *Int. J. Mod. Phys. Conf. Ser.*, vol. 26, p. 1460080, 2014.
- [11] I. V. Anikin, V. M. Braun, and N. Offen, “Electroproduction of the $N^*(1535)$ nucleon resonance in QCD,” *Phys. Rev.*, vol. D92, no. 1, p. 014018, 2015.
- [12] V. M. Braun, S. Collins, B. Glie, M. Gckeler, A. Schfer, R. W. Schiel, W. Slodner, A. Sternbeck, and P. Wein, “Light-cone Distribution Amplitudes of the Nucleon and Negative Parity Nucleon Resonances from Lattice QCD,” *Phys. Rev.*, vol. D89, p. 094511, 2014.
- [13] J. Segovia, I. C. Cloet, C. D. Roberts, and S. M. Schmidt, “Nucleon and Δ elastic and transition form factors,” *Few Body Syst.*, vol. 55, pp. 1185–1222, 2014.
- [14] D. Binosi, L. Chang, J. Papavassiliou, and C. D. Roberts, “Bridging a gap between continuum-QCD and ab initio predictions of hadron observables,” *Phys. Lett.*, vol. B742, pp. 183–188, 2015.
- [15] J. Segovia, B. El-Bennich, E. Rojas, I. C. Cloet, C. D. Roberts, S.-S. Xu, and H.-S. Zong, “Completing the picture of the Roper resonance,” *Phys. Rev. Lett.*, vol. 115, no. 17, p. 171801, 2015.
- [16] I. C. Cloet, C. D. Roberts, and A. W. Thomas, “Revealing dressed-quarks via the proton’s charge distribution,” *Phys. Rev. Lett.*, vol. 111, p. 101803, 2013.
- [17] I. C. Cloet and C. D. Roberts, “Explanation and Prediction of Observables using Continuum Strong QCD,” *Prog. Part. Nucl. Phys.*, vol. 77, pp. 1–69, 2014.

- [18] B. Julia-Diaz, T. S. H. Lee, A. Matsuyama, T. Sato, and L. C. Smith, “Dynamical coupled-channels effects on pion photoproduction,” *Phys. Rev.*, vol. C77, p. 045205, 2008.
- [19] E. Santopinto and M. M. Giannini, “Systematic study of longitudinal and transverse helicity amplitudes in the hypercentral constituent quark model,” *Phys. Rev.*, vol. C86, p. 065202, 2012.
- [20] I. G. Aznauryan and V. D. Burkert, “Extracting meson-baryon contributions to the electroexcitation of the $N(1675)\frac{5}{2}^-$ nucleon resonance,” *Phys. Rev.*, vol. C92, no. 1, p. 015203, 2015.
- [21] D. S. Carman, “Nucleon Resonance Structure Studies Via Exclusive KY Electroproduction,” 2016.
- [22] V. I. Mokeev, I. Aznauryan, V. Burkert, and R. Gothe, “Recent results on the nucleon resonance spectrum and structure from the CLAS detector,” *EPJ Web Conf.*, vol. 113, p. 01013, 2016.
- [23] <http://clasweb.jlab.org/bos/browsebos.php>.
- [24] K. Egian *et al.*, “Determination of electron energy cut due to the CLAS EC threshoul,” *CLAS-NOTE-99-007*, 1999.
- [25] M. Osipenko, A. Vlassov, and M. Taiuti, “Matching between the electron cndidate track and Cherenkov counter hit,” *CLAS-NOTE-2004-020*, 2004.
- [26] P. K. Khetarpal, “NEAR THRESHOLD NEUTRAL PION ELECTROPRODUCTION AT HIGH MOMENTUM TRANSFERS ,” *Ph. D. Thesis*, 2010.
- [27] K. Park, V. Burkert, L. Elouadrhiri, and W. Kim, “Kinematics Corrections for CLAS,” *CLAS-Note 2003-012*, 2003.

- [28] M. Ripani *et al.*, “A Phenomenological description of $\pi^-\Delta^{++}$ photoproduction and electroproduction in nucleon resonance region,” *Nucl. Phys.*, vol. A672, pp. 220–248, 2000.
- [29] I. G. Aznauryan, V. D. Burkert, G. V. Fedotov, B. S. Ishkhanov, and V. I. Mokeev, “Electroexcitation of nucleon resonances at $Q^2 = 0.65$ (GeV/c) 2 from a combined analysis of single- and double-pion electroproduction data,” *Phys. Rev.*, vol. C72, p. 045201, 2005.
- [30] V. I. Mokeev, V. D. Burkert, L. Elouadrhiri, A. A. Boluchevsky, G. V. Fedotov, E. L. Isupov, B. S. Ishkhanov, and N. V. Shvedunov, “Phenomenological analysis of the clas data on double charged pion photo and electro-production,” in *Proceedings, 5th International Workshop on Physics of excited nucleons (NSTAR 2005)*, pp. 47–56, 2005.
- [31] L. W. Mo and Y.-S. Tsai, “Radiative Corrections to Elastic and Inelastic e p and mu p Scattering,” *Rev.Mod.Phys.*, vol. 41, pp. 205–235, 1969.
- [32] C. Wu *et al.*, “Photoproduction of ρ^0 mesons and Delta-baryons in the reaction $\gamma p \rightarrow p\pi^+\pi^-$ at energies up to $s^{1/2} = 2.6$ GeV,” *Eur. Phys. J.*, vol. A23, pp. 317–344, 2005.
- [33] I. Skorodumina and G. Fedotov, “new 2 π event generator (https://clasweb.jlab.org/wiki/index.php/NEW_2PI_EVENT_GENERATOR),”
- [34] E. Byckling and K. Kajantie, *Particle Kinematics*. Jyvaskyla, Finland: University of Jyvaskyla, 1971.
- [35] B. Laforge and L. Schoeffel, “Elements of statistical methods in high-energy physics analyses,” *Nucl. Instrum. Meth.*, vol. A394, pp. 115–120, 1997.
- [36] *PHENOMENOLOGICAL ANALYSIS OF THE CLAS DATA ON DOUBLE CHARGED PION PHOTO AND ELECTRO-PRODUCTION*, 10-15 Oct 2005 2005.
- [37] “Photoproduction of meson and baryon resonances at energies up to 5.8-GeV,” *Phys.Rev.*, vol. 175, pp. 1669–1696, 1968.

- [38] R. Erbe *et al.*, “Multipion and strange-particle photoproduction on protons at energies up to 5.8-GeV,” *Phys. Rev.*, vol. 188, pp. 2060–2077, 1969.
- [39] N. Markov, “Single π^0 Electroproduction off the Proton in the Resonance region (https://www.jlab.org/Hall-B/general/thesis/Markov_thesis.pdf),” 2012.
- [40] E. Golovach, “Clas g11a experiment. clas analysis note. (under review),”
- [41] E. Isupov, “Double-pion electroproduction from clas e1-6 experiment clas analysis note.,”
- [42] P. E. Bosted, “An Empirical fit to the nucleon electromagnetic form-factors,” *Phys. Rev.*, vol. C51, pp. 409–411, 1995.